

Renormalization of crossing probabilities in the dilute Potts model

Pete Rigas

December 13, 2020

1 Introduction

Russo-Seymour-Welsh (RSW) theory provides estimates regarding the crossing probabilities across rectangles of specified aspect ratios, and was studied by Russo, and then by Seymour and Welsch on the square lattice, with results specifying the finite mean size of percolation clusters [23], in addition to a relationship that critical probabilities satisfy through a formalization of the sponge problem [24]. With such results, other models in statistical physics have been examined, particularly ones exhibiting sharp threshold phenomena [1,7] and continuous phase transitions [13], with RSW type estimates obtained for Voronoi percolation [27], critical site percolation on the square lattice [28], the Kostlan ensemble [2], and the FK Ising model [9], to name a few.

RSW arguments typically rely on self-duality of the model, in which the probability of obtaining a horizontal crossing is related, by duality, to the probability of obtaining a vertical crossing. Although this correspondence is useful for models enjoying self duality, previous arguments to obtain RSW estimates are not applicable to the dilute Potts model (in correspondence with the loop $O(n)$ model in presence of two external fields), which has been studied extensively by Nienhuis [15,19,20] who not only conjectured that the critical point of the model should be $1/\sqrt{2 + \sqrt{2 - n}}$ for $0 \leq n < 2$, but also has provided results for the $O(n)$ model on the honeycomb lattice [22] which has connective constant $\sqrt{2 + \sqrt{2}}$ [12]. It is also known that the loop $O(n)$ model, a model for random collections of loop configurations on the hexagonal lattice, exhibits a phase transition with critical parameter $1/\sqrt{2 + \sqrt{2 - n}}$, in which *subcritically* the probability of obtaining a macroscopic loop configuration of length k decays exponentially fast in k , while *at criticality* the probability of obtaining infinitely many macroscopic loop configurations, also of length k , and centered about the origin is bound below by c and above by $1 - c$ for $c \in (0, 1)$ irrespective of boundary conditions [8]. The existence of macroscopic loops in the loop $O(n)$ model has also been proved in [3] with the XOR trick.

In another recent work [14], Duminil-Copin & Tassion proposed alternative arguments to obtain RSW estimates for models that are no self-dual at criticality. The novel quantities of interest in the argument involve renormalization inequalities, which in the case of Bernoulli percolation can be viewed as a coarse graining argument, as well as the introduction of strip densities which are quantities defined as a limit supremum over a real parameter α . Ultimately, the paper proves RSW estimates for measures with free or wired boundary conditions in *subcritical, supercritical, critical discontinuous & critical continuous* cases, with applications of the two theorems relating to the mixing times of the random cluster measure, for systems undergoing discontinuous phase transitions [14,18]. Near the end of the introduction, the authors mention that potential generalizations of their novel renormalization argument can be realized in the dilute Potts model studied by Nienhuis which is equivalent to the loop $O(n)$ model, a model conjectured to exist in the same universality class as the spin $O(n)$ model.

With regards to the loop $O(n)$ model, previous arguments have demonstrated that the model undergoes a phase transition by making use of Smirnov's *parafermionic observable*, which was originally introduced to study conformal invariance of different models in several celebrated works [11,25,26]. As a holomorphic function, the discrete contour integral of the observable vanishes for specific choice of a multiplicative parameter to the winding term in the power of the exponential. Under such assumptions on σ , Duminil-Copin & friends prove exponential decay in the loop $O(n)$ model from arguments relating to the relative weights of paths and a discretized form of the Cauchy Riemann equations which is shown to vanish [8]. Historically, disorder operators share connections with the parafermionic observable and have been studied to prove the existence of phase transitions through examination of the behavior of expectations of random variables below, and above, a critical point [11,16], while other novel uses of the parafermionic observable have been introduced in [10].

2 Background

To execute steps of the renormalization argument in the hexagonal case, we introduce quantities to avoid making use of self duality arguments. For $G = (V, E)$, $n \geq 1$ and the strip $\mathbf{R} \times [-n, 2n] \equiv S_n \subset G$, let $\phi_{S_n}^\xi$, for $\xi \in \{0, 1, 0/1\}$,

respectively denote the measures with free, wired and Dobrushin boundary conditions in which all vertices at the bottom of the strip are wired. From such measures on the square lattice, several planar crossing events are defined in order to obtain RSW estimates for all four parameter regimes (*subcritical*, *supercritical*, *discontinuous & continuous critical*), including analyses of the intersection of crossing probabilities across a family of non disjoint rectangles \mathcal{R} , each of aspect ratio $[0, \rho n] \times [0, n]$ for $\rho > 0$, to obtain crossings across long rectangles à la FKG inequality, three arm events which establish lower bounds of the crossing probabilities across \mathcal{R} under translation and reflection invariance of ϕ , in addition to horizontal rectangular crossings which are used to prove renormalization inequalities through use of PushPrimal & PushDual relations. To begin, we define the horizontal and vertical crossing strip densities.

Definition 1 ([14, Theorem 2 & Corollary 3]): The *strip density* corresponding to the measure across a rectangle \mathcal{R} of aspect ratio $[0, \alpha n] \times [-n, 2n]$ with free boundary conditions is of the form,

$$p_n = \limsup_{\alpha \rightarrow \infty} \left(\phi_{[0, \alpha n] \times [-n, 2n]}^0 [\mathcal{H}_{[0, \alpha n] \times [0, n]}] \right)^{\frac{1}{\alpha}},$$

where \mathcal{H} denotes the event that \mathcal{R} is crossed horizontally, whereas for the measure supported over \mathcal{R} with wired boundary conditions, the crossing density is of the form,

$$q_n = \limsup_{\alpha \rightarrow \infty} \left(\phi_{[0, \alpha n] \times [-n, 2n]}^1 [\mathcal{V}_{[0, \alpha n] \times [0, n]}^c] \right)^{\frac{1}{\alpha}},$$

where \mathcal{V}^c denotes the complement of a vertical crossing across \mathcal{R} .

Besides the definition of the strip densities p_n and q_n , another key step in the argument involves inequalities relating p_n and q_n . The statement of the Lemma below holds under the assumption that the planar random cluster model is neither in the subcritical nor supercritical phase.

Lemma 1 ([14, Lemma 12]) There exists a constant $C > 0$ such that for every integer $\lambda \geq 2$, and for every $n \in 3\mathbb{N}$,

$$p_{3n} \geq \frac{1}{\lambda^C} q_n^{3+\frac{3}{\lambda}},$$

while a similar inequality holds between horizontal and the complement of vertical crossing probabilities of the complement \mathcal{V}^c across \mathcal{R} , which takes the form,

$$q_{3n} \geq \frac{1}{\lambda^C} p_n^{3+\frac{3}{\lambda}}.$$

Finally, we introduce the renormalization inequalities.

Lemma 2 ([14, Lemma 15]) There exists $C > 0$ such that for every integer $\lambda \geq 2$ and for every $n \in 3\mathbb{N}$,

$$p_{3n} \leq \lambda^C p_n^{3-\frac{9}{\lambda}} \quad \& \quad q_{3n} \leq \lambda^C q_n^{3-\frac{9}{\lambda}}.$$

To readily generalize the renormalization argument to the dilute Potts model, we proceed in the spirit of [14] by introducing hexagonal analogues of the crossing events discussed at the beginning of the section.

3 Towards hexagonal analogues of crossing events from the planar renormalization argument

3.1 Loop $O(n)$ measure, planar crossing event types

The Gibbs measure on a random configuration σ in the loop $O(n)$ model is of the form,

$$\mathbf{P}_{\Lambda,x,n}^\xi(\sigma) = \frac{x^{e(\sigma)} n^{l(\sigma)}}{Z_{\Lambda,x,n}^\xi}, \quad (\text{Loop measure})$$

where $\sigma(e)$ denotes the number of edges, $\sigma(l)$ the number of loops, $\Lambda \subset \mathbf{H}$, $\xi \in \{0, 1, 0/1\}$ and $Z_{\Lambda,e,n}^\xi$ is the partition function which normalizes $\mathbf{P}_{\Lambda,x,n}^\xi$ so that it is a probability measure. In particular, we restrict the parameter regime of x to that of [8], in which the loop $O(n)$ model satisfies the strong FKG lattice condition and monotonicity through a spin representation measure albeit $\mathbf{P}_{\Lambda,x,n}^\xi$ not being monotonic. By construction, $\mathbf{P}_{\Lambda,x,n}^\xi$ is invariant under $\frac{2\pi}{3}$ rotations. Through a particular extension for $n \geq 2$ of the spin representation of $\mathbf{P}_{\Lambda,\sigma(e),\sigma(l)}^\xi$, the measure on spin configurations $\sigma' \in \Sigma(G, \tau)$ is of the form

$$\mu_{G,x,n}^\tau(\sigma') = \frac{n^{k(\sigma')} x^{e(\sigma')} e^{hr(\sigma') + \frac{h'}{2}r'(\sigma')}}{Z_{G,x,n}^\tau}, \quad (\text{Spin Measure})$$

where $\tau \in \{-1, +1\}^{\mathbf{T}}$, $\Sigma(G, \tau)$ is the set of spin configurations coinciding with σ' outside of G , $r(\sigma') = \sum_{u \in G} \sigma'_u$ is the summation of spins inside G , $r'(\sigma') = \sum_{\{u,v,w\} \in G} \sigma'_u \mathbf{1}_{\sigma'_u = \sigma'_v = \sigma'_w}$ is the difference between the spins of monochromatic triangles, and $Z_{G,x,n}^\tau$ is the partition function which makes $\mu_{G,x,n}^\tau$ a probability measure. The extension enjoys translation invariance, a weaker form of the spatial/domain Markov property that will be mentioned in Section 5.1, comparison between boundary conditions that is mentioned in Section 3.2, & FKG for $n \geq 1$ and $nx^2 \leq 1$. The dual measure of $\mu_{G,x,n}^{+1}$ is $\mu_{G^*,x,n}^0$. Simply put, the superscripts above μ indicate whether the pushforward of a horizontal or vertical crossing event under the measure is under free, wired, or mixed boundary conditions.

To obtain boundary dependent RSW results on \mathbf{H} in all 4 cases, we identify crossing events in the planar renormalization argument in addition to difficulties associated with applying the planar argument to the push forward of similarly defined horizontal and vertical crossing events under $\mu_{G,x,n}^\tau$ on $(\mathbf{T})^* = \mathbf{H}$. In what follows, we describe all planar crossing events in the argument.

First, planar crossing events across translates of horizontal crossings across short rectangles of equal aspect ratio are combined to obtain horizontal crossings across long rectangles, through the introduction of a lower bound to the probability of the intersection that all short rectangles are simultaneously crossed horizontally with FKG. On \mathbf{H} , the probability of the intersection of horizontal crossing events of **first type** can be readily generalized to produce longer horizontal crossings from the intersection of shorter ones, through an adaptation of [14, Lemma 9].

Second, three arm events which determine whether two horizontal crossings to the top of a rectangle of aspect ratio $[0, n] \times [0, \rho n]$ intersect. Planar crossings of **second type** create symmetric domains over which the conditional probability of horizontal crossings in the symmetric domain can be determined, which for the renormalization argument rely on comparison between random cluster measures with free and wired boundary conditions. For random cluster configurations, comparison between boundary conditions is established in how the number of clusters in a configuration is counted. Comparison between boundary conditions applies to $\mu_{G,x,n}^\tau$ from [8], with hexagonal symmetric domains enjoying $\frac{2\pi}{3}$ symmetry.

Third, planar crossing events with wired boundary conditions, of **third type** induce wired boundary conditions within close proximity of vertical crossings in planar strips. Long planar horizontal crossings are guaranteed through applications of FKG across dyadic translates of horizontal crossings across shorter rectangles. For hexagonal domains, modifications to planar crossings of **first type** permit ready generalizations of **third type** planar crossings.

Fourth, planar horizontal crossing events of **fourth type** across rectangles establish relations between the strip densities p_n & q_n (Lemma 1). Finally, planar crossing events satisfying PushPrimal & PushDual conditions prove Lemma 2.

3.2 Comparison of boundary conditions & relaxed spatial markovianity for the $n \geq 2$ extension of the loop $O(n)$ measure

For suitable comparison of boundary conditions in the presence of external fields h, h' , the influence of boundary conditions from the fields on the spin representation amount to enumerating configurations differently for wired and free boundary

conditions than for the random cluster model in [14]. In particular, modifications to comparison between boundary conditions and the spatial Markov property.

Chiefly, the modifications entail that an admissible symmetric domain Sym inherit boundary conditions from partitions on the outermost layer of hexagons along loop configurations (see *Figures 1-3* in later section for a visualization of crossing events from the argument). Through distinct partitions of the $+/-$ assignment on hexagons on the outermost layer to the boundary, appearing in arguments for symmetric domains appearing in 5.1 - 5.4.

Corollary ([8, Corollary 10], comparison between boundary conditions for the Spin measure): Consider $G \subset \mathbf{T}$ finite and fix (n, x, h, h') such that $n \geq 1$ and $nx^2 \leq \exp(-|h'|)$. For any increasing event A and any $\tau \leq \tau'$,

$$\mu_{G,x,h,h'}^\tau[A] \leq \mu_{G,n,x,h,h'}^{\tau'}[A] .$$

Altogether, modifications to comparison of boundary conditions and the spatial Markov property between measurable spin configurations for μ is also achieved. We recall the (CBC) inequality for the random cluster model, and for the loop model make use of an "analogy" discussed in [8], in which we associate wired boundary conditions to the $+$ spin, and free boundary conditions to the $-$ spin over \mathbf{T} . Specifically, for boundary conditions ξ, ψ distributed under the random cluster measure ϕ , the measure supported over G satisfies

$$\phi_G^\xi[\mathcal{A}] \leq q^{\max\{k_\xi(\omega) - k_\psi(\omega) : \omega\} - \min\{k_\xi(\omega) - k_\psi(\omega)\}} \phi_G^\psi[\mathcal{A}] .$$

The Spin Measure introduced in the previous section, satisfies a similar relation,

$$\mu_{\mathbf{T}}^\tau[\mathcal{A}'] \leq n^{k_{\tau'}(\sigma) - k_\tau(\sigma)} x^{e_{\tau'}(\sigma) - e_\tau(\sigma)} e^{\frac{r_{\tau'}(\sigma) - r_\tau(\sigma)}{2}} \mu_{\mathbf{T}}^{\tau'}[\mathcal{A}'] ,$$

where the exponential factor in front of the pushforward in the upper bound, supported over \mathbf{T} , results from the difference between the number of monochromatically colored triangles in the configuration distributed under the Spin Measure, the edge weight associated with x , and the number of connected components $k(\sigma) + 1$, respectively with boundary conditions τ and τ' . The multiplicative factor arises from comparisons between the Spin Measure and the Random Cluster model measure, particularly by associating the summation over all spins in Spin Measure configurations with the ratio of the number of open edges to the number of closed edges in an FK percolation configuration, the number of connected components in a spin configuration under the loop O(n) model with the number of clusters in the Random cluster model, and also, the edge weights of x of spin configurations under the loop O(n) model with the cluster weights of q in the Random Cluster Model.

A special case of the inequality above will be implemented several times throughout the renormalization argument, stating,

$$\mu_{\mathbf{T}}^\tau[\mathcal{A}'] \leq n^{k_{\tau'}(\sigma) - k_\tau(\sigma)} (x \sqrt{e})^{\text{Stretch}} \mu_{\mathbf{T}}^{\tau'}[\mathcal{A}] ,$$

which will be introduced for an inequality in the proof of *Lemma 9**. The special case of the multiplicative factor above represents the difference in the number of clusters that are counted under boundary conditions τ, τ' , in addition to the corresponding edge weights x under each boundary condition. Stretch is a positive constant to which the edge weight and external field parameter are raised, which appears in arguments in *Lemma 1** in *Section 7*. We denote the modified properties for spin representations \mathcal{S} with $(\mathcal{S} \text{ CBC})$ and $(\mathcal{S} \text{ SMP})$. Besides such modifications, (MON) from [14] directly applies, and will be used several times. We abuse notation and refer to free boundary conditions under the Spin measure which represents $-$ boundary conditions, and wired boundary conditions for $+$ boundary conditions. The q^k "analogy" for the Spin Measure will enter into the novel renormalization argument at several points, stating,

- *Lemma 9**, in which $(\mathcal{S} \text{ SMP})$ will be repeatedly used to compare boundary conditions between crossings across the second or third edge of a hexagon, and boundary conditions for crossings across symmetric regions Sym ,
- *Corollary 11**, in which $(\mathcal{S} \text{ SMP})$ will be used to bound the pushfoward of horizontal crossings under wired boundary conditions, which in light of the homeomorphism f in 4.1, yields a corresponding bound for the pushforward of a vertical crossing under free boundary conditions,

- *Lemma 1**, in which an application of (\mathcal{S} SMP) and (MON) yield a lower bound for the probability of a horizontal crossing under free boundary conditions with a probability of a horizontal crossing under wired boundary conditions,
- *Lemma 2**, in which a modification to the lower bound obtained in the proof of *Lemma 1** is applied to obtain a lower bound for the probability of a horizontal crossing under wired boundary conditions with the probability of a vertical crossing under free boundary conditions,
- *Quadrichotomy proof*, in which the crossing events from previous results are compared to obtain the standard *box crossing estimate* that the Gibbs measure on loop configurations satisfies, per *Theorem 1*, [8].

3.3 Novelty of the inequalities

The strip and renormalization inequalities provided in the previous section are dependent on different quantities for \pm spin configurations rather than the corresponding inequalities for the random cluster model which only depend on the cluster weight q .

3.4 Results

The result presented for the loop $O(n)$ model mirrors the dichotomy of possible behaviors, in which the *standard box crossing estimate* reflects the influence of boundary conditions on the nature of the phase transition, namely that the transition is discontinuous, from the *discontinuous critical* case. To prove the *subcritical* & *supercritical* cases, the generalization to the dilute Potts model will make use of planar crossing events of **first** and **second** type, while crossing events of **third** and **fourth** type proves the remaining *continuous & discontinuous critical* cases. We denote the vertical strip domain \mathcal{S}_T with T hexagons, $\mathcal{S}_{T,L}$ the finite domain of \mathcal{S}_T of length $\pm L > 0$, and any regular hexagon $H_j \subset \mathcal{S}_T$ with side j [12]. The strip densities p_n^μ and q_n^μ are defined in 7.

Theorem 1* (μ homeomorphism): For $L \in [0, 1]$, there exists an increasing homeomorphism f_L so that for every $n \geq 1$, where $\mathcal{H}_H \equiv \mathcal{H}$ and $\mathcal{V}_H \equiv \mathcal{V}$ denote the horizontal and vertical crossings across a regular hexagon H , $\mu(\mathcal{H}) \geq f(\mu(\mathcal{V}))$.

Theorem 2* (hexagonal crossing probabilities): For the dilute regime $x \leq \frac{1}{\sqrt{n}}$, aspect ratio n of a regular hexagon $H \subset \mathcal{S}_T$, $c > 0$, and horizontal crossing \mathcal{H} across H , estimates on crossing probabilities with free, wired or mixed boundary conditions satisfy the following criterion in the following 4 possible behaviors.

- *Subcritical*: For every $n \geq 1$, under wired boundary conditions, $\mu_{G,x,n}^1[\mathcal{H}] \leq \exp(-cn)$,
- *Supercritical*: For every $n \geq 1$, under free boundary conditions, $\mu_{G,x,n}^0[\mathcal{H}] \geq 1 - \exp(-cn)$,
- *Continuous Critical* (Russo-Seymour-Welsh property): For every $n \geq 1$, independent of boundary conditions τ , $c \leq \mu_{G,x,n}^\tau[\mathcal{H}] \leq 1 - c$,
- *Discontinuous Critical*: For every $n \geq 1$, $\mu_{G,x,n}^1[\mathcal{H}] \geq 1 - \exp(-cn)$ for free boundary conditions, while $\mu_{G,x,n}^0[\mathcal{H}] \leq \exp(-cn)$ for wired boundary conditions.

As in the proofs for each set of inequalities located in Section 7 and Section 9.1, we set $p_*^\mu \equiv p_*$ and $q_*^\mu \equiv q_*$ for simplicity. Each one of the estimates below before letting $\rho \rightarrow \infty$ is achieved by concluding the argument with the q^k "analogy" mentioned on the previous page. The (\mathcal{S} CBC) leads to similar estimates for the Spin measure.

Lemma 1* (7, hexagonal strip density inequalities): In the **Non(Subcritical)** and **Non(Supercritical)** regimes, for every integer $\lambda \geq 2$, and every $n \in \text{Stretch } \mathbf{N}$, there exists a positive constant C satisfying,

$$p_{\text{Stretch } n} \geq \frac{1}{\lambda^C} \left(q_{\text{Stretch } n} \right)^{\text{Stretch} + \frac{\text{Stretch}}{\lambda}},$$

while a similar upper bound for vertical crossings is of the form,

$$q_{\text{Stretch } n} \geq \frac{1}{\lambda^C} \left(p_{\text{Stretch } n} \right)^{\text{Stretch} + \frac{\text{Stretch}}{\lambda}}.$$

With the strip densities for horizontal and vertical crossings, we state closely related renormalization inequalities.

Lemma 2* (*9, hexagonal renormalization inequalities*): In the **Non(Subcritical)** and **Non(Supcritical)** regimes, for every integer $\lambda \geq 2$, and every $n \in \text{Stretch } \mathbf{N}$, there exists a positive constant C satisfying,

$$p_{\text{Stretch } n} \geq \lambda^C \left(p_{\text{Stretch } n} \right)^{\text{Stretch} - \frac{n \text{ Stretch}}{\lambda}} \quad \& \quad q_{\text{Stretch } n} \geq \lambda^C \left(q_{\text{Stretch } n} \right)^{\text{Stretch} - \frac{n \text{ Stretch}}{\lambda}},$$

4 Proof of Theorem 1 & Lemma 9* preparation

To prove Theorem 1, we introduce 6-arm crossing events, from which symmetric domains will be crossed with good probability. The arguments hold for the $n \geq 2$ extension measure with free, wired or mixed boundary conditions. Previous use of such domains has been implemented to avoid using self duality throughout the renormalization argument [1,13]. Although more algebraic characterizations of fundamental domains on the hexagonal, and other, lattices exist [4], we focus on defining crossing events, from which we compute the probability conditioned on a path Γ crossing the symmetric region.

4.1 Existence of f

The increasing homeomorphism is shown to exist with the following.

Proposition 8* (*homeomorphism existence*): For any $L > 0$, there exists $c_0 = c_0(L) > 0$ so that for $nL \geq 1$, $\mu[\mathcal{H}] \geq c_0 \mu[\mathcal{V}]^{\frac{1}{c_0}}$.

Proof of Theorem 1.* With the statement of 8*, for $\mu = \mu^\tau$ on $\mathcal{S}_{T,L}$, μ^* is a measure supported on dual loop configurations, from which a correspondence between horizontal and vertical hexagonal crossings is well known. Trivially, by making use of 8*, rearrangements across the following inequality demonstrate the existence of f that is stated in *Theorem 1*, as

$$\mu^0[\mathcal{H}] \geq c_0 \mu^1[\mathcal{V}]^{\frac{1}{c_0}} \Leftrightarrow 1 - \mu^1[\mathcal{V}] \geq c_0 \left(1 - \mu^0[\mathcal{H}] \right)^{\frac{1}{c_0}} \Leftrightarrow \left(1 - \mu^1[\mathcal{V}] \right)^{c_0} \geq c_0^{c_0} \left(1 - \mu^0[\mathcal{H}] \right) \Leftrightarrow \mu^0[\mathcal{H}] \leq 1 - \frac{1}{c_0^{c_0}} \left(1 - \mu^1[\mathcal{V}] \right),$$

because by complementarity, $\mu^0[\mathcal{H}] + \mu^1[\mathcal{V}] = 1$. The existence of a homeomorphism satisfying $\mu(\mathcal{H}) \geq f(\mu(\mathcal{V}))$ is equivalent to $1 - \mu(\mathcal{V}) \geq f(\mu(\mathcal{V}))$, implying from the upper bound,

$$1 - \frac{1}{c_0^{c_0}} \left(1 - \mu^1[\mathcal{V}] \right) = \frac{c_0^{c_0} - 1 + \mu^1[\mathcal{V}]}{c_0^{c_0}} = \left(\frac{c_0^{c_0} - 1}{c_0^{c_0}} \right) + \frac{\mu^1[\mathcal{V}]}{c_0^{c_0}} = 1 - c_0^{-c_0} + c_0^{-c_0} \mu^1[\mathcal{V}].$$

The homeomorphism can be read off from the inequality, hence establishing its existence. \square

4.2 Crossing events for Lemma 9*

For a fixed ordering of all 6 edges that enclose any $H_j \subset \mathcal{S}_{T,L}$, $\{1_j, 2_j, 3_j, 4_j, 5_j, 6_j\}$, crossing events \mathcal{C} to obtain hexagonal symmetric domains with rotational and reflection symmetry will be defined. To obtain generalized regions from their symmetric counterparts in the plane from [14], we make use of comparison between boundary condition with the $n \geq 2$ extension measure. For μ , we are capable of readily proving a generalization of the union bound with the following prescription.

First, we define 6 armed crossing events across an arbitrary box $H_j \in \mathcal{S}_{T,L}$, from which countable families of crossing probabilities are introduced. The construction of the families is dependent on a partition of a single edge of H_j which we denote without loss of generality as edge 1_j of H_j . After partitioning 1 into equal k subintervals, each of length $\frac{s}{k}$, we define a countable family of crossing events from the partition \mathcal{S}_j of 1_j to the corresponding topmost edge 4_j of H_j , as well as crossing events from \mathcal{S}_j to all remaining edges of H_j . We also introduce a standard formulation of the union bound for the family of crossing events which has a lower bound dependent on the probability of a vertical hexagonal crossing. For our choice of 1_j , we position a horizontal line $\mathcal{L} \equiv [0, \delta] \times \{0\} \subset \mathbf{H}$ for arbitrary δ , from which we denote the horizontal translate $H_{j+\delta'}$ of H_j horizontally along \mathcal{L} by δ' where the magnitude of the translation satisfies

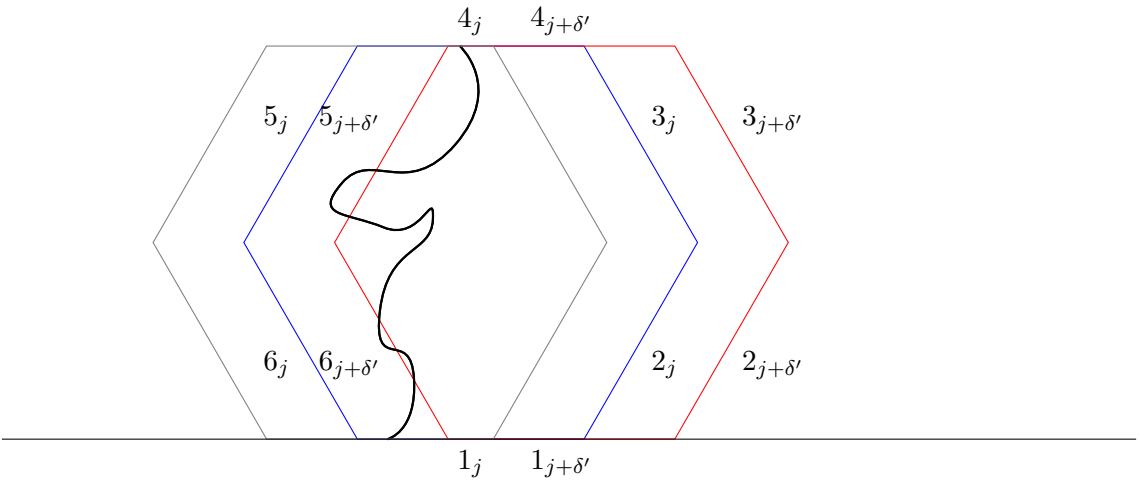


Figure 1: The centermost blue hexagon H_j flanked by its gray left translate $H_{j-\delta'}$, and its red right translate $H_{j+\delta'}$. 1_j lies incident to \mathcal{L} for every point on the edge. A vertical crossing from the partition $\mathcal{S}_j \subset 1_j$ to 4_j is shown.

$\delta' << \delta$. Second, across the countable family of crossing pairs for any sequence of 3 hexagons $\{H_{j-\delta'}, H_j, H_{j+\delta'}\}$, we define additional crossing events across the hexagonal translates through the stipulation that the crossing starting from an arbitrary partition of 1 to any of the remaining edges $\{2, 3, 4, 5, 6\}$ of H occur in the intermediate regions $H_{j-\delta'} \cap H_j$ and $H_j \cap H_{j+\delta'}$ ¹ (respectively given by the nonempty intersection between the gray and blue hexagons, and blue and red hexagons, in Figure 1 on the top of the next page) for $j > 0$. Third, we accommodate higher degrees of freedom in the number of arms for hexagonal events by reducing the number of crossing events taken in the maximum for the union bound, in turn reducing the 9* proof to three distinct cases. We generalize the argument to the dilute Potts model, which can be placed into correspondence with the loop $O(n)$ model, by accounting for the +/- spin representation from the extension μ . Fourth, we introduce adaptations to the renormalization argument across the remaining hexagonal domains. Finally, we let $L \rightarrow \infty$, and generalize the crossing events on \mathcal{S}_T in the weak limit along the infinite hexagonal strip.

Differences emerge in the proofs for the dilute Potts model in comparison to those of the random cluster model, not only in the encoding of boundary conditions for μ but also in the construction of the family of crossing probabilities, and the cases that must be considered to prove the union bound. We gather these notions below; denote the quantities corresponding to the partition $\mathcal{S}_j \subset 1_j$ with the following events,

$$\mathcal{C}_{2j} = \{\mathcal{S}_j \xleftrightarrow{H_{j+\delta'}} 2_{j-\delta'}\}, \quad \mathcal{C}_{3j} = \{\mathcal{S}_j \xleftrightarrow{H_{j+\delta'}} 3_{j-\delta'}\}, \quad \mathcal{C}_{4j} = \{\mathcal{S}_j \xleftrightarrow{H_j} 4_j\}, \quad \mathcal{C}_{5j} = \{\mathcal{S}_j \xleftrightarrow{H_{j-\delta'}} 5_{j+\delta'}\}, \quad \text{and} \quad \mathcal{C}_{6j} = \{\mathcal{S}_j \xleftrightarrow{H_{j-\delta'}} 6_{j+\delta'}\},$$

as well as the following crossing events across the left and right translates of H_j ,

$$\begin{aligned} \mathcal{C}'_{2j} &= \{\mathcal{S}_j \xleftrightarrow{H_{j+\delta'}} 2_{j+\delta'}\} \setminus \mathcal{C}_{2j}, \quad \mathcal{C}'_{3j} = \{\mathcal{S}_j \xleftrightarrow{H_{j+\delta'}} 3_{j+\delta'}\} \setminus \mathcal{C}_{3j}, \\ \mathcal{C}'_{5j} &= \{\mathcal{S}_j \xleftrightarrow{H_{j-\delta'}} 5_{j+\delta'}\} \setminus \mathcal{C}_{5j}, \quad \mathcal{C}'_{6j} = \{\mathcal{S}_j \xleftrightarrow{H_{j-\delta'}} 6_{j+\delta'}\} \setminus \mathcal{C}_{6j}. \end{aligned}$$

Along with the right and left translates of H_j , we can easily Before proceeding to make use of the 6-arm events to create symmetric domains for Lemma 9* (presented below), we briefly prove 8*.

Proof of Proposition 8.* Let $C_j = \{\mathcal{S}_j \xleftrightarrow{H_j \cup H_{j+2\delta'}} \mathcal{S}_{j+\delta'} \cup \mathcal{S}_{j+2\delta'}\}$. Uniformly in boundary conditions, for 8* horizontal (vertical) crossings \mathcal{H} (\mathcal{V}) across H_j can be pushed forwards under μ to obtain a standard lower bound for the probability of obtaining a longer vertical (horizontal) crossing \mathcal{V}' (\mathcal{H}') through one application of FKG to the finite intersection of shorter vertical (horizontal) crossings \mathcal{H}'_j (\mathcal{V}'_j),

$$\mu[\mathcal{H}'] \geq \mu\left(\bigcap_{j \in \mathcal{J}} C_j\right) \geq \prod_{j \in \mathcal{J}} \mu[\mathcal{V}'_j] \geq \left(\frac{c}{\lambda^3} \mu[\mathcal{V}']^3\right)^{|\mathcal{J}|}, \quad (\star)$$

¹In comparison to the argument of [14] which demands that crossings occur in between segments $S_2 \cup S_4$ in a rectangle R_0 , we introduce an auxiliary parameter δ' when defining crossing events.

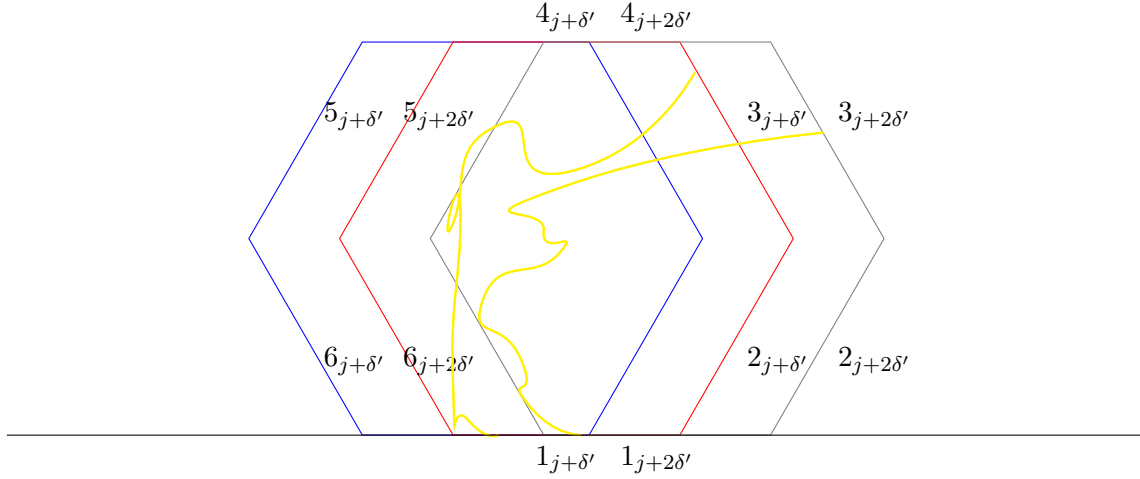


Figure 2: *Yellow* crossings from the partition $\mathcal{S}_{j+\delta'} \subset 1_{j+\delta'}$ to $3_{j+\delta'}$, and from the partition $\mathcal{S}_{j+2\delta'} \subset 1_{j+2\delta'}$ to $3_{j+2\delta'}$ are shown. We neglect illustrating additional connected components of loop configurations above in $H_{j-\delta'}$, H_j or $H_{j+\delta'}$ beyond the intersection of the paths with $3_{j+\delta'}$, as the paths would necessarily have to traverse leftwards so that the crossings respectively occur in H_j and $H_{j+\delta'}$. Under $\frac{2\pi}{3}$ rotational invariance of μ , symmetric domains constructed for \mathcal{C}_3 correspond to those for \mathcal{C}_{6_j} .

where the product is taken over admissible $j \in \mathcal{J} \equiv \{j \in \mathbf{R} : \text{there exists a regular hexagon with side length } j \text{ & } H_j \cap \mathcal{S}_{T,L} \neq \emptyset\}$, with $c, \lambda > 0$. We denote the sequence of inequalities with \star because the same argument will be applied several times for collections of horizontal and vertical crossings. From a standard lower bound from vertical crossings, the claim follows by setting λ equal to the aspect ratio of H_j . \square

The lower bound of \star above is raised to the cardinality of \mathcal{J} . We apply the same sequence of terms from this inequality to several arguments in *Corollary 11**, *Lemma 1**, *Lemma 2**, *Lemma 13**, & *Lemma 14**. We now turn to a statement of 9*.

Lemma 9* (6-arm events, existence of c): For every $\lambda > 0$ there exists a constant c, λ such that for every $n \in \mathbf{Z}$,

$$\mu[C_0] \geq \frac{c}{\lambda^3} \mu[\mathcal{V}]^3.$$

5 9* arguments

Proof of Lemma 9.* For the 6-arm lower bound, the argument involves manipulation of symmetric domains. In particular, we must examine the crossing event that is the most probable from the union bound, in 3 cases that are determined by the $\frac{2\pi}{3}$ rotational invariance of μ . Under this symmetry, in the union bound it is necessary that we only examine the structure of the crossing events \mathcal{C} in the following cases. We include the index j associated with crossing events \mathcal{C}_j , executing the argument for arbitrary j (in contrast to $j \equiv 0$ in [14]), readily holding for any triplet $j - \delta', j, j + \delta'$ which translates H_j horizontally. Besides exhibiting the relevant symmetric domain in each case, the existence of c will also be justified. Depending on the construction of Sym, we either partition the outermost layer to Sym, called the incident layer to ∂Sym , as well as sides of Sym with L_{Sym} , R_{Sym} , T_{Sym} and B_{Sym} . Finally, we finish the section with bounds in 5.4.3 to conclude the argument.

5.1 $\mathcal{C}_j \equiv \mathcal{C}_{2_j}$

In the first case, crossings across 2_j can be analyzed with the events \mathcal{C}_j and $\mathcal{C}_{j+2\delta'}$. To quantify the conditional probability of obtaining a $2_{j+\delta'}$ crossing beginning from $\mathcal{S}_{j+\delta'}$, let Γ_{2_j} and $\Gamma_{2_{j+2\delta'}}$ be the set of respective paths from \mathcal{S}_j and $\mathcal{S}_{j+2\delta'}$ to 2_j and $2_{j+2\delta'}$, and also realizations of the paths as $\gamma_1 \in \Gamma_{2_j}$, $\gamma_2 \in \Gamma_{2_{j+2\delta'}}$.

To accommodate properties of the dilute Potts model, we also condition that the number of connected components k_{γ_1} of γ_1 equal the number of connected components of k_{γ_2} of γ_2 in the spin configuration sampled under μ (see *Figure 3* for one example, in which the illustration roughly gives one half of the top part of Sym which is above the point of intersection x^{γ_1, γ_2} of the red and purple connected components, while the remaining purple connected components until x_T constitute one half of the lower half of Sym). We denote restrictions of the connected components for γ_1 and γ_2 to the

magnified region in *Figure 3*, and with some abuse of notation we still denote $k_{\gamma_1} \equiv k_{\gamma_1}|_{\mathcal{C}_j \cap \mathcal{C}_{j+2\delta'}}$ and $k_{\gamma_2} \equiv k_{\gamma_2}|_{\mathcal{C}_j \cap \mathcal{C}_{j+2\delta'}}$ for simplicity. Finally, assign $\Omega \subset \mathbf{H}$ as the points to the left of γ_1 and to the right of γ_2 , and the symmetric domain as $\text{Sym} \equiv \text{Sym}_{2_j} \equiv \text{Sym}_{2_j}(\Omega)$. To obtain a crossing across Sym, we conditionally pushforward the event

$$\mu[C_0 \mid \Gamma_{2_j} = \gamma_1 \& \Gamma_{2_{j+2\delta'}} = \gamma_2, k_{\gamma_1} = k_{\gamma_2}] ,$$

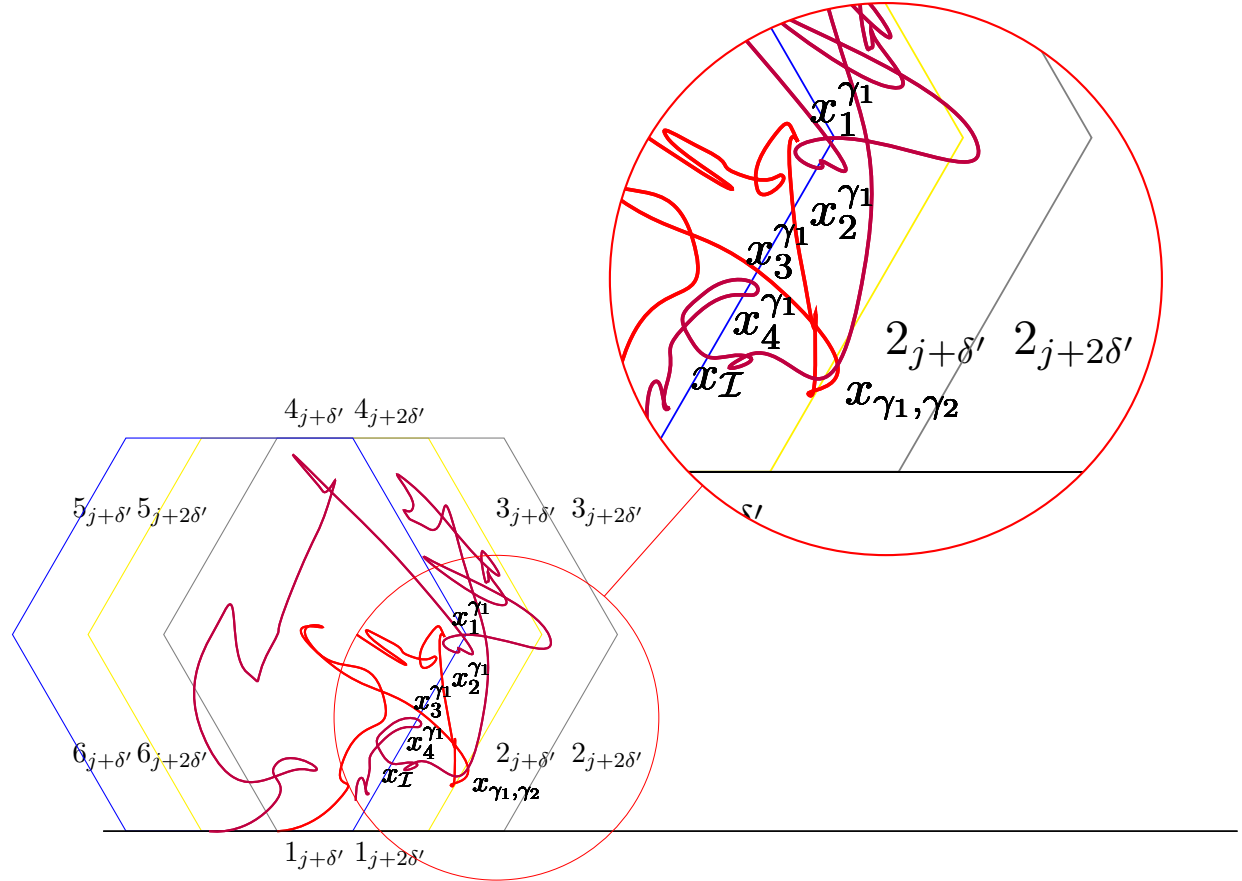


Figure 3: Sym construction from macroscopic $+/-$ crossings induced by \mathcal{C}_{2_j} and $\mathcal{C}_{2_{j+2\delta'}}$. Loop configurations with distribution \mathbf{P} , with corresponding $+/-$ random coloring of faces in \mathbf{H} with distribution μ , are shown with purple γ_1 and red γ_2 . Each configuration intersects 2_j , with crossing events occurring across the box H_j and its translate $H_{j+2\delta'}$. Under translation invariance of the spin representation, different classes of Sym domains are produced from the intersection of γ_1 and γ_2 , as well as the connected component of an intersection x_I incident to 2_j , which is shown above the second intersection of the red connected components of γ_2 . From one such arrangement of γ_1 and γ_2 , a magnification of the symmetric domain is provided, illustrating the contours of Sym which are dependent on the connected components of the outermost γ_2 path above x_{γ_1, γ_2} , while the connected components of γ_2 below x_{γ_1, γ_2} determine the number of connected components below the intersection. Across 2_j , one half of Sym is rotated to obtain the other half about the crossed edge. From paths of the connected components of each configuration, Sym is determined by forming the region from the intersection of the connected components of γ_1 and γ_2 in the magnified region. We condition on the number of connected components of each path by stipulating that they are equal to form two connected sets along the incident boundary to Sym. At the point of intersection between the red and purple $+/-$ spin configurations, the connected component associated with x_I determines half of the lowest side of Sym. The region allows for the construction of identical domains under \mathcal{C}_{5_j} and $\mathcal{C}_{5_{j+2\delta'}}$. Connected components are only shown in the vicinity of 2_j for the identification of boundaries of Sym, running from the intersection of γ_2 at the cusp of 2_j and 3_j , and from two nearby intersections of γ_1 with 2_j . The points of intersection of the purple connected components of γ_1 with 2_j are labeled $x_1^{\gamma_1}, x_2^{\gamma_1}, x_3^{\gamma_1}, x_4^{\gamma_1}, x_I$.

which quantifies the probability of obtaining a connected component across $\mathcal{S}_{j+\delta'} \cup \mathcal{S}_{j+2\delta'}$. We condition C_0 through γ_1 and γ_2 because if there exists a spin configuration passing through Sym whose boundaries are determined by γ_1 and γ_2 , then necessarily the configuration would have a connected component from \mathcal{S}_j to $\mathcal{S}_{j+2} \cup \mathcal{S}_{j+4}$ hence confirming that C_0 occurs. To establish a comparison between this conditional probability and the conditional probability of obtaining a horizontal crossing across Sym, consider

$$\mu[\gamma_1 \xleftarrow{\Omega} \gamma_2 \mid \Gamma_{2_j} = \gamma_1 \& \Gamma_{2_{j+2\delta'}} = \gamma_2, k_{\gamma_1} = k_{\gamma_2}] ,$$

subject to wired boundary conditions on R_{Sym} and L_{Sym} and free boundary conditions elsewhere. Conditionally this probability is an upper bound for another probability supported over Sym , as

$$\mu[\gamma_1 \xleftarrow{\Omega} \gamma_2 \mid \Gamma_{2_j} = \gamma_1 \& \Gamma_{2_{j+2\delta'}} = \gamma_2, k_{\gamma_1} = k_{\gamma_2}] \geq \mu_{\Omega}^{\{\gamma_1, \gamma_2\}}[\gamma_1 \longleftrightarrow \gamma_2] , \quad (\star \star)$$

with the conditioning on the connected components applying to $+/-$ spin configurations as shown in *Figure 3*, Ω is a region inside the symmetric domain (see *Figure 5*), and the $\{\gamma_1, \gamma_2\}$ superscript indicates boundary conditions wired along γ_1 and γ_2 . Similarly, conditional on $\Gamma_{2_j} = \gamma_1 \& \Gamma_{2_{j+2\delta'}} = \gamma_2$, $\{\gamma_1 \xleftarrow{\Omega} \gamma_2\}$ occurs. To quantify the probability of $\mathcal{C}_{2_{j+\delta'}} \setminus (C_0 \cup C_2)$, conditionally that the connect components of the event not intersect those of $\mathcal{C}_{2_j} \cap \mathcal{C}_{2_{j+2\delta'}}$, we introduce modifications through $(\mathcal{S} \text{ SMP})$, which impact the boundary conditions of the symmetric domains that will be constructed, while modifications through $(\mathcal{S} \text{ CBC})$ impact the number of paths that can be averaged over in Γ_{2_j} and $\Gamma_{2_{j+2\delta'}}$ given the occurrence of C_0 .

In particular, under the weaker form of the Spatial Markov Property, we can push boundary conditions away from nonempty boundary $\partial \text{Sym} \subset \partial H_j$ with the edge of intersection towards L_{Sym} , to then construct Sym by reflecting one half of the region enclosed by the realizations $\{\gamma_1, \gamma_2\} \subset \mathcal{C}_{2_j} \cap \mathcal{C}_{2_{j+2\delta'}}$, as follows. Because the event $\mathcal{C}_{j+\delta'}$ necessarily induces the existence of a loop configuration from S_j to 2_j , under Dobrushin/mixed boundary conditions which stipulate the existence of a wired arc of length $\frac{\pi}{6}$ along 2_j , the distribution μ on loop configurations satisfying \mathcal{C}_{2_j} implies that the probability of a crossing across Sym supported on $\mu_{\text{Sym}}^{\text{mix}}$ ². With wired boundary conditions along two sides of Sym , comparison between boundary conditions, and monotonicity, of the loop measure imply, under the circumstance of , that the pushforward of the conditionally defined crossing events under μ with dominate other boundary conditions on Sym .

Notably, boundary conditions are pushed forwards in the following partitions of hexagons incident with the boundary. We introduce equal partitions of the boundary through a $+/-$ coloring of the outermost layer of hexagons in finite volume domains. To partition vertices in Sym to then apply $(\mathcal{S} \text{ SMP})$, we assign $+$ boundary conditions to a partition of the first layer of hexagons outside of a loop configuration induced by $\mathcal{C}_{2_{j+\delta'}} \setminus (C_0 \cup C_2)$, conditioned under realizations $\gamma_1 \& \gamma_2$ sampled under μ , as follows. Given such a crossing, the length of the boundary of Sym is entirely determined by the number of connected components of the spin configuration, which corresponds to the edges of the spin configuration between neighboring hexagons that are colored $+$ and $-$. Next, we partition the outermost layer of hexagons outside of the paths above and below the intersection of the connected components of γ_1 and γ_2 (see *Figure 3* for loop configurations in **red** and **purple** sampled under μ whose connected components after intersection with 2_j yield boundaries of Sym). Without loss of generality, if we assume that the connected component of γ_1 in a neighborhood of 2_j is closer to the edge $2_{j+\delta'}$ than those of γ_2 , we take the connected components of γ_1 closest to $2_{j+\delta'}$ to construct one half of the top of Sym . The other top half of Sym will be readily obtained by reflection through 2_j , as will the remaining one half of the lower part. Below x_{γ_1, γ_2} , without loss of generality the connected components of γ_2 constitute one half of the lower region of Sym . Before reflection one half of Sym is constructed by taking the union $\gamma_1^{x_{\gamma_1, \gamma_2}} \cup \gamma_2^{x_{\gamma_1, \gamma_2}}$, where the paths in the union denote the restriction of the connected components of γ_1 and γ_2 after \mathcal{C}_j and $\mathcal{C}_{j+2\delta'}$ have occurred, given one specification stated below on the number of connected components of $\gamma_1^{x_{\gamma_1, \gamma_2}}$ relative to those of $\gamma_2^{x_{\gamma_1, \gamma_2}}$. The accompanying reflections $\tilde{\gamma}_1^{x_{\gamma_1, \gamma_2}}$ and $\tilde{\gamma}_2^{x_{\gamma_1, \gamma_2}}$ give the other half of Sym . Finally, we denote $x_{\mathcal{T}}$ as another point of intersection of γ_1 (γ_2) with 2_j besides the intersection of $\gamma_1^{x_{\gamma_1, \gamma_2}}$ ($\gamma_2^{x_{\gamma_1, \gamma_2}}$) determining the height of Sym (see *Figure 3* for multiple intersection points of the **red** and **purple** spin configurations with 2_j).

5.1.1 First partition of the incident hexagonal layer to ∂Sym

Besides the construction of Sym from the connected components, it remains to detail how $+$ spins are distributed in the partition along the boundary. Under the relaxation $(\mathcal{S} \text{ SMP})$, symmetric domains can only be constructed when the number of connected components of γ_1 above x_{γ_1, γ_2} equals those of γ_2 below x_{γ_1, γ_2} . Under this hypothesis, the first partition of the first layer of hexagons outside of the connected components of Sym can be achieved by assigning $+$ spins to the first layer bordering the restriction of connected components of $\gamma_1^{x_{\gamma_1, \gamma_2}}$, while $-$ spins can be assigned to the bordering first layer of the restriction of connected components of $\gamma_2^{x_{\gamma_1, \gamma_2}}$. Under this assignment, one half of Sym can be readily constructed by reflection across 2_j . The intersection of the connected components at x_{γ_1, γ_2} establishes the proportion of $+$, or $-$, signs that are distributed in between 2_j and $2_{j+\delta'}$. With the first partition of the layer incident to the boundary of Sym , we accommodate $(\mathcal{S} \text{ SMP})$ by assigning $+$ boundary conditions, with a $-$ assignment of boundary

²The mix boundary conditions are provided in two separate constructions of Sym below.

conditions to the remaining connected components of γ_2 below x_{γ_1, γ_2} . Finally, we reflect the region across 2_j to obtain the resulting domain which has wired boundary conditions along its top arc, and free boundary conditions along its bottom arc. (\mathcal{S} CBC) will be invoked through a comparison of a slightly altered Sym with wired boundary conditions along the entirety of the union of connected components of $\gamma_1^{x_{\gamma_1, \gamma_2}} \cup \gamma_2^{x_{\gamma_1, \gamma_2}}$ and hence along the whole domain itself.

5.1.2 Second partition of the incident hexagonal layer to ∂ Sym

We present a second partition of the incident layer to the boundary of Sym under the spin flip $\sigma \mapsto -\sigma$. In contrast to the first vertex partition above, the second partition achieves a partition of the incident layer to the connected components with the assignment of $-$ spins along $\gamma_1^{x_{\gamma_1, \gamma_2}}$, and $+$ spins assigned along $\gamma_2^{x_{\gamma_1, \gamma_2}}$, inducing free boundary conditions along the top half of Sym and wired boundary conditions along the bottom half of Sym (see *Figure 4*). The remaining half of symmetric domains corresponding to the second partition of $\gamma_1^{x_{\gamma_1, \gamma_2}} \cup \gamma_2^{x_{\gamma_1, \gamma_2}}$ can similarly be constructed through reflection.

5.2 Incorporating (\mathcal{S} SMP)

We progress towards making use of another modification for the dilute Potts model through the two types of symmetric domains above to ensure that such domains are conditionally bridged with good probability. We make use of the comparison through the following modification of Sym.

5.2.1 Modification to boundary conditions induced by the first partition of the Sym incident layer

A first modification of the incident hexagonal layer can be realized by taking the first partition presented, through a modification of the $+$ spin assignment along the incident layer bordering $\gamma_1^{x_{\gamma_1, \gamma_2}}$ uniformly to $-$ spins, while leaving the $-$ spin assignment to the incident layer bordering $\gamma_2^{x_{\gamma_1, \gamma_2}}$ fixed. This construction yields a class of symmetric domains with free boundary conditions along the entire boundary before reflecting to obtain the other half.

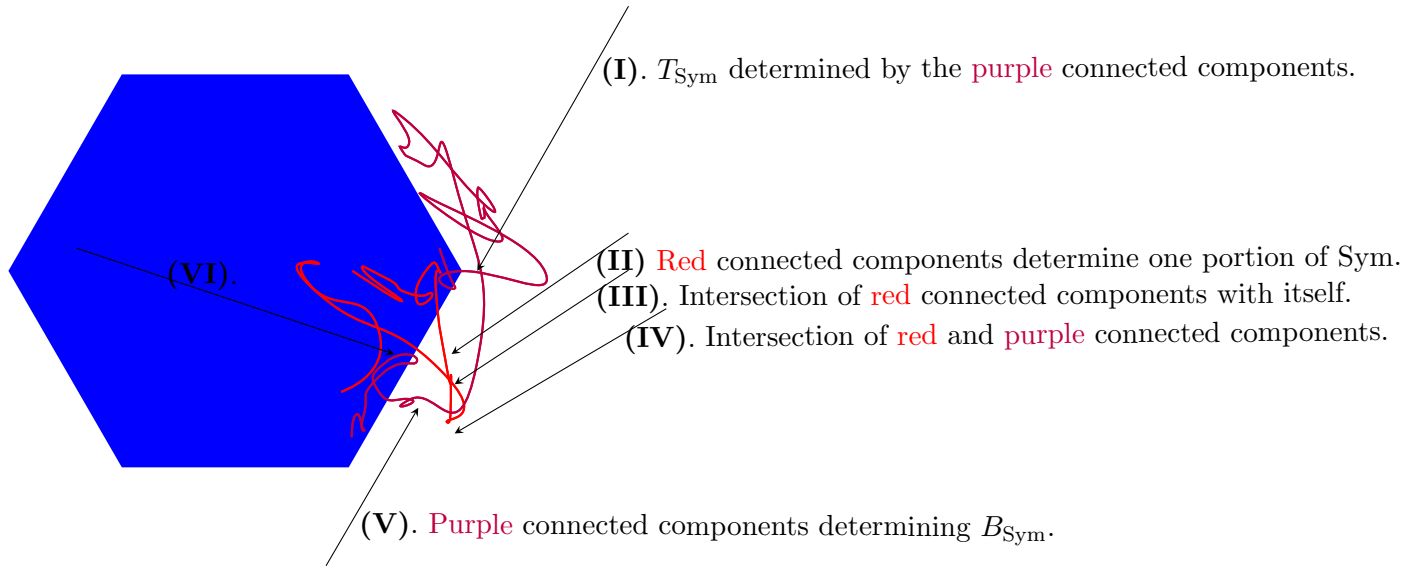


Figure 4: Sym from *Figure 3*, incident to 2_j . The region in between the connected components of each path constitute the boundaries of the symmetric region. Arrows are shown to each connected component which are used to construct Sym given relevant connected components of γ_1 and γ_2 . The non trivial intersection of the red and purple connected components within the blue interior of H_j determine one half of Sym before reflection. (I) illustrates the top side of Sym determined by the intersection of the purple connected components with itself. (II) illustrates a portion of Sym that is reflected about 2_j to obtain the other half of Sym. (III) illustrates the intersection of red connected components with itself. (IV) illustrates the intersection of connected components from γ_1 and γ_2 which are removed from the interior of Sym. (V) illustrates the purple connected components determining B_{Sym} . (VI) illustrates the red connected components that are removed from the interior of Sym, upon multiple intersection points with 2_j .

5.2.2 Modification to boundary conditions induced by the second partition of the Sym incident layer

A second modification of the incident hexagonal layer can be realized by taking the second partition presented, through a modification of the $-$ spin assignment along the incident layer bordering $\gamma_2^{x_{\gamma_1, \gamma_2}}$ uniformly to $+$ spins, while leaving the $+$ spin assignment to the incident layer bordering $\gamma_1^{x_{\gamma_1, \gamma_2}}$ fixed. This construction yields a class of symmetric domains

with wired boundary conditions along the entire boundary before reflecting to obtain the other half which inherits wired boundary conditions.

Next, we make use of the two types of Sym domains, in addition to the modification of boundary conditions as follows. From an application of (S CBC), the conditional probability introduced at the beginning of the proof, under spin configurations supported on μ_{Sym} satisfies, under the conditional measure $\mu_\Omega \equiv \mu_\Omega[\cdot | \Omega \mid \gamma_1 \cap \gamma_2 = \emptyset, \gamma_1 \cap \gamma_3 = \emptyset, k_{\gamma_1} = k_{\gamma_2}]$, for measurable events depending on finitely many edges in Ω ,

$$\mu[\mathcal{C}_{2j} \setminus (C_0 \cup C_2) \mid \Gamma_{2j} = \gamma_1 \& \Gamma_{2j+2\delta'} = \gamma_2, k_{\gamma_1} = k_{\gamma_2}] \leq \mu_\Omega^{\{\gamma_1, \gamma_2\}^c} [\mathcal{C}_{2j+\delta'}] ,$$

after examining the pushforward of the conditional probability above under spin configurations supported in Sym, where the superscript $\{\gamma_1, \gamma_2\}^c$ denotes free boundary conditions along γ_1 and γ_2 and wired elsewhere, the complement of $\{\gamma_1, \gamma_2\}$ given in the lower bound of $\star \star$. The stochastic domination above of the conditional probability under no boundary conditions on any side of Sym will be studied for paths $\gamma_3 \in \Gamma_{j+\delta'}$. The event under $\mu_\Omega^{\{\gamma_1, \gamma_2\}^c}$ demands that the connected components of γ_3 be disjoint for those of γ_1 and γ_2 for the entirety of the path.

Particularly, we remove the conditioning from the pushforward in the upper bound because the definition of Ω implies that connectivity holds in between γ_1 and γ_2 . Pointwise, the connected components of γ_3 do not intersect those of γ_1 and γ_2 . Recalling $\star \star$ in 5.1, we present additional modifications to the renormalization argument through the lower bound of the inequality to exhaust the case for $\mathcal{C}_j \equiv \mathcal{C}_{2j}$. Lower bounds for the pushforward under μ_Ω can only be obtained for mixed boundary conditions along Sym precisely under partitions of the incident hexagonal layer given in 5.1.1 & 5.1.2.

Under the conditions of (S SMP), crossings in Ω with boundary conditions $\{\gamma_1, \gamma_2\}$, the lowermost bound for $\star \star$ can only be established when boundary conditions are distributed under 5.1.1 or 5.1.2. For completeness, we first establish the lower bound for 5.1.1, in which the boundary conditions for a crossing distributed under $\mu_{\text{Sym}}^{\{\gamma_1, \gamma_2\}}$ can be compared to a closely related crossing distributed under $\mu_\Omega^{\{\gamma_1, \gamma_2\}^c}$.

To establish the comparison, the edges in $\text{Sym} \cap \Omega$, we divide the proof into separate cases depending on whether the boundary conditions for vertices along γ_1 or γ_2 are connected together under wired or free boundary conditions. One instance of pushing boundary conditions occurs for $\mathcal{C}_j \equiv \mathcal{C}_{2j}$, while another instance of pushing boundary conditions occurs when $\mathcal{C}_j \equiv \mathcal{C}_{4j}$ in Section 5.4.³

5.2.3 Pushing wired boundary conditions away from Ω towards Sym in the first partition of the incident layer

One situation occurs as follows. It is possible that $+ \setminus -$ configurations distributed under μ_Ω can be compared to configurations distributed under μ_{Sym} by pushing boundary conditions away from the first partition of Sym towards Ω ; applying (S CBC) between deterministic and random circuits yields

$$\mu_\Omega^{\{\gamma_1, \gamma_2\}^c} [\mathcal{C}_{2j+\delta'}] \leq \mu_{\text{Sym}}^{\{T, B\}} [\mathcal{C}_{2j+\delta'}] ,$$

by virtue of monotonicity in the domain because $\Omega \subset \text{Sym}$, where μ_Ω is taken under boundary conditions $\{T, B\}$ wired along T_{Sym} and B_{Sym} . Additionally, the comparison

$$\mu_{\text{Sym}}^{\{T, B\}} [\mathcal{C}_{2j+\delta'}] \leq \mu_{\text{Sym}}^{\{T, B\}} [T_{\text{Sym}} \longleftrightarrow B_{\text{Sym}}] ,$$

holds by virtue of the FKG inequality for the Spin measure, in which we suitably restricted our analysis of μ for $n \geq 1$ & $nx^2 \leq 1$, from which it follows that the event $\{T_{\text{Sym}} \longleftrightarrow B_{\text{Sym}}\}$ depends on more edges than the conditional event $\{\mathcal{C}_{2j+\delta'} \mid \gamma_1 \cap \gamma_2 = \emptyset, \gamma_1 \cap \gamma_3 = \emptyset, k_{\gamma_1} = k_{\gamma_2}\}$ under μ_Ω does and is an increasing event. Finally, the simplest comparison, namely the equality

$$\mu_{\text{Sym}}^{\{T, B\}} [T_{\text{Sym}} \longleftrightarrow B_{\text{Sym}}] = \mu_{\text{Sym}}^{\{L, R\}} [L_{\text{Sym}} \longleftrightarrow R_{\text{Sym}}] ,$$

³In contrast to the planar case of [14], considerations through the condition $k_{\gamma_1} = k_{\gamma_2}$ impact the construction of Sym and the rotational symmetry the region enjoys.

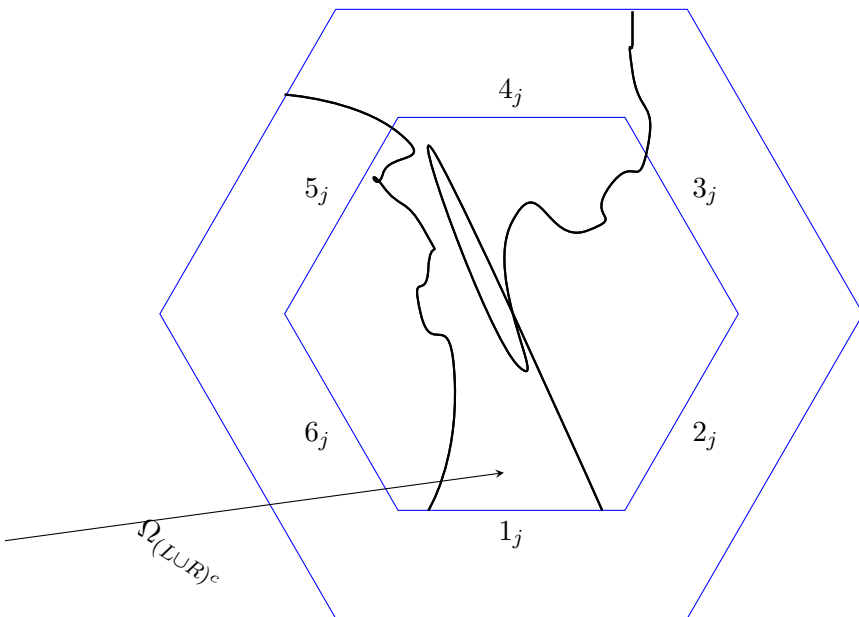


Figure 5: $\mathcal{C}_j \equiv \mathcal{C}_{4_j}$ case for crossing events through paths to the topmost edge 4_j , in addition to Ω and its subsets from the partition are indicated. By construction, the three partitions of 1_j from which the top to bottom crossings occur begin respectively from \mathcal{S}_j , $\mathcal{S}_{j+\delta'}$ and $\mathcal{S}_{j+2\delta'}$. Connectivity induced by $\mathcal{C}_{4_{j+\delta'}}$ occurs in $\Omega_{(L \cup R)^c}$. A symmetric region for this case in the proof requires a hexagonal box encompassing H_j across which connectivity events are quantified. Bottom crossings to any of the topmost three edges of H_j under wired boundary conditions induce bottom to top crossings.

holds by virtue of dual boundary conditions of μ_{Sym} , in which the pushforward of the event $\{T_{\text{Sym}} \longleftrightarrow B_{\text{Sym}}\}$ under boundary conditions $\{T, B\}$ is equal to the pushforward of the event $\{L_{\text{Sym}} \longleftrightarrow R_{\text{Sym}}\}$ under boundary conditions $\{L, R\}$. Hence complementarity implies that the rotation of boundary conditions of Sym gives the following upper bound,

$$\mu[\mathcal{C}_{2_j} \setminus (C_0 \cup C_2) \mid \Gamma_{2_j} = \gamma_1 \& \Gamma_{2_{j+2\delta'}} = \gamma_2, k_{\gamma_1} = k_{\gamma_2}] \leq \mu_{\Omega}^{\{\gamma_1, \gamma_2\}^c} [\mathcal{C}_{2_{j+\delta'}}],$$

which holds by (S SMP), as wired boundary conditions for \mathcal{C}_{2_j} in between γ_1 and γ_2 can be pushed away to obtain wired boundary conditions along γ_1 and γ_2 for $\mathcal{C}_{2_{j+\delta'}}$, in turn transitively yielding,

$$\mu[\mathcal{C}_{2_j} \setminus (C_0 \cup C_2) \mid \Gamma_{2_j} = \gamma_1 \& \Gamma_{2_{j+2\delta'}} = \gamma_2, k_{\gamma_1} = k_{\gamma_2}] \leq \mu_{\text{Sym}}^{\{L, R\}} [L_{\text{Sym}} \longleftrightarrow R_{\text{Sym}}].$$

5.2.4 Pushing boundary conditions away from Ω towards Sym in the second partition of the incident layer

The argument proceeds as in the previous case from 5.2.3, with the exception that the incident layer to Sym is partitioned according to 5.1.2. Following the same sequence of inequalities given above establishes that wired boundary conditions distributed under μ_{Sym} under the spin flip $\sigma \mapsto -\sigma$ are free along γ_1 and γ_2 instead of wired as in 5.2.3. The rest of the argument applies by incorporating simple modifications to the boundary conditions of μ_{Sym} .

Under $\frac{2\pi}{3}$ rotational invariance of μ , the argument for this case can be directly applied with $\mathcal{C}_j \equiv \mathcal{C}_{5_j}$. Examining the pushforward of this crossing event, in addition to $\mathcal{C}_{5_{j-\delta'}}$ which guarantees the existence of a connected component that necessarily crosses 5_j through $5_{j-\delta'}$, leads to the same conclusion with wired boundary conditions from to along Sym. Under duality, the identification between measures under nonempty boundary conditions over Sym readily applies. Hence a combination of (S SMP), followed by (S CBC), implies that $\{L_{\text{Sym}} \longleftrightarrow R_{\text{Sym}}\}$ occurs with substantial probability for $\mathcal{C}_j \equiv \mathcal{C}_{2_j}$ and $\mathcal{C}_j \equiv \mathcal{C}_{5_j}$.

5.3 $\mathcal{C}_j \equiv \mathcal{C}_{3_j}$

In the second case, one can apply similar arguments with the following modifications. To identify other possible symmetric regions Sym corresponding to \mathcal{C}_{3_j} and $\mathcal{C}_{3_{j+2\delta'}}$, fix path realizations $\gamma_1 \in \Gamma_{3_j}$ and $\gamma_2 \in \Gamma_{3_{j+2\delta'}}$ (see Figure 2 for yellow connected components in the Sym construction). From γ_1 and γ_2 , we construct Sym by reflecting half of the domain

across 3_j instead of 2_j . Under $\frac{2\pi}{3}$ rotational invariance of μ , Sym constructed in this case correspond to symmetric domains induced by the paths in \mathcal{C}_{5_j} and $\mathcal{C}_{5_{j+2\delta'}}$. Explicitly, the conditional probability is of the familiar form,

$$\mu[\mathcal{C}_{3_j} \setminus (C_0 \cup C_2) \mid \Gamma_{2_j} = \gamma_1 \& \Gamma_{2_{j+2\delta'}} = \gamma_2, k_{\gamma_1} = k_{\gamma_2}] ,$$

which by the same argument applied to \mathcal{C}_{3_j} is bounded above by

$$\mu_{\text{Sym}}^{\{L,R\}}[L_{\text{Sym}} \longleftrightarrow R_{\text{Sym}}] ,$$

for $\text{Sym}(\Omega) \equiv \text{Sym}$. Applying the same argument to push boundary conditions away from wired boundary conditions on 3_j (5_j), to L_{Sym} (R_{Sym}) establishes the same sequence of inequalities, through contributions of μ, μ & μ_{Sym} . Sym for \mathcal{C}_{3_j} corresponds to rotating the crossings of loop configurations, and hence the symmetric region to 5_j from the symmetric domain corresponding to 2_j in *Figure 3*.

5.4 $\mathcal{C}_j \equiv \mathcal{C}_{4_j}$

In the third case, we denote the events C_0 and C_2 as bottom to top crossings, respectively across H_j and $H_{j+2\delta'}$, with respective path realizations Γ_1 and Γ_1 as in the previous two cases. However, the final case for top to bottom crossings stipulates that the construction of Sym independently of Ω . We present modifications to the square symmetric region of [14], and partition the region over which connectivity events are quantified through points to the left and right of γ_1 and γ_2 , respectively. In particular, we denote Ω as the collection of all points in the hexagonal box Sym, along with the partition $\Omega = \Omega_L \cup \Omega_{(L \cup R)^c} \cup \Omega_R$. In the partition, each set respectively denotes the points to the left of γ_1 , the points in between the left of γ_1 and the right of γ_2 , and the points to the right of γ_2 . With some abuse of notation we restrict the paths in Ω_L , Ω_R and $\Omega_{(L \cup R)^c}$ to coincide with crossings in between the top most edge of H_j and Sym, in which $\Omega_R \equiv (\text{Sym} \cap H_j) \cap \Omega_R$, $\Omega_L \equiv (\text{Sym} \cap H_j) \cap \Omega_L$, and $\Omega_{(L \cup R)^c} \equiv (\text{Sym} \cap H_j) \cap \Omega_{(L \cup R)^c}$ (see *Figure 5* above for the Ω partition). We provide such an enumeration to apply (S SMP) and then (S CBC), when comparing the spin representation measures supported over Ω and Sym.

Besides the Ω partition, to apply (S SMP) we examine $\mathcal{R}_1 \equiv (\text{Sym} \setminus H_j^c) \cap \Omega_L$ and $\mathcal{R}_2 \equiv (\text{Sym} \setminus H_j^c) \cap \Omega_R$ which denote the collection of points to the left of γ_1 and to the right of γ_2 in the region above H_j that is contained in Sym (see *Figure 5* for H_j embedded within the hexagonal symmetric domain). To apply (S CBC), it is necessary that we isolate \mathcal{R}_1 and \mathcal{R}_2 so that (S CBC) can be applied to the outermost layer of hexagons incident to $\partial \Omega$ through a partition of the incident layer.

Again, we provide an upper bound for the pushforward of the following conditional probability, for $\mathcal{R} \equiv \{\Gamma_{2_j} = \gamma_1 \& \Gamma_{2_{j+2\delta'}} = \gamma_2, \gamma_1 \cap \gamma_3 = \emptyset, \gamma_1 \cap \gamma_2 = \emptyset\}$

$$\mu[\mathcal{C}_{4_j} \setminus (C_0 \cup C_2) \mid \mathcal{R}] ,$$

for the class of hexagonal box symmetric domains Sym, with $\gamma_3 \in \Gamma_{j+\delta'}$.

5.4.1 Class of partitions of the incident layer to the Sym boundary

Along the incident layer, the boundary conditions for hexagonal Sym can be equally partitioned into two disjoint sets over which the $+ \backslash -$ coloring is constant as follows. The first partition of the incident layer is achieved by assigning boundary conditions along the topmost three edges of the hexagon and assigning free boundary conditions along the bottommost three edges. More generally, a more wide family of boundary conditions for Sym used in $\mathcal{C}_j \equiv \mathcal{C}_{4_j}$ than Sym used in $\mathcal{C}_j \equiv \mathcal{C}_{2_j}$ and $\mathcal{C}_j \equiv \mathcal{C}_{3_j}$ because any counterclockwise $\frac{\pi}{6}$ rotation of boundary conditions yields other boundary conditions in which the partition of the boundary that is wired is translated downwards by $\frac{\pi}{6}$ (see *Figure 5* for top to bottom crossings across Sym and H_j).

5.4.2 Pulling boundary conditions away from H_j towards Sym

Next, we push boundary conditions away from H_j . Under the assumption that the upper half of Sym is endowed with wired boundary conditions while the lower half is endowed with free boundary conditions. We denote these boundary conditions with Top, and will consider the measures supported over Sym, respectively. From observations in previous

cases, to analyze the conditional probability of C_0 given $\Gamma_j = \gamma_1$ and $\Gamma_{j+2\delta'} = \gamma_2$, we introduce the following lower bound for a connectivity event between γ_1 and γ_2 in Ω , with,

$$\mu[C_0 \mid \mathcal{R}] \geq \mu[\gamma_1 \xrightarrow{\Omega} \gamma_2 \mid \mathcal{R}] ,$$

holds from arguments applied when $\mathcal{C}_j \equiv \mathcal{C}_{2,j}$. By construction, $H_j \subset \text{Sym}$ implies

$$\mu[\mathcal{C}_{4,j} \mid \mathcal{R}] \leq \mu_{\Omega_{(L \cup R)^c}}^{\{\gamma_1, \gamma_2\}^c}[\mathcal{C}_{4,j} \mid \mathcal{R}] ,$$

due to monotonicity in the domain, as the occurrence of $\mathcal{C}_{4,j}$ conditionally on disjoint connected components of $\gamma_3 \in \Gamma_{j+\delta'}$ with those of γ_1 and γ_2 . In comparison to the conditioning applied through $k_{\gamma_1} = k_{\gamma_2}$ for $\mathcal{C}_{2,j}$ and $\mathcal{C}_{3,j}$, the sides of Sym are formed independently of the connected components of γ_1 and γ_2 ; a combination of monotonicity of μ , in addition to $(\mathcal{S} \text{ SMP})$ through an equal partition of the incident layer outside of Sym equally into two sets along which $+/-$ spin is constant.

After pushing boundary conditions towards Sym, we make use of rotational symmetry of Sym. In particular, the distribution of boundary conditions from the incident layer partition of 5.4.1 satisfies the following inequality,

$$\mu_{\Omega_{(L \cup R)^c}}^{\{\gamma_1, \gamma_2\}^c}[C_0 \mid \mathcal{R}] \leq \mu_{\text{Sym}}^{(\text{Top Half})}[C_0 \mid \mathcal{R}] \leq \mu_{\text{Sym}}^{(\text{Top Half})}[T_{\text{Sym}} \longleftrightarrow B_{\text{Sym}}] = \mu_{\text{Sym}}^{(\text{Top Half}) \frac{2\pi}{3}}[L_{\text{Sym}} \longleftrightarrow R_{\text{Sym}}] ,$$

where (Top Half) denotes wired boundary conditions along the top half of hexagonal Sym. Within the sequence of inequalities, the leftmost lower bound for $\mu_{\text{Sym}}^{\{L, R\}}[C_0 \mid \mathcal{R}]$ holds because $\Omega_{(L \cup R)^c} \subset \text{Sym}$, with $\{L, R\}$ denoting wired boundary conditions along L_{Sym} and R_{Sym} .⁴ The next lower bound for $\mu_{\text{Sym}}^{\{L, R\}}[T_{\text{Sym}} \longleftrightarrow B_{\text{Sym}}]$ holds because the event $\{T_{\text{Sym}} \xrightarrow{\text{Sym}} B_{\text{Sym}}\}$ depends on finitely many more edges in \mathbf{H} than $\{C_0 \mid \mathcal{R}\}$ does. Finally, the last inequality holds due to complementarity as in the argument for $\mathcal{C}_j \equiv \mathcal{C}_{2,j}$. $\{L, R\}$ denotes a $\frac{2\pi}{3}$ rotation of the boundary conditions supported over Sym.

More specifically, rotating the boundary conditions $\{L, R\}$ by $\frac{2\pi}{3}$ to obtain the boundary conditions $\{L, R\}^{\frac{2\pi}{3}}$ amounts to four $\frac{\pi}{6}$ rotations of Sym. With each rotation, the boundary conditions $\{L, R\}^{\frac{\pi}{6}}$ are obtained by rotating the partition of the incident layer along ∂Sym to its leftmost neighboring edge, in addition to modifications of the connectivity in $\mathcal{C}_{4,j}$.

Finally, the arguments imply the same result as in other cases, in which

$$\mu[\mathcal{C}_{4,j} \setminus (C_0 \cup C_2) \mid \mathcal{R}] \leq \mu_{\text{Sym}}^{(\text{Top Half}) \frac{2\pi}{3}}[L_{\text{Sym}} \longleftrightarrow R_{\text{Sym}}] .$$

We conclude the argument for 9*, not only having shown that the same inequality holds for a different classes of symmetric domains in the $\mathcal{C}_j \equiv \mathcal{C}_{4,j}$ case, but also that rotation of boundary conditions wired along the top half of Sym for top to bottom crossings can be used to obtain boundary conditions for left to right crossings.

5.4.3 Finishing the argument with $(\mathcal{S} \text{ CBC})$

We complete the argument by providing the following inequalities for each case. We make use of the special case of $(\mathcal{S} \text{ CBC})$ from Section 3.2, in which for $\mathcal{C}_j \equiv \mathcal{C}_{2,j}$, conditionally on top to bottom crossings \mathcal{C}_0 and \mathcal{C}_2 from 5.2.2, the pushforward below satisfies,

$$\mu[C_0 \mid \mathcal{C}_0 \cap \mathcal{C}_4] \geq \frac{1}{n^{k_{\tau'}(\sigma) - k_{\tau}(\sigma)} (x\sqrt{e})^{\text{Stretch}}} \mu[\mathcal{C}_j \setminus (C_0 \cup C_2) \mid \mathcal{C}_0 \cap \mathcal{C}_4] ,$$

⁴In contrast to square symmetric domains of [14] for the random cluster model, hexagonal Sym have two left sides and two right sides, and in turn require that boundary conditions along Sym be rotated by a different angle than $\frac{\pi}{2}$.

where the normalization to the crossing probability in the lower bound is dependent on the edge weight x . One obtains the same bound for crossings $\mathcal{C}_j \equiv \mathcal{C}_{4j}$. The bound above corresponds to the partition of boundary conditions . Finally, the existence of c such that the inequality in the statement of *Lemma 9** holds is of the form,

$$C = \{\text{Under construction}\},$$

because the union bound

$$\max\{\mu[\mathcal{C}_{2j}], \mu[\mathcal{C}_{3j}], \mu[\mathcal{C}_{4j}]: 0 \leq j < I\} \geq \frac{\mu[\mathcal{V}_{\mathcal{H}}]}{3I},$$

which is equivalent to the maximum of the crossing events taken over \mathcal{C}_{20} , \mathcal{C}_{30} and \mathcal{C}_{40} ,

$$\max\{\mu[\mathcal{C}_{20}], \mu[\mathcal{C}_{30}], \mu[\mathcal{C}_{40}]\} \geq \frac{\mu[\mathcal{V}_{\mathcal{H}}]}{3I},$$

holds if the maximum of each one of the crossing probabilities across 2_j or 3_j , across $3I$ events, in addition to the fact that the lower bound for the intersection \cap of crossing events is of the form,

$$\mu[C_0] \geq \mu[\mathcal{C}^1 \cap \mathcal{C}^2] \geq \left(\frac{\mu[\mathcal{V}_{\mathcal{H}}]}{3I}\right)^2,$$

where in the upper bound \mathcal{C}^1 can be any one of the crossings to a rightmost edge of \mathcal{H} , \mathcal{C}_{5j} or \mathcal{C}_{6j} , while \mathcal{C}^2 can be any one of the crossings to a leftmost edge of \mathcal{H} , \mathcal{C}_{2j} or \mathcal{C}_{3j} . \square

6 Wired boundary conditions induced by vertical crossings

To study behavior of the dilute Potts model in the *Continuous Critical* and *Discontinuous Critical* cases, we turn to studying vertical crossings under μ under wired boundary conditions. To denote vertical translates of hexagons containing H_j , we introduce $H_{j,j+\delta}$ as the hexagonal box whose center coincides with that of H_j , and is of side length $j + \delta$. We state the following Lemma and Corollary.

Lemma 10* (*volume of connected components*): For $x \in H_j$ and $C \geq 2$, there exists $\epsilon > 0$ such that, given $\mu_{H_{Cj}}^1[H_j \longleftrightarrow \partial H_{j,j+\delta}] < \epsilon$ for some k , in $H_j \cap H_{j,j+\delta}$ there exists a positive c satisfying,

$$\mu_{H_j}^1[\text{Vol(connected components in the annulus } H_j \cap H_{j,j+\delta}) = N] \leq e^{-cN},$$

for every $j, N \geq 2$, taken under wired boundary conditions.

*Proof of Lemma 10**. The arguments require use of hexagonal annuli which for simplicity we denote with $\mathcal{H}_{\mathcal{A}} \equiv H_j \cap H_{j,j+\delta}$, in which one hexagonal box is embedded within another (the same arrangement given in *Figure 5* for top to bottom crossings in $\mathcal{C}_j \equiv \mathcal{C}_{4j}$), and set $\mathcal{P} \equiv \{\text{Vol(connected components in the annulus } H_j \cap H_{j,j+\delta}) = N\}$. The existence of the quantity $\mu^{\mathcal{C}_l}$, where μ is a finite constant and \mathcal{C}_l is the number of connected components of length l is standard from [29]. To prove the statement, we measure the connected components of length l from the center of H_j in $\mathcal{H}_{\mathcal{A}}$.

From the connected components of x in H_j , we can restrict the connected components to the nonempty intersection given by $\mathcal{H}_{\mathcal{A}}$. The argument directly transfers from the planar case to the hexagonal one with little modification, as the restriction of the connected components \mathcal{C}_l of length l to the annulus implies the existence of a connected set of in \mathbf{H} , denoted with $S \subset \mathcal{H}_{\mathcal{A}}$ of vertex cardinality $N \setminus |H_j|$ from which a subset of the connected components $\mathcal{S}_{\mathcal{C}} \subset S$ can be obtained. We conclude the proof by analyzing the pushforward of \mathcal{P} under wired boundary conditions supported on H_j , in which the union bound below over \mathcal{J}_S satisfies,

$$\mu_{H_j}^1[\mathcal{P}] \leq \bigcup_{i \in \mathcal{J}_S = \{\text{connected components of size } l \text{ of } \mathcal{H}_{\mathcal{A}} \text{ in } S\}} \mu_{H_j}^1[\mathcal{P}_i] \leq \left(\mu_{H_j}^1[\mathcal{P}]\right)^{N \setminus |H_j|} \leq \left(\mu e^{|\mathcal{S}_C|}\right)^{N \setminus |H_j|} \leq e^{-cN},$$

where the union is taken over the collection of connected components under the criteria that admissible vertices from S are taken to be of distance $2j$ from one another in \mathcal{J}_S , and events $\mathcal{P}_{\mathcal{J}_S}$ denote measurable events under $\mu_{H_j}^1$ indexed by the number of admissible vertices from \mathcal{S}_C . We also apply $(\mathcal{S} \text{ SMP})$ and $(\mathcal{S} \text{ CBC})$ in the inequality above to push boundary conditions away, with ϵ arbitrary and small enough. \square

Next, we turn to the statement of the Corollary below which requires modification to vertical crossings across H_j , which can be accommodated with families of boxes H_j with varying height dependent on the usual RSW aspect ratio factor ρ . We also make use of $\mathcal{S}_{T,L} \equiv \mathcal{S}$.

Corollary 11* (*dilute Potts behavior outside of the supercritical and subcritical regimes*): For every $\rho > 0$, $L \geq 1$, there exists a positive constant \mathcal{C} satisfying the following, in which

- for the **Non(Subcritical)** regime, the crossing probability under wired boundary conditions of a horizontal crossing across \mathcal{H}_j supported over the strip, $\mu_{\mathcal{S}}^1[\mathcal{H}_{\mathcal{H}_j}] \geq \mathcal{C}$,
- for the **Non(Supercritical)** regime, the crossing probability under free boundary conditions of a vertical crossing across H_j , $\mu_{\mathcal{S}}^0[\mathcal{V}_{\mathcal{H}_j}] \leq 1 - \mathcal{C}$, also supported over the strip.

Proof of Corollary 11.* We present the argument for the first statement in **Non(Subcritical)** from which the second statement in **Non(Supercritical)** follows. For \mathcal{S} , in the **Non(Subcritical)** phase horizontal crossing probabilities across $\mathcal{S}_{T,L} \equiv \mathcal{S}$ are bound uniformly away from 0, which for μ can be demonstrated through examination of crossing events C_j first introduced in the *Proof of Proposition 8**. For , the result under which the pushforward with wired boundary conditions takes the form, for any $j \geq 1$,

$$\mu_{\mathcal{S}}^1[C_j] \geq 6e^{-c},$$

from an application of 10* to a connected component with unit volume in \mathcal{H} type annuli.

Also, in the following arrangement, we introduce a factor ρ for the aspect length of a regular hexagon in $\mathcal{S}_{T,L}$ which mirrors the role of ρ in RSW theory for crossings across rectangles. About the origin, we pushforward vertical crossing events on each side of $\mathcal{H}_j = \cup_i H_{j+\delta_i}$, respectively given by $H_{j+\delta_k}$ and $H_{j+\delta_l}$ for k such that $H_{j+\delta_k}$ and $H_{j+\delta_l}$ are of equal distance to the left and right of the origin. By construction, in any \mathcal{H}_j with the aspect length dependent on ρ , intermediate regular hexagons can be embedded within \mathcal{H}_j corresponding to the partition of the aspect length ρ . Longer horizontal or vertical crossings can be constructed through \star , which are exhibited below.

From the lower bound on the volume of a unit connected component, a vertical crossing across a hexagon of aspect height δ , from reasoning in \star can be bound below by FKG over δ_i translates of vertical crossings across hexagons of aspect height δ_i .

The measure under wired boundary conditions, for a vertical crossing \mathcal{V} across $H_{j+\delta_k}$, is

$$\mu_{\mathcal{H}_j}[\mathcal{V}_{H_{j+\delta_k}}],$$

supported over \mathcal{H}_j .

From the upper bound in \star , longer vertical horizontal crossings occur across 2^i vertical translates of shorter vertical crossings. The next ingredient includes making use of previous arrangements of horizontal translates of H_j , namely the left translate $H_{j-\delta'}$ and the right translate $H_{j+\delta'}$. Under the occurrence of vertical crossings across $H_{j+\delta_k}$ and $H_{j+\delta_l}$. From this event, to show that some box H_j in between $H_{j+\delta_k}$ and $H_{j+\delta_l}$ is crossed vertically, under wired boundary conditions supported over H_j we directly apply previous arguments from \star , with the exception that FKG is applied to a countable intersection of vertical, instead of horizontal, crossing events \mathcal{V} .

Conditionally, if vertical crossings in $H_{j+\delta_k}$ and $H_{j+\delta_l}$ occur about arbitrary $H_{j+\delta_i}$ with $k \leq i \leq l$, then the probability below satisfies, under wired boundary conditions,

$$\mu^1[\mathcal{V}_{H_{j+\delta_k}} \cap \mathcal{V}_{H_{j+\delta_l}}] \geq \mu_{\mathcal{H}_j}^1[\mathcal{V}_{H_{j+\delta_k}}] \cap \mu_{\mathcal{H}_j}^1[\mathcal{V}_{H_{j+\delta_l}}] = \mu_{\mathcal{H}_j}^1[\mathcal{V}_{H_{j+\delta_l}}]^2 \geq \prod_i \mu_{\mathcal{H}_j}^1[\mathcal{V}_{H_{j+\delta_{l_i}}}] = \left(\mu_{\mathcal{H}_j}^1[\mathcal{V}_{H_{j+\delta_{l_i}}}] \right)^{2^{1-i}}, \quad (\circ)$$

where \mathcal{V}_H denotes the vertical crossing across hexagons of aspect length which is the same as that of $H_{j+\delta_k}$, but with aspect height δ_{l_i} where $\delta_l = \cup_i \delta_{l_i}$. The union over i indicates a partition of the aspect height of $H_{j+\delta_l}$ into 2^{1-i} intervals. Finally,

$$\left(\mu_{\mathcal{H}_j}^1[\mathcal{V}_{H_{j+\delta_{l_i}}}] \right)^{2^{1-i}} \geq \left(e^{-c}\right)^{2^{1-i}}. \quad (\circ\circ)$$

The lower bound for the inequality above is obtained from an application of 10^* to the volume of a connected component from vertical crossings in $H_{j+\delta_k}$ and $H_{j+\delta_l}$. Between the second and third terms in \circ , monotonicity in the domain allows for a comparison between the measure under wired boundary conditions respectively supported over $H_{j+\delta_l}$ and \mathcal{H}_j .

From the partition of \mathcal{H}_j , to apply $(\mathcal{S} \text{ CBC})$ we consider the region between vertical crossings across $\mathcal{H}_{j+\delta_l}$ and $\mathcal{H}_{j+\delta_k}$. From the previous upper bound, given some u the vertical event $\{\mathcal{V}_{H_{j+\delta_k}} \cup \mathcal{V}_{H_{j+\delta_l}}\}$ about $H_{j+\delta_u}$ occurs for some $k, l < u$. Under wired boundary conditions, the conditional vertical crossing

$$\mu^1[\left(\mathcal{V}_{H_{j+\delta_{k-1}}} \cup \mathcal{V}_{H_{j+\delta_{l-1}}}\right) \mid \left(\mathcal{V}_{H_{j+\delta_k}} \cup \mathcal{V}_{H_{j+\delta_l}}\right)],$$

is bounded from below by the lower bound of $\circ \circ$. With conditioning on $\{\mathcal{V}_{H_{j+\delta_k}} \cup \mathcal{V}_{H_{j+\delta_l}}\}$, the probability of simultaneous vertical crossings in $H_{j+\delta_k}$ and $H_{j+\delta_l}$ and $j + \delta_k \equiv j + \delta_l$, the pushforward under wired boundary conditions of vertical crossings across two hexagons which entirely overlap with one another gives the upper bound

$$\mu_{\mathcal{H}_j}^1[\mathcal{V}_{\mathbf{1}_{\{j+\delta_k \equiv j+\delta_l\}}}] \geq \mu_{\mathcal{H}_j}^1[\mathcal{V}_{H_{j+\delta_k}} \cup \mathcal{V}_{H_{j+\delta_l}}] \prod_{i=1}^j \mu_{\mathcal{H}_j}^1[\left(\mathcal{V}_{H_{j+\delta_{k-1}}} \cup \mathcal{V}_{H_{j+\delta_{l-1}}}\right) \mid \left(\mathcal{V}_{H_{j+\delta_k}} \cup \mathcal{V}_{H_{j+\delta_l}}\right)] \geq e^{-c},$$

where the vertical crossing \mathcal{V} occurs when the indicator is satisfied. In the $\rho \rightarrow \infty$ limit, the finite volume measure over \mathcal{H}_j under the weak limit of measures yields a similar inequality

$$\mu_{\mathcal{S}}^1[\mathcal{V}_{\mathbf{1}_{\{j+\delta_k \equiv j+\delta_l\}}}] \geq \mu_{\mathcal{S}}^1[\mathcal{C}_0] \geq e^{-c},$$

with the exception that μ under wired boundary conditions is supported along the strip \mathcal{S} , and \mathcal{C}_0 denotes the crossing event in which hexagons to the right and left of \mathcal{H}_0 are crossed vertically. The exponential bound itself can be bounded below with the desired constant,

$$e^{-c} \geq \mathcal{C},$$

establishing the inequality for the Spin measure under wired boundary conditions. From the union of vertical crossings $\mathcal{V}_{H_{j+\delta_k}} \cup \mathcal{V}_{H_{j+\delta_l}}$, applying the μ homeomorphism under the conditions on c_0 in *Theorem 1**,

$$f(x) = 1 - c_0^{-c_0} + c_0^{-c_0}x,$$

for $x = \mu^1[\mathcal{V}]$ to the inequality for vertical crossings bounded below by \mathcal{C} implies that the upper bound of \mathcal{C} on can be translated into a corresponding upper bound dependent on \mathcal{C} for horizontal crossings, obtaining a similar upper bound under free boundary conditions,

$$\mu_{\mathcal{S}}^0[\mathcal{V}_{\mathcal{H}_j}] \leq 1 - \mathcal{C},$$

concluding the argument after having taken the infinite aspect length as $\rho \rightarrow \infty$ for a second time. From rotational symmetries in the 9* proof, there are six possible rotations from which C_j can occur, in which $\mathcal{C} \equiv \mathcal{C}_{2j}$, $\mathcal{C} \equiv \mathcal{C}_{3j}$ or $\mathcal{C} \equiv \mathcal{C}_{4j}$. Each upper bound under wired and free boundary conditions has been shown. \square

7 Vertical and horizontal strip densities

In this section, we make use of strip densities similar to those provided for the random cluster model in [14] (defined in 3.3) from which strip density and renormalization inequalities will be presented, in the infinite length aspect ratio limit. In the arguments below, we present boxes \mathcal{H} , \mathcal{H}_i and \mathcal{H}'_i across which horizontal and vertical crossings are quantified. For the lower bound of the conditional probability of obtaining no vertical crossings across each \mathcal{H}_i , we introduce a slightly larger hexagonal box $\mathcal{H}^{\text{Stretch}}$ which has an aspect height ratio **insert** times that of \mathcal{H}_j .

Definition 1* (*dilute Potts horizontal and vertical strip densities*): For $n \geq 1$, $x \leq \frac{1}{\sqrt{n}}$, $nx^2 \leq \exp(-|h'|)$, and (n, x, h, h') , with external fields h, h' , the strip density for horizontal crossings across \mathcal{H}_j under the Spin measure with free boundary conditions is,

$$p_n^\mu = \limsup_{\rho \rightarrow \infty} \left(\mu_{[0, \rho n] \times H[0, \lambda \text{Stretch}]}^0 [\mathcal{H}_{[0, \rho n] \times H[0, \lambda \text{Stretch}]}] \right)^{\frac{1}{\rho}},$$

while for vertical crossings across $\mathcal{H} + j$, under the Spin measure with wired boundary conditions, is,

$$q_n^\mu = \limsup_{\rho \rightarrow \infty} \left(\mu_{[0, \rho n] \times H[0, \lambda \text{Stretch}]}^1 [\mathcal{V}_{[0, \rho n] \times H[0, \lambda \text{Stretch}]}^c] \right)^{\frac{1}{\rho}}.$$

We denote $p_n \equiv p_n^\mu$ and $q_n \equiv q_n^\mu$. With these quantities, we prove the strip density formulas which describe how boundary conditions induced by vertical crossings under wired boundary conditions across $H_{j+\delta_k}, H_{j+\delta_l} \subset \mathcal{H}_j$ relate to horizontal crossings under free boundary conditions.

In the proof below, we make use of arguments from 11* to study vertical crossings across hexagons, and through applications of (S SMP) and (S CBC). To prove 1*, we define additional crossing events as follows. First, the crossing event that three hexagons, with aspect width of \mathcal{H}_j and aspect length Stretch placed on top of each other, is pushed forwards to apply FKG type arguments from \star over a countable intersection of horizontal crossings across hexagons with the same aspect height and smaller aspect length than that of \mathcal{H}_j . We denote this event with \mathcal{E} . Second, we also need the event of obtaining a horizontal crossing across $H_{j,j+\delta}$ and $H_{j,j-\delta}$, conditioned on \mathcal{E} which we denote as $\{\mathcal{F}|\mathcal{E}\}$. We study the conditions under which wired boundary conditions distributed from a prescribed distance of $H_{j,j-\delta}$ and $H_{j,j+\delta}$ induce vertical crossings. Third, crossing events across a larger domain than those considered in $\{\mathcal{F}|\mathcal{E}\}$ are formulated by making use of the monotonicity in the domain assumption, denoted as \mathcal{G} which is independent of ρ .

Fourth, the intersection of the previous three events is pushed forwards, and by virtue of (S SMP) and (S CBC), yields a strip inequality relating p_n to q_n , and q_n to p_n . In infinite aspect length as $\rho \rightarrow \infty$, inequalities corresponding to the horizontal and vertical strip densities are presented.

Proof of Lemma 1.* The argument consists of six parts; we fix $\lambda \in \mathbf{N}$, $n \in 3\mathbf{N}$. As a matter of notation, below we denote each of the three boxes below as the Cartesian product of the aspect length and height ratios, and let $\rho \rightarrow \infty$ in the last step. In the boxes \mathcal{H} , \mathcal{H}_i and \mathcal{H}'_i below, λ is taken smaller relative to ρ . Under the definitions of \mathcal{E} , $\{\mathcal{F}|\mathcal{E}\}$ and \mathcal{G} , we first define all hexagonal boxes across which horizontal crossings occur, which are defined as,

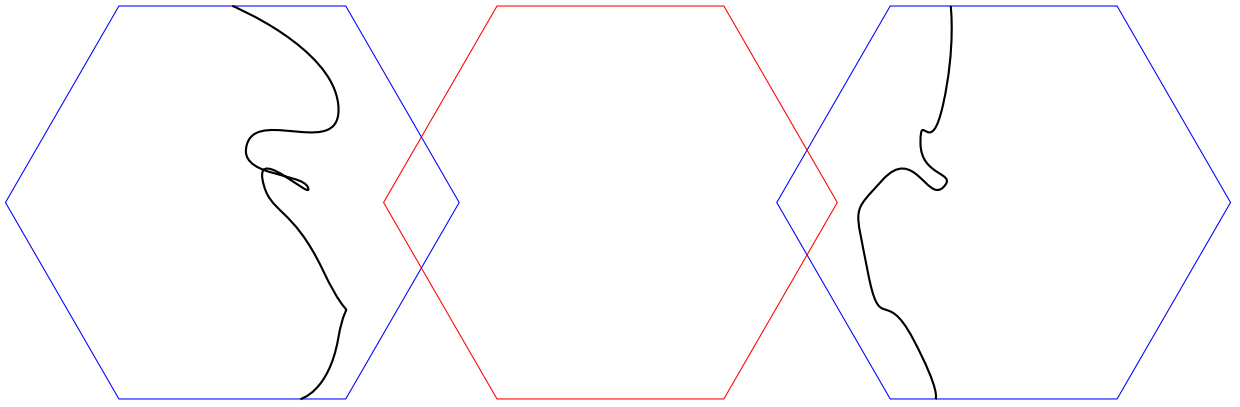


Figure 6: Vertical crossings across $H_{j+\delta_l}$ and across $H_{j+\delta_k}$ within the box \mathcal{H}_j (not shown). Under such vertical crossings, boundary conditions are induced for any hexagon between the right and leftmost ones, which is studied under the event $\mathcal{V}_{H_{j+\delta_{k-1}}} \cup \mathcal{V}_{H_{j+\delta_{l-1}}}$ in the 11* proof. In the case that the region over which the vertical crossings in the leftmost and rightmost hexagons overlap completely, the pushforward of \mathcal{V}_1 under wired boundary conditions dominates the pushforward of under wired boundary conditions.

$$\begin{aligned}\mathcal{H} &= [0, \rho n] \times_H [0, (2\lambda) \text{Stretch} + \text{Stretch}] , \\ \mathcal{H}_i &= [0, \rho n] \times_H [(2i) \text{Stretch} + \text{Stretch}, (2i) \text{Stretch} + 2 \text{Stretch}] , \\ \mathcal{H}'_i &= [0, \rho n] \times_H [(2i) \text{Stretch}, (2i) \text{Stretch} + \text{Stretch}] ,\end{aligned}$$

for every $0 \leq i \leq \lambda - 1$. The product \times_H denotes that a hexagon is formed from the aspect dimensions above. In the construction, the aspect length is the same as that of \mathcal{H} , while the aspect height of each box is partitioned in i relative to the scaling of the Stretch factor. Also, a final box with the Stretch scaling itself will be defined,

$$\mathcal{H}_{\text{Stretch}} = [0, \rho n] \times_H [0, n \lambda \text{Stretch}] ,$$

which is supported over which the spin measure with wired bound conditions for a lower bound of $\mu_{\mathcal{H}}^1[\mathcal{F} \mid \mathcal{E}]$, and n is an integer parameter. Second, to apply \star reasoning used in several previous arguments, if $\mathcal{H}_{\mathcal{D}}$ denotes a horizontal crossing across a finite domain \mathcal{D} of \mathcal{S} , we make use of $\mathcal{H}, \mathcal{H}_i, \mathcal{H}'_i \subset \mathcal{D}$ with smaller aspect lengths across which horizontal crossings occur. The lower bound for applying the FKG inequality across a countable family of horizontal crossings $\mathcal{H}_{\mathcal{H}_i}$ is,

$$\mu_{\mathcal{H}}^1[\mathcal{E}] \geq \mu_{\mathcal{H}}^1[\bigcap_{0 \leq i \leq \lambda-1} \mathcal{H}_{\mathcal{H}_i}] \geq \prod_{0 \leq i \leq \lambda-1} \mu_{\mathcal{H}}^1[\mathcal{H}_{\mathcal{H}_i}] \geq \prod_{0 \leq i \leq \lambda-1} \left(\frac{1}{\lambda_i^C}\right)^\rho \geq \left(\frac{1}{\lambda^C}\right)^{\lambda \rho} ,$$

with the existence of the lower bound guaranteed by *Corollary 11**, and λ is the minimum amongst all λ_i . Before letting $\rho \rightarrow \infty$, pushing forwards the horizontal crossing event across $\mathcal{H} \subset \mathcal{D}$ under wired boundary conditions for vertical crossings across \mathcal{H}'_i gives,

$$\mu_{\mathcal{H}}^1[\mathcal{F} \mid \mathcal{E}] \geq \mu_{\mathcal{H}'_i}^1[\bigcap_{0 \leq i \leq \lambda} \mathcal{V}_{\mathcal{H}'_i}^c] \geq \prod_{0 \leq i \leq \lambda-1} \mu_{\mathcal{H}'_i}^1[\mathcal{V}_{\mathcal{H}'_i}^c] \geq \left(\mu_{[0, \rho n] \times_H [0, n_1 \lambda \text{Stretch}]}^1[\mathcal{V}_{[0, \rho n] \times_H [0, n_1 \lambda \text{Stretch}]}^c] \right)^{\lambda+1} ,$$

for $n_2 > n_1$, by virtue of applications of $(\mathcal{S} \text{ SMP})$, monotonicity in the domain, and \star reasoning applied to vertical crossing events, instead of horizontal crossing events.

By construction of \mathcal{E} , the following lower bound for the conditional event $\{\mathcal{F} \mid \mathcal{E}\}$,

$$\begin{aligned} \mu_{\mathcal{H}}^1[\mathcal{E} \cap \mathcal{F} \cap \mathcal{G}] &= \mu_{\mathcal{H}}^1[(\mathcal{E} \cap \mathcal{F}) \cap \mathcal{G}] \stackrel{\text{FKG}}{\geq} \mu_{\mathcal{H}}^1[\mathcal{E} \cap \mathcal{F}] \mu_{\mathcal{H}}^1[\mathcal{G}] = \left(n^{k_{\mathcal{G}}(\sigma)} e^{(2\lambda)\text{Stretch} + \text{Stretch}} x^{2\{(2\lambda)\text{Stretch} + \text{Stretch}\}} \right) \mu_{\mathcal{H}}^1[\mathcal{E} \cap \mathcal{F}] \\ &= n^{k_{\mathcal{G}}(\sigma)} \left(x\sqrt{e} \right)^{(2\lambda)\text{Stretch} + \text{Stretch}} \mu_{\mathcal{H}}^1[\mathcal{E} \cap \mathcal{F}], \end{aligned} \quad (\star\star\star)$$

where the edge weight in the lower bound is representative of additional weights in the configuration supported under the wired Spin measure over \mathcal{H} . In the exponent of the edge weight x , by definition the number of connected components in a \pm configuration σ sampled under μ ,

$$k_{\mathcal{G}}(\sigma) = \sum_{k \text{ cc}'s} \left(\sum_{u \sim v} \mathbf{1}_{\{\sigma_{u_k} = \sigma_{v_k}\}} + 1 \right),$$

where the summation is taken over all connected components k so that \mathcal{G} occurs, and all neighboring vertices u and v with the same \pm spin, clearly impacting the number of connected components counted under σ .

Before completing the next step, we combine the estimates on $\mu_{\mathcal{H}}^1[\mathcal{E}]$ and $\mu_{\mathcal{H}}^1[\mathcal{F} | \mathcal{E}]$ to obtain the strip inequality between horizontal and vertical crossings. The following comparison amounts to making use of (S SMP) and (MON) to establish the following. First, we know that the measure $\mu_{\mathcal{S}}^1[\cdot]$ can be bound above with,

$$\mu_{\mathcal{S}}^1[\mathcal{E} \cap \mathcal{F} \cap \mathcal{G}] \leq \mu_{\mathcal{S}}^1[\mathcal{E} | \mathcal{F} \cap \mathcal{G}] \leq \left(\mu_{[0, \rho n] \times H[0, n_2 \lambda \text{Stretch}]}^0 [\mathcal{H}_{[0, \rho n] \times H[0, n_3 \lambda \text{Stretch}]}] \right)^\lambda,$$

because the event in the upper bound is more likely to occur than the event in the lower bound, in addition to \star reasoning for λ horizontal crossings, each event of which has equal probability, across $[0, \rho n] \times H[0,]$, and $n_3 > n_2$. Also, the upper bound to the conditional probability $\mu_{\mathcal{S}}^1[\mathcal{E} | \mathcal{F} \cap \mathcal{G}]$ above is established by making the comparison between measures with free boundary conditions. In comparison to the planar case, modifications to the argument with (S SMP), while other properties of the random cluster measure ϕ directly apply.

In light of the lower bound in $\star\star\star$ dependent on the edge weight x and Stretch, we consider the horizontal pushforward from the previous upper bound with free boundary conditions,

$$\mu_{[0, \rho n] \times H[0, n_2 \lambda \text{Stretch}]}^0 [\mathcal{H}_{[0, \rho n] \times H[0, n_1 \lambda \text{Stretch}]}],$$

which can be bound below by establishing comparisons between the measure under wired boundary conditions supported over a smaller hexagonal domain,

$$\mu_{[0, \rho n] \times H[0, n_1 \lambda \text{Stretch}]}^1 [\mathcal{V}_{[0, \rho n] \times H[0, n_1 \lambda \text{Stretch}]}^c],$$

as a consequence yielding one estimate for the vertical strip density,

$$\begin{aligned} &\left(\mu_{[0, \rho n] \times H[0, n_2 \lambda \text{Stretch}]}^0 [\mathcal{H}_{[0, \rho n] \times H[0, n_1 \lambda \text{Stretch}]}] \right)^\lambda \xrightarrow{\rho \rightarrow \infty} \left(p \text{Stretch } n \right)^\lambda \geq \\ &\left(\mu_{[0, \rho n] \times H[0, n_1 \lambda \text{Stretch}]}^1 [\mathcal{V}_{[0, \rho n] \times H[0, n_1 \lambda \text{Stretch}]}^c] \right)^{\lambda+1} \xrightarrow{\rho \rightarrow \infty} \frac{1}{\lambda^C} \left(q \text{Stretch } n \right)^{\lambda+1}, \end{aligned}$$

due to the fact that $\mathcal{T} = n^{\frac{k_{\mathcal{G}}(\sigma)}{\lambda\rho}} x^{\frac{(2\lambda)\text{Stretch} + \text{Stretch}}{\lambda\rho}} e^{\frac{(2\lambda)\text{Stretch} + \text{Stretch}}{2\lambda\rho}} \rightarrow 1$ as $\rho \rightarrow \infty$, and cancellations of λ crossings in the inequality gives,

$$p_{\text{Stretch } n} \geq \frac{1}{\lambda^C} \left(q_{\text{Stretch } n} \right)^{\text{Stretch} + \frac{\text{Stretch}}{\lambda}},$$

resulting from $(\mathcal{S} \text{ CBC})$, as in the region below the connected component of the path associated with the crossing $\mathcal{H}_{\mathcal{H}}$ the induced boundary conditions dominate the measure supported over a smaller domain under wired boundary conditions.

The strip inequality for horizontal and vertical crossings is finally achieved by taking each side of the inequality to the power $\frac{1}{\rho\lambda}$, which preserves the direction of the inequality as a monotonic decreasing transformation. As $\rho \rightarrow \infty$, we recover the peculiar definition of the horizontal strip density, while the other inequality corresponding to the vertical crossing density can be easily achieved by following the same argument, with the exception of the inequalities leading to the final estimate for vertical crossing events instead of horizontal ones. \square

8 Pushing lemma

We turn to the following estimates. In Lemmas 13* and 14* below, $\bar{\mathcal{H}}$ denotes the box with aspect length ρn , and variable aspect height defined for each box in the proof. To prove *Lemma 13** (see below), we make use of the following property for the Spin measure. With the Pushing Lemma, we provide arguments for the renormalization inequalities in the next section.

Property (*Finite energy for the Spin measure*, [8]): For any $\tau \in \{-1, 1\}^T$ and $\sigma \in \Sigma(G, \tau)$, $\mu_{G, n, x, h, h'}^\tau[\sigma] \geq \epsilon^{|G|}$, for any $\epsilon > 0$ depending only on (n, x, h, h') .

8.1 Statement

Lemma 13* (Pushing Lemma): There exists positive c , such that for every $n \geq 1$, with aspect length ρ , one of the following two inequalities is satisfied,

$$\mu_{\mathcal{H}}^{\text{Mixed}}[\mathcal{H}_{\mathcal{H}}] \geq c^\rho, \quad (\text{PushPrimal})$$

or,

$$\mu_{\mathcal{H}}^{(\text{Mixed})'}[\mathcal{V}_{\mathcal{H}}^c] \geq c^\rho, \quad (\text{PushDual})$$

for every $\rho \geq 1$, and the superscript Mixed denotes wired boundary conditions along the left, top and right sides of $\bar{\mathcal{H}}$, and free boundary conditions elsewhere. \mathcal{H} is the same hexagonal box used in previous arguments for *Lemma 1**. Under the PushDual condition, the analogous statement holds for the complement of vertical crossings across \mathcal{H} , under dual boundary conditions $(\text{Mixed})'$ to Mixed.

Lemma 14* (Pushforward of horizontal and vertical crossings under mixed boundary conditions): There exists positive c such that for every $n \geq 1$, with aspect length ρ , one of the following two inequalities is satisfied,

$$\mu_{\mathcal{S}}^{(\text{Mixed})'}[\mathcal{H}_{\mathcal{H}}] \geq c^\rho, \quad (\text{PushPrimal Strip})$$

or,

$$\mu_{\mathcal{S}}^{(\text{Mixed})'}[\mathcal{V}_{\mathcal{H}}^c] \geq c^\rho, \quad (\text{PushDual Strip})$$

for every $\rho \geq 1$. $(\text{Mixed})'$ denote the same boundary conditions from 13*, which manifest in the following.

8.2 14* arguments

Proof of Lemma 14.* With some abuse of notation, we denote the hexagonal boxes for this proof as,

$$\mathcal{H}_i = [0, 2n] \times_H \left[\frac{i}{3}n, \frac{i+1}{3}n \right],$$

for $i = 0, 1, 2$. Furthermore, we introduce the vertical segments along the bottom of each \mathcal{H}_i , and hexagons with same aspect length as those of each \mathcal{H}_i , in addition to hexagon of the prescribed aspect height below, respectively,

$$\begin{aligned}\mathcal{I}_i &= \left[\frac{i}{3}n, \frac{i+1}{3}n \right] \times \{0\}, \\ \mathcal{K}_i &= \left[\frac{i}{3}n, \frac{i+1}{3}n \right] \times_H [-n, n],\end{aligned}$$

each of which are also indexed by i , with the exception that i also runs over $i = 4, 5$. Before presenting more arguments for the connectivity between \mathcal{I}_1 and \mathcal{I}_4 , suppose that either $\mu_S^{(\text{Mixed})'}[\mathcal{V}_{\mathcal{H}_i}] \geq \frac{1}{6}$, or $\mu_S^{(\text{Mixed})'}[\mathcal{H}_{\mathcal{H}_i}^c] \geq \frac{1}{6}$ for some i . In the first case for the pushforward of vertical crossings in \mathcal{H}_i , another application of the μ homeomorphism f from arguments to prove *Corollary 11** implies that PushPrimal Strip holds, while in the second case for the pushforward of horizontal crossings in \mathcal{H}_i , an application of the same homeomorphism implies that PushDual Strip holds. By complementarity, under $\mu_S^{(\text{Mixed})'}[\cdot]$, the pushforward of the following events respectively satisfy the lower bounds, as $\mu_S^{(\text{Mixed})'}[\mathcal{V}_{\mathcal{H}_i}^c] \geq \frac{5}{6}$, and $\mu_S^{(\text{Mixed})'}[\mathcal{H}_{\mathcal{H}_i}] \geq \frac{5}{6}$. The same argument that follows applies to lower bounds for crossing probabilities by other constants than $\frac{1}{6}$ or $\frac{5}{6}$, and the modifications to obtaining identical lower bounds in place of different constants are provided.

With such estimates, under the same boundary conditions listed in PushPrimal Strip & PushDual Strip, the Spin measure satisfies

$$\mu_S^{(\text{Mixed})'}[\mathcal{V}_{\mathcal{H}_0}^c \cap \mathcal{H}_{\mathcal{H}_1} \cap \mathcal{V}_{\mathcal{H}_2}^c] \leq \mu_S^{(\text{Mixed})'}[\mathcal{H}_{\mathcal{H}_1}] \leq \mu_{\mathcal{H}}^{*(\text{Mixed})'}[\mathcal{H}_{\mathcal{H}_1}],$$

where the upper bound for the probability of the intersection of the three events above only holds under boundary conditions in which the incident layer to the configuration (as given in arguments for the proof of *Lemma 9**), the boundary conditions for the measure dominating (Mixed)' boundary conditions holds because every vertex that is wired in the (Mixed)' boundary conditions is also wired in the boundary conditions for the pushforward in the upper bound. Moreover, the partition of boundary vertices in the boundary conditions for the upper bound is composed of the arc that is wired in the boundary conditions for , in addition to a singleton

Under the (Mixed)' boundary conditions, the conditional probability

$$\mu_S^{\text{Mixed}}[\mathcal{I}_1 \xleftrightarrow{\mathcal{H}} \mathcal{I}_4 | \mathcal{H}_{\mathcal{H}_1}],$$

can be bound below by conditioning on a horizontal crossing $\mathcal{H}_{\mathcal{H}_1}$ across \mathcal{H}_1 . In particular, conditionally on $\mathcal{H}_{\mathcal{H}_1}$, the connectivity event

$$\mu_S^{(\text{Mixed})'}[\mathcal{I}_1 \xleftrightarrow{\mathcal{K}_1} \mathcal{I}_4 | \mathcal{H}_{\mathcal{H}_1}], \quad (\square)$$

can be bounded below through applications of (\mathcal{S} CBC) and (\mathcal{S} SMP). Each property is applied as follows; for (\mathcal{S} SMP), we make use of previous partitions of the incident layer of hexagons to a configuration, in which (\mathcal{S} SMP) can only be applied when the outermost layer of a configuration can be partitioned into two equal sets over which the \pm spin is constant.

Concluding, we apply standard arguments for the crossing event below through a lower bound dependent on a conditional probability,

$$\begin{aligned} \mu_S^{\text{Mixed}}[\mathcal{I}_1 \xleftrightarrow{\mathcal{H}} \mathcal{I}_4] &\geq \mu_S^{\text{Mixed}}[\mathcal{I}_1 \xleftrightarrow{\mathcal{H}} \mathcal{I}_4 \mid \mathcal{H}_{\mathcal{H}_i}] \mu_S^{\text{Mixed}}[\mathcal{H}_{\mathcal{H}_i}] \geq \frac{5}{6} \mu_S^{\text{Mixed}}[\mathcal{I}_1 \xleftrightarrow{\mathcal{H}} \mathcal{I}_4 \mid \mathcal{H}_{\mathcal{H}_{[0, \rho n] \times H}}] \\ &\geq \frac{5}{6} \textcolor{blue}{Underconstruction} \frac{1}{\prod_i (n^{k_i} x_i)^{\text{Stretch}_i} (\sqrt{e})^{\text{Stretch}}} , \end{aligned}$$

from which \star reasoning à la FKG for the countable intersection, dependent on i , of horizontal crossings across hexagons of small enough aspect length. The inverse proportionality in the lower bound is dependent on the product \mathcal{T} , defined in the proof for *Lemma 1** on page 21, with i running over two configurations with respective number of connected components $k_1 + 1$ and $k_2 + 1$. The lower bound dependent on the edge weight x arises from multiple applications of $(S \text{ SMP})$ and (MON) , in which the modification to (SMP) from the random cluster model argument with $(S \text{ SMP})$ for the Spin Measure results in comparisons between \pm configurations and partitions of the incident layer as described in 5.2.

Instead, if we suppose that the lower bounds for $\mu_S^{(\text{Mixed})'}[\mathcal{V}_{\mathcal{H}_i}^c] \geq c$ for real c instead of $\frac{5}{6}$, the lower bound on the second line above takes the form,

$$c \mu_S^{\text{Mixed}}[\mathcal{I}_1 \xleftrightarrow{\mathcal{H}} \mathcal{I}_4 \mid \mathcal{H}_{\mathcal{H}_i}] \geq c \textcolor{blue}{Underconstruction} .$$

due to the fact that the boundary conditions from the special case of the inequality, where the power to which the product of the edge weight and difference in monochromatically colored triangles is raised to the aspect ratio Stretch of $\mathcal{H}_{\text{Stretch}}$, and the number of connected components in the exponent of n is the difference between the number of connected components of a \pm configuration respectively sampled under $\mu_S^{(\text{Mixed})'}$ and $\mu_{\mathcal{H}}^{*(\text{Mixed})'}$.

Furthermore, the lower bound dependence on the edge weight x, n and e , emerges from an application of FKG to the pushforward below of two events,

$$\textcolor{blue}{Underconstruction} ,$$

each of which have equal probability, concluding the proof. \square

8.3 13* arguments

Proof of Lemma 13.* We show that either PushPrimal Strip \Rightarrow PushPrimal, or that PushDualStrip \Rightarrow PushDual. Without loss of generality, suppose that PushDual Strip holds; to show that PushDual holds, we introduce the following collection of similarly defined boxes from arguments in 14* on the previous page,

$$\widetilde{\mathcal{H}}_i = [0, \rho n] \times_H \left[\frac{i}{3}n, \frac{i+1}{3}n \right] ,$$

for $1 \leq i \leq N$, with N sufficiently large. Under $(\text{Mixed})'$ boundary conditions,

$$\mu_S^{(\text{Mixed})'}[\mathcal{V}_{\widetilde{\mathcal{H}}_N}^c] \geq c^\rho ,$$

the probability of a complement of the vertical crossing across $\widetilde{\mathcal{H}}_N$, and can be bounded below by c^ρ because by assumption PushPrimal Strip holds. Clearly, the probability of obtaining a vertical crossing across the last rectangle over all i can be determined by applying the FKG inequality across each of the N smaller hexagons, yielding an upper bound of $c^{N\rho}$ to the probability of obtaining a longer N -hexagon crossing.

Next, with similar conditioning on horizontal crossings in previous arguments, the probability of a horizontal crossing across $\widetilde{\mathcal{H}}_i$, given the occurrence of a horizontal crossing across $\widetilde{\mathcal{H}}_{i+1}$, satisfies for every i ,

$$\mu_S^{(\text{Mixed})'}[\mathcal{V}_{\widetilde{\mathcal{H}}_i}^c \mid \mathcal{V}_{\widetilde{\mathcal{H}}_{i+1}}^c] \geq c^\rho ,$$

with the exception that the pushforward $\widetilde{\mathcal{H}}_{i+1}$, taken under (Mixed)' boundary conditions, in comparison to previous arguments for the wired pushforward

$$\mu_{\mathcal{H}_j}^1 [\mathcal{V}_{\{j+\delta_k \equiv j+\delta_l\}}] ,$$

below by e^{-c} for *Corollary 11**, can also be applied to bound the intersection of conditional events, for the event $\{\mathcal{V}_{\widetilde{\mathcal{H}}_i}^c | \mathcal{V}_{\widetilde{\mathcal{H}}_{i+1}}^c\}$, for all i ,

$$\prod_{0 \leq i \leq N} \mu_{\widetilde{\mathcal{H}}}^{(\text{Mixed})'} [\mathcal{V}_{\widetilde{\mathcal{H}}_i}^c | \mathcal{V}_{\widetilde{\mathcal{H}}_{i+1}}^c] \geq \left(c^\rho \right)^N ,$$

implying that the identical lower bound from the PushPrimal Strip holds, across the countable intersection of horizontal crossings,

$$\mu_{\widetilde{\mathcal{H}}}^{(\text{Mixed})'} [\mathcal{V}_{\widetilde{\mathcal{H}}_1}^c] \geq c^{N\rho} .$$

We conclude the argument, having made use of the previous application of FKG across $0 \leq i \leq \lambda - 1$, uniformly in boundary conditions (Mixed)'. \square

9 Renormalization inequality

We now turn to arguments for the Renormalization inequality. We make use of notation already given in the proof for the vertical and horizontal strip inequalities of *Lemma 1**, namely that we make use of a similar partition of the hexagons to the left and right of some \mathcal{H} . To restrict the crossings to occur across hexagons of smaller aspect length, we change the assumptions on our choice of n , and follow the same steps in the argument of *Lemma 1** to obtain a lower bound for the pushforward $\mu_{\mathcal{H}}^1 [\tilde{\mathcal{E}} \cap \mathcal{F} \cap \mathcal{G}]$, where $\tilde{\mathcal{E}}$ denotes the event that each of the three boxes $\widetilde{\mathcal{H}}_i, \widetilde{\mathcal{H}}_i^+, \widetilde{\mathcal{H}}_i^-$ which are defined in arguments below. The partition of the aspect length of $\widetilde{\mathcal{H}}_i, \widetilde{\mathcal{H}}_i^+, \widetilde{\mathcal{H}}_i^-$ is dependent on i . Also, the smaller scale over which we force the horizontal crossings to occur in $\tilde{\mathcal{E}}$ is reflected in the partition of the aspect length, which not surprisingly permits for \star reasoning for $0 \leq i \leq \lambda - 1$. The partition of \mathcal{H}_i into the three boxes $\widetilde{\mathcal{H}}_i, \widetilde{\mathcal{H}}_i^+, \widetilde{\mathcal{H}}_i^-$ determines corresponding powers, dependent on λ to which the horizontal or vertical strip densities are raised before taking $\rho \rightarrow \infty$. As previously mentioned, differences in (S SMP) emerge in one step of the following argument. We discuss the arguments for the proof when PushPrimal holds, and in the remaining case when PushDual holds, a modification to the argument is provided.

9.1 2^* arguments

*Proof of Lemma 2**. Suppose that PushDual holds; the PushPrimal case will be discussed at the end. In light of the brief remark of the argument at the beginning of the section, we introduce the three boxes to partition the middle of \mathcal{H}_i from the 1^* proof,

$$\begin{aligned} \widetilde{\mathcal{H}}_i &= [0, \rho n] \times_H [(2i) \text{ Stretch} + \text{Stretch} + () \text{ Stretch} , (2i) \text{ Stretch} + 2 \text{ Stretch} + () \text{ Stretch}] , \\ \widetilde{\mathcal{H}}_i^+ &= [0, \rho n] \times_H [(2i) \text{ Stretch} + \text{Stretch} + () \text{ Stretch} , (2i) \text{ Stretch} + 2 \text{ Stretch} + () \text{ Stretch}] , \\ \widetilde{\mathcal{H}}_i^- &= [0, \rho n] \times_H [(2i) \text{ Stretch} + \text{Stretch} + () \text{ Stretch} , (2i) \text{ Stretch} + 2 \text{ Stretch} + () \text{ Stretch}] , \end{aligned}$$

for every $0 \leq i \leq \lambda - 1$, and will apply steps of the argument from the proof of *Lemma 1**, in which we modify all pushforwards under the prescribed boundary conditions for $\tilde{\mathcal{E}}$. Briefly, we recall the steps with the sequence of inequalities below. Under one simple modification through the lower bound, applying FKG as in \star implies,

$$\mu_{\mathcal{H}}^1[\tilde{\mathcal{E}}] \geq \prod_{0 \leq i \leq \lambda-1} \mu_{\mathcal{H}_i}^1[\mathcal{H}_{\mathcal{H}_i}] \geq \left(\frac{1}{(\lambda')^C}\right)^{\lambda\rho},$$

from which the conditional probability dependent on $\tilde{\mathcal{E}}$ can be bound from below as follows,

$$\mu_{\mathcal{H}}^1[\mathcal{F} | \tilde{\mathcal{E}}] \geq \prod_{0 \leq i \leq \lambda-1} \mu_{\mathcal{H}_i}^1[\mathcal{V}_{\mathcal{H}_i}^c] \geq \left(\mu_{[0, \rho n] \times_H [0, n_1 \lambda \text{Stretch}]}^1[\mathcal{V}_{\times_H}^c]\right)^{\lambda+1}.$$

Further arguments result in the following lower bound for the probability of $\{\tilde{\mathcal{E}} \cap \mathcal{F} \cap \mathcal{G}\}$,

$$\mu_{\mathcal{H}}^1[\tilde{\mathcal{E}} \cap \mathcal{F} \cap \mathcal{G}] = \mu_{\mathcal{H}}^1[(\tilde{\mathcal{E}} \cap \mathcal{F}) \cap \mathcal{G}] \geq \mu_{\mathcal{H}}^1[\tilde{\mathcal{E}} \cap \mathcal{F}] \mu_{\mathcal{H}}^1[\mathcal{G}] = x^{k_{\mathcal{G}}(\sigma)} \left(x\sqrt{e}\right)^{(2\lambda)\text{Stretch}+\text{Stretch}} \mu_{\mathcal{H}}^1[\mathcal{E} \cap \mathcal{F}],$$

which is the same lower bound provided in $\star\star\star$. Also, under PushDual, the conditional pushforward under wired boundary conditions satisfies,

$$\mu_{\mathcal{H}}^1[\tilde{\mathcal{F}} | \tilde{\mathcal{E}} \cap \mathcal{F} \cap \mathcal{G}] \geq c^{\text{Underconstruction}^{\text{Stretch}}},$$

which will be used to complete the remaining steps from the 1^* proof. In particular, the intersection $\{\tilde{\mathcal{E}} \cap \mathcal{F} \cap \mathcal{G}\}$ can be bounded above by the product of λ horizontal crossings below, by \star reasoning

$$\mu_{\mathcal{H}}^1[\tilde{\mathcal{E}} \cap \tilde{\mathcal{F}} \cap \tilde{\mathcal{G}}] = \mu_{\mathcal{H}}^1[\tilde{\mathcal{F}} | \tilde{\mathcal{E}} \cap \mathcal{F} \cap \mathcal{G}] \mu_{\mathcal{H}}^1[\tilde{\mathcal{E}} \cap \mathcal{F} \cap \mathcal{G}] \geq c^{\text{Underconstruction}^{\text{Stretch}}} \mu_{\mathcal{H}}^1[\tilde{\mathcal{E}} \cap \mathcal{F} \cap \mathcal{G}],$$

through the same application of $(\mathcal{S} \text{ SMP})$ and (MON) , and where \mathcal{F} denotes the event that neither of the three hexagonal boxes defined at the beginning of the proof are vertically crossed. As a result, the last application of \star yields, for λ horizontal crossings across thinner hexagons,

$$\mu_{\mathcal{H}}^1[\tilde{\mathcal{E}} \cap \tilde{\mathcal{F}} \cap \mathcal{G}] \leq \left(\mu_{[0, \rho n] \times_H [0, 1]}^1[\mathcal{H}_1]\right)^{\lambda+1},$$

under free boundary conditions.

Finally, comparing the pushforward under free boundary conditions to the pushforward under wired boundary conditions yields, after taking the same infinite aspect length limit as in *Section 7*. From previous applications of $(\mathcal{S} \text{ SMP})$ and (MON) are used, in order to suitably compare boundary conditions, as a consequence imply a similar estimate as in *Section 7*,

$$\begin{aligned} & \left(\mu_{[0, \rho n] \times_H [0, n_2 \lambda \text{Stretch}]}^0[\mathcal{H}_{[0, \rho n] \times_H [0, n_1 \lambda \text{Stretch}]}]\right)^\lambda \xrightarrow{\rho \rightarrow \infty} \left(p_{\text{Stretch } n}\right)^\lambda \geq \\ & \left(\mu_{[0, \rho n] \times_H [0, n_1 \lambda \text{Stretch}]}^1[\mathcal{V}_{[0, \rho n] \times_H [0, n_1 \lambda \text{Stretch}]}^c]\right)^{\lambda+1} \xrightarrow{\rho \rightarrow \infty} \frac{1}{\lambda^C} \left(q_{\text{Stretch } n}\right)^{\lambda+1}, \end{aligned}$$

with the exception that the support of the measure with free (-) boundary conditions is over a hexagon with thinner aspect length. The result corresponds to the renormalization inequality for the horizontal crossing probability, concluding the argument under the PushDual assumption. Below, we briefly describe how the same sequence of inequalities applies for the remaining possibility.

Suppose that PushPrimal holds. Under this assumption, denote $\tilde{\mathcal{F}}$ as the crossing event that none of the boxes \mathcal{H}_i^\pm are vertically crossed. From this event, the assumption implies from the definition of the horizontal and vertical strip densities for the Spin Measure that the arguments to bound the conditional probability can be achieved by the same line of argument, possibly with larger C . \square

10 Quadrichotomy proof

In the final section we classify all possible behaviors of the model. Briefly, we remark that for the continuous critical case, the first part of the argument does not require use of (SMP) and (CBC) for original results in the random cluster model, implying that the entirety of the argument immediately applies. Briefly, we summarize the steps of the argument. We consider horizontal crossing events across a regular hexagon, pushed forwards under free boundary conditions for the Spin measure supported over a slightly larger hexagon. From knowledge of the longest edge in the + path of the horizontal crossing, removing the largest edge from the configuration easily yields a connectivity event along the common set of edges over a subgraph of the triangular lattice that excludes the length of the maximal edge along two points x and y . These steps demonstrate the ingredients for the *Discontinuous Critical* case, before obtaining the horizontal strip densities in the infinite aspect length limit as $\rho \rightarrow \infty$. For the discontinuous critical case, the second part of the argument requires use of (S CBC) and (MON). Before proceeding, we cite the following theorem which classifies the probability of obtaining loop configurations of fixed length in the model. In the following application of the inequalities, we choose an aspect ratio of hexagons dependent on ρ , from which horizontal and vertical crossings will be studied.

Theorem 3* (*Continuous & Discontinuous critical cases, behaviors of the dilute Potts model quadrichotomy, [8]*): For configurations distributed under the μ , for $n \geq 1$ and $x \leq \frac{1}{\sqrt{n}}$, one of the two possible behaviors occurs,

$$\mu_S^\tau[R \geq k] \leq \exp(-ck), \quad (\text{Exponential decay of } + \text{ paths})$$

where R is the diameter of the largest loop surrounding the origin, demonstrating that + paths are exponentially unlikely for any $k \geq 1$, or,

$$c \leq \mu_S^\tau[\text{there exists a } + \text{ path which horizontally crosses a rectangle over the triangular lattice}] \leq 1 - c, \quad (\text{RSW box-crossing property})$$

demonstrating that the RSW box-crossing property is satisfied. Each possibility holds for boundary conditions $\tau \in \{-1, +1\}^T$ and $c > 0$.

Observe that we have slightly rephrased the first condition provided in [8] which is stated instead for the loop measure P , of *Section 3.1*. The equivalent condition of obtaining a loop configuration whose largest diameter about the origin is k is equivalent to obtaining a path of + spins about the origin. From the statement of *Theorem 3**, we now study 2*.

*Proof of Theorem 2**. As mentioned at the beginning of the section, first suppose that the first possibility holds. To show that this condition implies that the phase transition is discontinuous, consider the following. Define a horizontal crossing across \mathcal{H} . From the existence of such an event, the longest edge in the crossing of arbitrary length L then excluding the length of this longest edge from the crossing implies that another closely related crossing event occurs across a subgraph of the triangular lattice which excludes the maximal edge with length L . Hence there exists vertices in a subgraph of the triangular lattice, such that the vertices x and y are connected by a + path in a hexagon of smaller aspect length that is not regular. Collecting these observations implies the following, where the upper and lower bounds of the inequality are taken under – boundary conditions, by the union bound,

$$\mu_{[0, \rho n] \times_H [0, 2n]}^0[\mathcal{H}_{[0, \rho n] \times_H [0, n]}] \leq c n^2 \mu_{[0, \rho n] \times_H [0, 2n]}^0[x^{[0, \rho n] \times_H [0, n]} \longleftrightarrow y],$$

where x and y are the vertices satisfying $x \in [, .] \times_H [,]$ and $y \in [, .]$, with c an arbitrary positive constant. For the next step, we introduce horizontal translates of x with $x_k = x + (4kn, 0)$. Across all horizontal translates of x , yields the following lower bound for the connectivity event between x and each x_k , by virtue of (MON) and FKG,

$$\mu_S^0[x \rightarrow x_k] \geq \mu_{[0, \rho n] \times_H [0, 2n]}^0[x^{[0, \rho n] \times_H [0, n]} \longleftrightarrow y].$$

From previous remarks, the first upper bound given in the proof dependent on c yields the inequality, as applied in ★ several times previously in the argument,

$$\mu_{\mathcal{S}}^0[x \longleftrightarrow x_k] \geq \frac{1}{cn^2} \left(\mu_{[0, \rho n] \times_H [0, 2n]}^0[\mathcal{H}_{[0, \rho n] \times_H [0, n]}] \right)^{2k},$$

from which taking the infinite limit as in previous arguments implies, for $k \rightarrow \infty$,

$$p_{2n}^2 \geq \frac{1}{cn^2} \mu_{[0, \rho n] \times_H [0, 2n]}^0[\mathcal{H}_{[0, \rho n] \times_H [0, n]}],$$

so that the pushforward of the spin measure under free boundary conditions satisfies the strip density estimate from the original definition provided in the beginning of *Section 7*, from the connected components of + paths from the occurrence of $\{x \longleftrightarrow \infty\}$. Finally, we observe that the upper bound for the horizontal strip density decays exponentially fast, implying that the pushforward in the lower bound taken under free boundary conditions does as well. As expected, to analyze the other possibility for infinitely long vertical crossings, repeating the same steps of the argument, with the exception that the horizontal crossing event is instead a vertical crossing event, simply yields a similar bound, from an application of 12* for some integer λ satisfying the conditions of the Lemma, that the probability of obtaining an infinitely long vertical crossings is an upper bound in the following inequality,

$$q_{2n}^2 \geq \frac{1}{cn^2} \left(1 - \mu_{[0, \rho n] \times_H [0, 2n]}^1[\mathcal{V}_{[0, \rho n] \times_H [0, 1]}^c] \right),$$

which nevertheless still exponential decays for the same reason as $k \rightarrow \infty$.

Under construction. Enter parafermionic observable.

11 References

- [1] Beffara, V. & Duminil-Copin, H. The self-dual point of the two-dimensional random-cluster model is critical for $q \geq 1$. *Probability Theory and Related Fields* **153** 511-542 (2012).
- [2] Beliaev, D., Muirhead, S. & Wigman, I. Russo-Seymour-Welsh estimates for the Kostlan ensemble of random polynomials. *Arxiv* (2017).
- [3] Crawford, N., Glazman, A., Harel, M. & Peled, R. Macroscopic loops in the loop $O(n)$ model via the XOR trick. *Arxiv* (2020).
- [4] Clarence, J., Damasco, G., Frettloh, D., Loquias, M. Highly Symmetric Fundamental Domains for Lattices in \mathbf{R}^2 and \mathbf{R}^3 . *Arxiv* (2018).
- [5] Duminil-Copin, H. Parafermionic observables and their applications to planar statistical physics models. *Ensaios Matematicos* **25** 1-371 (2013).
- [6] Duminil-Copin, H. Parafermionic observables and their applications. *AMP Bulletin* (2015).
- [7] Duminil-Copin, H. Sharp threshold phenomena in statistical physics. *Japanese Journal of Mathematics* **14** 1-25 (2019).
- [8] Duminil-Copin, H., Glazman, A., Peled, R. & Spinka, Y. Macroscopic Loops in the Loop $O(n)$ model at Nienhuis' Critical Point. *Arxiv*.
- [9] Duminil-Copin, H., Hongler, C. & Nolin, P. Connection probabilities and RSW-type bounds for the FK Ising Model. *Communications on Pure and Applied Mathematics* **64**(9) (2011).
- [10] Duminil-Copin, H., Manolescu, I. & Tassion, V. Planar random-cluster model: fractal properties of the critical phase. *Arxiv* (2020).
- [11] Duminil-Copin, H. & Smirnov, S. Conformal invariance of lattice models. *Arxiv* (2012).

- [12] Duminil-Copin, H. & Smirnov, S. The convective constant of the honeycomb lattice equals $\sqrt{2 + \sqrt{2}}$. *Annals of Mathematics* **175**(3) 1653-1665 (2012).
- [13] Duminil-Copin, H., Sidoravicius, V. & Tassion, V. Continuity of the phase transition for planar random-cluster and Potts models for $1 \leq q \leq 4$. *Communications in Mathematical Physics* **349** 47-107 (2017).
- [14] Duminil-Copin, H. & Tassion, V. Renormalization of crossing probabilities in the planar random-cluster model. *Arxiv*.
- [15] Feher, G. & Nienhuis, B. Currents in the dilute $O(n = 1)$ model. *Arxiv* 1510.02721v2 (2018).
- [16] Fradkin, E. Disorder Operators and their Descendants. *Lecture Notes*.
- [17] Glazman, A. & Manolescu, I. Uniform Lipschitz functions on the triangular lattice have logarithmic variations. *Arxiv* (2019).
- [18] Gheissari, R. & Lubetzky, E. Quasi-polynomial Mixing of Critical two-dimensional Random Cluster Models. *Random Structures & Algorithms* **56**(2) (2019).
- [19] Guo, W., Blote, H. & Nienhuis, B. First and Second Order Transitions in the Dilute $O(n)$ models *International Journal of Modern Physics* **10**(1) 291-300 (1999).
- [20] Guo, W., Blote, H. & Nienhuis, B. Phase Diagram of a Loop on the Square Lattice. *International Journal of Modern Physics* **10**(1) 301-308 (1999).
- [21] Hongler, C. Percolation on the triangular lattice. *Arxiv* (2007).
- [22] Nienhuis, B. & Guo, W. Tricritical $O(n)$ models in two dimensions. *American Physical Society* **78**, 061104 (2008).
- [23] Russo, L. A note on percolation. *Zeitschrift fur Wahrscheinlichkeitstheorie und Verwandte Gebiete* **43** 39-48 (1978).
- [24] Seymour, P. & Welsh, D. Percolation probabilities on the square lattice. *Annals Discrete Math.* **3** 227–245 (1978).
- [25] Smirnov, S. Discrete Complex Analysis and Probability. *Proceedings of the International Congress of Mathematicians* (2010).
- [26] Smirnov, S. Conformal invariance in random cluster models. I. Holomorphic fermions in the Ising model. *Annals of Mathematics* **172** 1435-1467 (2010).
- [27] Tassion, V. Crossing probabilities for Voronoi percolation. *The Annals of Probability* **44**(5) 3385-3398 (2016).
- [28] Zeng, X. A Russo Seymour Welsh Theorem for critical site percolation on \mathbf{Z}^2 . *Arxiv* (2013).
- [29] Grimmett, G. *Percolation*, Volume 321 of *Fundamental Principles of Mathematical Sciences*. Springer-Verlag, second edition (1999).

Variational quantum algorithm for extracting measurements from the Navier-Stokes, Euler and Poisson equations

Pete Rigas, McMahon Lab

December 1, 2020

1 Introduction

The variational quantum algorithm (VQA) has attracted wide attention from several computational disciplines in physics, chemistry and materials science [16], with recent studies demonstrating how optimizers for such algorithms can be improved and parametrized for entanglement [23,24], robust encoding in molecules for chemistry computations [1], various implementations for linear algebra problems [22,26], variance minimization [27], and the construction of quantum Gibbs states [6]. To further contribute to rapid developments, Lubasch et al [15] introduced a VQA which can be applied to solve nonlinear problem from various PDEs through specifications on quantum circuits including an optimized quantum nonlinear processing unit (QNPUs) to treat nonlinearities of the equation efficiently, in addition to variational states λ, λ_0 which are prepared in quantum circuits from a cost function $\mathcal{C}(\lambda, \lambda_0)$. In turn, quantum registers prepared in circuits of polynomial depth not only require exponentially fewer parameters than their classical counterparts but also allow for the algorithm to be applied to several other nonlinear problems [15].

To briefly expound upon the algorithm of [15], the algorithm is applied to NLS and the Burger's equation with MPS ansatzae of polynomial bond dimension [19,20]. These particular ansatzae are advantageous for quantum computation in their ability to be represented as a product of isometric matrices, which can be interpreted as the wave function of possible states that are initially imposed on the system through the ansatz before the algorithm is ran to obtain solutions, while also enjoying a two-qubit unitary decomposition that can always be embedded into circuits with polynomial depth. In comparison to cost functions obtained for NLS and the Burger's equations, the Navier-Stokes cost function involves quadratic terms in the magnitude of the time step of the evolution, constant terms directly proportional to the time step and inversely proportional to the Reynolds number, in addition to several other terms resulting from expectation values involving the discretized Nabla and Laplacian operators. We rearrange the cost function in the next section and make use of several identities to obtain expectation terms dependent on the pressure, which under different cases impacts the computation of pressure dependent expectation terms of the cost function. In turn, classical optimization routines will be introduced, in an effort to determine circuit arrangements over which the variational algorithm is capable of generating solutions to the Navier-Stokes equations for different classes of initial data. Modifications to the general requirements imposed on quantum circuits in [15] will be further described.

That is, to apply the hybrid algorithm to study nonlinearities and related behaviors of the Navier-Stokes equations, we optimize the Navier-Stokes cost function for time steps τ in conjunction with running quantum circuit computations given an ansatz. In the following implementation, different numerical aspects of the variational algorithm will be explored through disparate QNPUs, quantum circuits and ansatzae, with qualities of the QNPUs differing in how nonlinearities of the Navier-Stokes equations are treated; qualities of the quantum circuit construction differing in the number of quantum registers, and hence, variational parameters that need to be specified as the algorithm is executed for solutions; and finally, qualities of ansatzae construction, including the shallow layered ansatz which is comprised of rotation and entanglement operations [17], as well as implications of ansatz construction on the optimization routine of the cost function.

For running the algorithm with nonlinearities besides those which are discussed in [15], it is important to not only determine optimal circuit constructions that reduce noise in gate operations [14,21,31], but also different arrangement of entanglement gates in circuits. Peculiarly, nonlinearities of the Navier-Stokes equations exhibit terms in the cost function which must be computed on entirely different circuit constructions, leading to quantum circuits with readout values from expectations taken between operators denoted \hat{Q} , the discretized Nabla and Laplacian about each degree of freedom, and the pressure $\rho(t)$ exerted on the system. To this end, the circuits that will be displayed from terms of the Navier-Stokes cost function are of shallow depth, permitting for computations over quantum circuits for terms in the Navier-Stokes cost function to be numerically analyzed with Cirq simulations. Notably, the primary difficulties in applying the hybrid variational algorithm to Navier-Stokes is apparent through the QNPUs construction for expectation terms from the cost function presented below.

2 Algorithm

2.1 Overview

To quantify time evolution forwards at the initial state and after an increment, we introduce the states Ψ and $\tilde{\Psi}$. With some abuse of notation, to avoid confusion with the operator \hat{Q} in the cost function we denote the solutions to Navier-Stokes as f . As a result, the Navier-Stokes cost function is of the form,

$$\mathcal{C}(\lambda, \lambda_0) = |\lambda_0|^2 + \left(\frac{\tau}{h}\right)^2 |\tilde{\lambda}_0|^2 + \left(\frac{\tau}{\rho h}\right)^2 + 2 \operatorname{Re}\left\{-\frac{\tau}{h} \lambda_0^* \tilde{\lambda}_0 \langle\Psi|\hat{Q}|\tilde{\Psi}\rangle + \frac{\tau}{\rho h} \lambda_0 \langle\Psi|\nabla_x|p\rangle - \frac{1}{\rho} \left(\frac{\tau}{h}\right)^2 \tilde{\lambda}_0 \langle p|\nabla_x^\dagger \hat{Q}|\tilde{\Psi}\rangle\right\},$$

which is readily obtained upon collection of terms from the expansion of $\| |f(t+\tau)\rangle - \frac{\tau}{h} \hat{Q} |f(t)\rangle + \frac{\tau}{\rho h} \nabla_x |p(t)\rangle \|$ after rearrangement, in which we make use of the straightforward identities for discrete approximations of derivatives in the Navier-Stokes equations after finite differencing, which are,

$$\hat{Q} |f(t)\rangle = \langle f(t)|\hat{Q}^\dagger \quad \& \quad \nabla_x |p(t)\rangle = \langle p(t)|\nabla_x^\dagger ,$$

by virtue of the expectation being an Hermitian form. Next, the Euler method is applied to obtain \mathcal{C} for variational state preparation, in order to determine ground states in the optimization landscape. From the Navier-Stokes cost function, we identify variational states that are to be prepared when the algorithm from [15] is ran. Specifically, the operator \hat{Q} in \mathcal{C} emerges from finite differencing the Navier-Stokes equations and isolating for the time increment of the state of the solution f forwards in time by an increment τ , and takes the form, with $\mathbf{1}$ as the identity operator,

$$\hat{Q} \equiv \frac{h}{\tau} (\mathbf{1} - |f(t)\rangle \nabla_x - |v(t)\rangle \nabla_y + v \Delta_x + v \Delta_y) ,$$

where in \hat{Q} above,

$$\begin{aligned} \nabla_x &= A_x - \mathbf{1} , \quad \nabla_y = A_y - \mathbf{1} , \\ \Delta_x &= A_x^\dagger - 2 \times \mathbf{1} + A_x \text{ and, } \Delta_y = A_y^\dagger - 2 \times \mathbf{1} + A_y . \end{aligned}$$

We will make use of this procedure to study nonlinearities of the Euler and Poisson equations, in which quantum circuit architecture for computing expectation terms of the cost function above is executed for other PDEs with modifications to the QNPU and CP. After further discussion of the circuit outputs from the variational algorithm for Navier-Stokes, such modifications to the QNPU for the Euler and Poisson equations are valuable for analyzing computational bases with respect to nonlinear behaviors of inviscid flow, amongst other types of time evolution.

From the definition of \hat{Q} , we observe that the second and third expectations can be rewritten as,

$$\begin{aligned} \langle\Psi|\hat{Q}|\tilde{\Psi}\rangle &= \langle\Psi|\left(\frac{h}{\tau}(\mathbf{1} - |f(t)\rangle \nabla_x - |v(t)\rangle \nabla_y + v \Delta_x + v \Delta_y)\right)|\tilde{\Psi}\rangle \\ &= \langle\Psi|\frac{h}{\tau}|\tilde{\Psi}\rangle + \left(-\langle\Psi|\frac{h}{\tau}(|f(t)\rangle)\right)|\tilde{\Psi}\rangle + \left(-\langle\Psi|\frac{h}{\tau}(|v(t)\rangle)\right)|\tilde{\Psi}\rangle + \langle\Psi|\frac{h}{\tau}(v \Delta_x)\rangle|\tilde{\Psi}\rangle + \langle\Psi|\frac{h}{\tau}(v \Delta_y)\rangle|\tilde{\Psi}\rangle \\ &= \frac{h}{\tau} \left(\langle\Psi|\mathbf{1}|\tilde{\Psi}\rangle + \left(-\langle\Psi|(|f(t)\rangle)\right)|\tilde{\Psi}\rangle + \left(-\langle\Psi|(|v(t)\rangle)\right)|\tilde{\Psi}\rangle + \langle\Psi|v \Delta_x|\tilde{\Psi}\rangle + \langle\Psi|v \Delta_y|\tilde{\Psi}\rangle \right) , \end{aligned}$$

which amounts to computing the summation of expectations above, with the final resultant multiplied by $\frac{h}{\tau}$ corresponding to the second term. As for the third term, we can similarly expand by making use of the definition of \hat{Q} , obtaining

$$\begin{aligned}
\langle p | \nabla_x^\dagger \hat{Q} | \tilde{\Psi} \rangle &= \langle p | \nabla_x^\dagger \left(\frac{h}{\tau} (\mathbf{1} - |f(t)\rangle \nabla_x - |v(t)\rangle \nabla_y + v\Delta_x + v\Delta_y) \right) | \tilde{\Psi} \rangle \\
&= \langle p | \frac{h}{\tau} \left(\nabla_x^\dagger \right) | \tilde{\Psi} \rangle + \left(- \langle p | \frac{h}{\tau} \nabla_x^\dagger \left(|f(t)\rangle \right) \nabla_x | \tilde{\Psi} \rangle \right) + \left(- \langle p | \frac{h}{\tau} \nabla_x^\dagger \left(|v(t)\rangle \right) \nabla_y | \tilde{\Psi} \rangle \right) + \langle p | \frac{hv\Delta_x}{\tau} | \tilde{\Psi} \rangle \\
&\quad + \langle p | \frac{hv\Delta_y}{\tau} | \tilde{\Psi} \rangle \\
&= \frac{h}{\tau} \left(\langle p | \left(\nabla_x^\dagger \right) | \tilde{\Psi} \rangle + \left(- \langle p | \nabla_x^\dagger \left(|f(t)\rangle \right) \nabla_x | \tilde{\Psi} \rangle \right) + \left(- \langle p | \nabla_x^\dagger \left(|v(t)\rangle \right) \nabla_y | \tilde{\Psi} \rangle \right) + \langle p | v\Delta_x | \tilde{\Psi} \rangle \right. \\
&\quad \left. + \langle p | v\Delta_y | \tilde{\Psi} \rangle \right),
\end{aligned}$$

allowing for further rearrangements from respective collection of like terms in $|v(t)\rangle$, $|f(t)\rangle$, $v\Delta_x$ and $v\Delta_y$, between the second and third expectation terms, giving

$$\frac{h}{\tau} \left(- \langle p | \left(|v(t)\rangle + \nabla_x^\dagger |v(t)\rangle \nabla_x \right) | \tilde{\Psi} \rangle \right),$$

for $|v(t)\rangle$, while

$$\frac{h}{\tau} \left(- \langle p | \left(|f(t)\rangle + \nabla_x^\dagger |f(t)\rangle \nabla_x \right) | \tilde{\Psi} \rangle \right),$$

for $|f(t)\rangle$. Also, the remaining two terms dependent on v take the form,

$$\frac{2h}{\tau} \left(\langle p | v\Delta_x | \tilde{\Psi} \rangle + \langle \Psi | v\Delta_y | \tilde{\Psi} \rangle \right).$$

Hence applying linearity of expectation where appropriate in turn gives a cost function of the form, through the superposition

$$\begin{aligned}
|\lambda_0|^2 + \left(\frac{\tau}{h} |\tilde{\lambda}_0|^2 + \left(\frac{\tau}{\rho h} \right)^2 + \frac{2h}{\tau} \operatorname{Re} \{ \langle \Psi | \mathbf{1} | \tilde{\Psi} \rangle + \langle p | \left(\nabla_x^\dagger \right) | \tilde{\Psi} \rangle - \langle \Psi | \left(|v(t)\rangle \right) | \tilde{\Psi} \rangle + \langle p | \nabla_x^\dagger |v(t)\rangle \nabla_x | \tilde{\Psi} \rangle - \right. \\
\left. \langle p | \left(|f(t)\rangle + \nabla_x^\dagger |f(t)\rangle \nabla_x \right) | \tilde{\Psi} \rangle + 2 \left(\langle p | v\Delta_x | \tilde{\Psi} \rangle + \langle \Psi | v\Delta_y | \tilde{\Psi} \rangle \right) \right|,
\end{aligned}$$

which can be rearranged more explicitly, through substitution in terms with ∇_x , ∇_y , Δ_x and Δ_y , for the second term taken under Re ,

$$\langle p | \left(\nabla_x^\dagger \right) | \tilde{\Psi} \rangle = \langle p | \left(A_x^\dagger - \mathbf{1} \right) | \tilde{\Psi} \rangle,$$

and similarly for the third and fourth terms taken under Re ,

$$\langle \Psi | \left(|v(t)\rangle \right) | \tilde{\Psi} \rangle + \langle p | \nabla_x^\dagger |v(t)\rangle \nabla_x | \tilde{\Psi} \rangle = \langle \Psi | \left(|v(t)\rangle \right) | \tilde{\Psi} \rangle + \langle p | \left(\{A_x^\dagger - \mathbf{1}\} |v(t)\rangle \{A_x - \mathbf{1}\} \right) | \tilde{\Psi} \rangle.$$

For the fourth term taken under Re , we get

$$\langle p | \left(|f(t)\rangle + \nabla_x^\dagger |f(t)\rangle \nabla_x \right) |\tilde{\Psi}\rangle = \langle p | \left(|f(t)\rangle + \{A_x^\dagger - \mathbf{1}\} |f(t)\rangle \{A_x - \mathbf{1}\} \right) |\tilde{\Psi}\rangle ,$$

and finally from the fourth term multiplied by 2,

$$\langle p | v \Delta_x |\tilde{\Psi}\rangle + \langle \Psi | v \Delta_y |\tilde{\Psi}\rangle = \langle p | v \left(A_x^\dagger - 2 \times \mathbf{1} + A_x \right) |\tilde{\Psi}\rangle + \langle \Psi | v \left(A_y^\dagger - 2 \times \mathbf{1} + A_y \right) |\tilde{\Psi}\rangle ,$$

from which we collect all rearrangements, in turn obtaining a cost function of the form from like terms,

$$\begin{aligned} |\lambda_0|^2 + \left(\frac{\tau}{h} \right)^2 |\tilde{\lambda}_0|^2 + \left(\frac{\tau}{\rho h} \right)^2 + \frac{2h}{\tau} \operatorname{Re} \{ \langle \Psi | \mathbf{1} | \tilde{\Psi} \rangle + \langle p | \left(A_x^\dagger - \mathbf{1} \right) | \tilde{\Psi} \rangle + \langle \Psi | \left(|v(t)\rangle \right) | \tilde{\Psi} \rangle - \langle p | \left(\{A_x^\dagger - \mathbf{1}\} |v(t)\rangle \{A_x - \mathbf{1}\} \right) | \tilde{\Psi} \rangle - \langle p | \left(|f(t)\rangle + \{A_x^\dagger - \mathbf{1}\} |f(t)\rangle \{A_x - \mathbf{1}\} \right) | \tilde{\Psi} \rangle + 2 \left(\langle p | v \left(A_x^\dagger - 2 \times \mathbf{1} + A_x \right) | \tilde{\Psi} \rangle + \langle \Psi | v \left(A_y^\dagger - 2 \times \mathbf{1} + A_y \right) | \tilde{\Psi} \rangle \right) \} , \end{aligned}$$

from which rearranging fifth expectation term under Re gives, by making use of the identity $|f(t)\rangle = \lambda_0 |\Psi\rangle$, which is related to the time evolved quantum state which satisfies $|f(t+\tau)\rangle = \tilde{\lambda}_0 |\tilde{\Psi}\rangle$ for variational states,

$$\begin{aligned} \langle p | \left(\{\tilde{\lambda}_0 | \tilde{\Psi} \rangle\} + \{A_x^\dagger - \mathbf{1}\} \{\tilde{\lambda}_0 | \tilde{\Psi} \rangle\} \{A_x - \mathbf{1}\} \right) | \tilde{\Psi} \rangle &= \left(\langle p | \{\tilde{\lambda}_0 | \tilde{\Psi} \rangle\} + \langle p | \{A_x^\dagger - \mathbf{1}\} \{\tilde{\lambda}_0 | \tilde{\Psi} \rangle\} (A_x - \mathbf{1}) \right) | \tilde{\Psi} \rangle , \\ &= \langle p | \{\tilde{\lambda}_0 | \tilde{\Psi} \rangle\} | \tilde{\Psi} \rangle + \langle p | \{A_x^\dagger - \mathbf{1}\} \{\tilde{\lambda}_0 | \tilde{\Psi} \rangle\} (A_x - \mathbf{1}) | \tilde{\Psi} \rangle , \end{aligned}$$

which yields the desired cost function for Navier-Stokes below after substituting in for variational states for the solution to the Navier-Stokes equations, yielding,

$$\begin{aligned} \boxed{\mathcal{C}^x(\lambda, \lambda_0)} &= |\lambda_0|^2 + \left(\frac{\tau}{h} \right)^2 |\tilde{\lambda}_0|^2 + \left(\frac{\tau}{\rho h} \right)^2 + \frac{2h}{\tau} \operatorname{Re} \{ \langle \Psi | \mathbf{1} | \tilde{\Psi} \rangle + \langle \textcolor{brown}{p} | \left(A_x^\dagger - \mathbf{1} \right) | \tilde{\Psi} \rangle + \langle \Psi | \left(|v(t)\rangle \right) | \tilde{\Psi} \rangle - \langle \textcolor{brown}{p} | \left(\{A_x^\dagger - \mathbf{1}\} |v(t)\rangle \{A_x - \mathbf{1}\} \right) | \tilde{\Psi} \rangle - \langle \textcolor{brown}{p} | \{\tilde{\lambda}_0 | \tilde{\Psi} \rangle\} | \tilde{\Psi} \rangle - \langle \textcolor{brown}{p} | \{A_x^\dagger - \mathbf{1}\} \{\tilde{\lambda}_0 | \tilde{\Psi} \rangle\} (A_x - \mathbf{1}) | \tilde{\Psi} \rangle + 2 \left(\langle \textcolor{brown}{p} | v \left(A_x^\dagger - 2 \times \mathbf{1} + A_x \right) | \tilde{\Psi} \rangle + \langle \Psi | v \left(A_y^\dagger - 2 \times \mathbf{1} + A_y \right) | \tilde{\Psi} \rangle \right) \} , \quad (\star) \end{aligned}$$

for the x component of the solution.

As one modification to the Lubasch et al variational algorithm, another cost function must be introduced within the QNPU which has expectation terms dependent on the other component of the solution which appears in the Navier-Stokes equations. We denote this additional cost function as $\mathcal{C}^y(\lambda, \lambda_0)$. The circuit diagram provided in *Figure 2* illustrates the expectation terms from this cost function for only one component of the solution. Due to the no-cloning theorem, to accommodate expectation terms associated with the remaining cost function \mathcal{C}^y for the remaining component of the solution, we must prepare additional states outside of those illustrated in the ancillary registers of *Figure 1*.

Within \mathcal{C} , it is necessary that we introduce cost functions for $|v(t)\rangle$ so that corresponding quantum states to each quantity can be stored appropriately on registers in the quantum computer. To do this, we follow similar procedures used to obtain the first Navier-Stokes cost function, as we formulate cost functions which correspond to different classes of pressure distributions.¹

To this end, we introduce several cases to further study the computations associated with different pressure dependent expectation terms from the Navier-Stokes cost function. If the pressure distribution is uniform, in the simplest case each

¹Further remarks will also shed light upon determining ground states for the Navier-Stokes cost function in a constant pressure distribution which remains constant with time steps in the evolution.

pressure dependent term amounts to the expectation with a quantity that is uniformly distributed over the domain. In more realistic cases, the variational state $|p(t + \tau)\rangle$ after $|p(t)\rangle$ is time evolved forwards requires specification of additional variational parameters λ^p , in addition to an accompanying unitary operator as the time evolution is computed. We introduce classes of admissible pressure distributions for the Navier-Stokes equations in the following cases. The expectation terms from \mathcal{C}^x and \mathcal{C}^y which will be impacted are indicated in orange. In the cases below, we discuss how the pressure distribution would be prepared and computed on the quantum computer for one coordinate, from which computations for the remaining component easily follow.

We make use of previous rearrangements after substituting in \hat{Q} and prepare corresponding variational states of the pressure distribution p after time evolution, which are readily obtained from \star . From previous studies of exact solutions to Navier-Stokes [32], pressure distributions corresponding to solutions in the plane focus on analyses of convective terms under which solutions are known to exist. Below, we gather results by reading off expectation terms from the Navier-Stokes cost function which are dependent on the pressure, and afterwards identifying admissible pressure distributions from solutions to the equations presented in the literature, in addition to additional formulations of the cost function.

2.1.1 Vanishing pressure distribution

Under a pressure distribution with no magnitude at every point on the domain over which readout for Navier-Stokes is produced, the cost function simplifies to the following. We simply cross off terms if one term in the expectation vanishes, in which

$$\boxed{\mathcal{C}^{0,x}(\lambda, \lambda_0)} = |\lambda_0|^2 + \left(\frac{\tau}{h}\right)^2 |\tilde{\lambda}_0|^2 + \left(\frac{\tau}{\rho h}\right)^2 + \frac{2h}{\tau} \operatorname{Re} \{ \langle \Psi | \mathbf{1} | \tilde{\Psi} \rangle + \langle \Psi | \left(|v(t)\rangle \right) \tilde{\Psi} \} - 2 \left(\langle \Psi | v \left(A_y^\dagger - 2 \times \mathbf{1} + A_y \right) | \tilde{\Psi} \rangle \right) ,$$

for the cost function of the x component of the solution under no pressure distribution.

In the remaining cases, the following cost functions differ in pressure dependent expectation terms from \star in orange.

2.1.2 Uniform pressure distribution

For a uniform distribution \mathcal{U} the time evolution of the pressure for any time step remains unchanged. Simply, the most nontrivial cost function for the magnitude of the pressure over each grid point of the discretization yields the following, when $p \equiv c$ with $c > 0$,

$$\boxed{\mathcal{C}^{\mathcal{U},x}(\lambda, \lambda_0)} = |\lambda_0|^2 + \left(\frac{\tau}{h}\right)^2 |\tilde{\lambda}_0|^2 + \left(\frac{\tau}{\rho h}\right)^2 + \frac{2h}{\tau} \operatorname{Re} \{ \langle \Psi | \mathbf{1} | \tilde{\Psi} \rangle + \langle \textcolor{orange}{c} | \left(A_x^\dagger - \mathbf{1} \right) | \tilde{\Psi} \rangle + \langle \Psi | \left(|v(t)\rangle \right) \tilde{\Psi} \} - \langle \textcolor{orange}{c} | \left(\{ A_x^\dagger - \mathbf{1} \} |v(t)\rangle \{ A_x - \mathbf{1} \} \right) | \tilde{\Psi} \rangle - \langle \textcolor{orange}{c} | \{ \tilde{\lambda}_0 | \tilde{\Psi} \rangle | \tilde{\Psi} \rangle - \langle \textcolor{orange}{c} | \{ A_x^\dagger - \mathbf{1} \} \{ \tilde{\lambda}_0 | \tilde{\Psi} \rangle \} (A_x - \mathbf{1}) | \tilde{\Psi} \rangle + 2 \left(\langle \textcolor{orange}{c} | v \left(A_x^\dagger - 2 \times \mathbf{1} + A_x \right) | \tilde{\Psi} \rangle + \langle \Psi | v \left(A_y^\dagger - 2 \times \mathbf{1} + A_y \right) | \tilde{\Psi} \rangle \right) \} ,$$

through modifications to the expectation terms from \mathcal{C} which are dependent on p , in orange. In comparison with the most simple pressure distribution assumption in the previous case, $\mathcal{C}^{\mathcal{U},x}$ retains all pressure dependent expectation terms.

2.1.3 Linearly dependent \mathcal{L} pressure distribution

With respect to the location in the optimization landscape

In relevant expectation terms, a pressure distribution which varies linearly with respect to space yields the following superposition, including pressure dependent expectation terms,

$$\boxed{\mathcal{C}^{\mathcal{L},x}(\lambda, \lambda_0)} = |\lambda_0|^2 + \left(\frac{\tau}{h}\right)^2 |\tilde{\lambda}_0|^2 + \left(\frac{\tau}{\rho h}\right)^2 + \frac{2}{\tau} \frac{h}{\tau} \operatorname{Re} \{ \langle \Psi | \mathbf{1} | \tilde{\Psi} \rangle + \langle \mathcal{L} | \left(A_x^\dagger - \mathbf{1}\right) | \tilde{\Psi} \rangle + \langle \Psi | \left(|v(t)\rangle\right) | \tilde{\Psi} \rangle - \langle \mathcal{L} | \left(\{A_x^\dagger - \mathbf{1}\} |v(t)\rangle \{A_x - \mathbf{1}\}\right) | \tilde{\Psi} \rangle - \langle \mathcal{L} | \{\tilde{\lambda}_0 | \tilde{\Psi} \rangle | \tilde{\Psi} \rangle - \langle \mathcal{L} | \{A_x^\dagger - \mathbf{1}\} \{\tilde{\lambda}_0 | \tilde{\Psi} \rangle\} (A_x - \mathbf{1}) | \tilde{\Psi} \rangle + 2 \left(\langle \mathcal{L} | v \left(A_x^\dagger - 2 \times \mathbf{1} + A_x\right) | \tilde{\Psi} \rangle + \langle \Psi | v \left(A_y^\dagger - 2 \times \mathbf{1} + A_y\right) | \tilde{\Psi} \rangle \right) \} ,$$

which results in the following modification to the circuit architecture discussed in the next section, and displayed in *Figure 1 & Figure 2*. Specifically, if the pressure distribution is proportional to the absolute value of the coordinate of space at which the sample is drawn, then additional ancillary registers in the circuit must be prepared so as to keep track of the location at which the sample is gathered rather than its magnitude alone. Such a class of distributions is realistic for further complexity upon the distribution assumption in the previous two cases. Performing simple manipulations under this assumption gives, respectively for the second, fourth, fifth, sixth, and seventh terms under Re ,

$$\boxed{2} \Rightarrow \langle \mathcal{L} | \left(A_x^\dagger - \mathbf{1}\right) | \tilde{\Psi} \rangle = \left(\langle \mathcal{L} | \left(A_x^\dagger - \mathbf{1}\right) \right) | \tilde{\Psi} \rangle = \left(\langle \mathcal{L} | A_x^\dagger - \langle \mathcal{L} | \mathbf{1} \rangle \right) | \tilde{\Psi} \rangle = \langle \mathcal{L} | A_x^\dagger | \tilde{\Psi} \rangle - \langle \mathcal{L} | \mathbf{1} | \tilde{\Psi} \rangle ,$$

$$\boxed{4} \Rightarrow \langle \mathcal{L} | \left(\{A_x^\dagger - \mathbf{1}\} |v(t)\rangle \{A_x - \mathbf{1}\}\right) | \tilde{\Psi} \rangle = \left(\langle \mathcal{L} | \left(\{A_x^\dagger - \mathbf{1}\} |v(t)\rangle \{A_x - \mathbf{1}\}\right) \right) | \tilde{\Psi} \rangle = \langle \mathcal{L} | \left(\{A_x^\dagger - \mathbf{1}\} |v(t)\rangle \{A_x - \mathbf{1}\}\right) | \tilde{\Psi} \rangle = \left(\left(\langle \mathcal{L} | \{A_x^\dagger - \mathbf{1}\} |v(t)\rangle \right) \{A_x - \mathbf{1}\} \right) | \tilde{\Psi} \rangle ,$$

$$\boxed{5} \Rightarrow \langle \mathcal{L} | \{\tilde{\lambda}_0 | \tilde{\Psi} \rangle\} | \tilde{\Psi} \rangle = \left(\langle \mathcal{L} | \{\tilde{\lambda}_0 | \tilde{\Psi} \rangle\} \right) | \tilde{\Psi} \rangle = \left(\langle \mathcal{L} | \tilde{\lambda}_0 | \tilde{\Psi} \rangle \right) | \tilde{\Psi} \rangle$$

$$\boxed{6} \Rightarrow \langle \mathcal{L} | \{A_x^\dagger - \mathbf{1}\} \{\tilde{\lambda}_0 | \tilde{\Psi} \rangle\} (A_x - \mathbf{1}) | \tilde{\Psi} \rangle = \langle \mathcal{L} | \left(\{A_x^\dagger - \mathbf{1}\} \{\tilde{\lambda}_0 | \tilde{\Psi} \rangle\} (A_x - \mathbf{1})\right) | \tilde{\Psi} \rangle = \left(\langle \mathcal{L} | \left(A_x^\dagger \tilde{\lambda}_0 - \tilde{\lambda}_0\right) | \tilde{\Psi} \rangle (A_x - \mathbf{1}) \right) | \tilde{\Psi} \rangle = \left(\left(\langle \mathcal{L} | \left(A_x^\dagger \tilde{\lambda}_0 - \tilde{\lambda}_0\right) \right) | \tilde{\Psi} \rangle \right) (A_x - \mathbf{1}) | \tilde{\Psi} \rangle ,$$

$$\boxed{7} \Rightarrow \langle \mathcal{L} | v \left(A_x^\dagger - 2 \times \mathbf{1} + A_x\right) | \tilde{\Psi} \rangle = \langle \mathcal{L} | \left(v A_x^\dagger - 2 \times v + v A_x\right) | \tilde{\Psi} \rangle = \langle \mathcal{L} | v A_x^\dagger | \tilde{\Psi} \rangle - \langle \mathcal{L} | \{2 \times v\} | \tilde{\Psi} \rangle + \langle \mathcal{L} | v A_x | \tilde{\Psi} \rangle = \langle \mathcal{L} | v A_x^\dagger | \tilde{\Psi} \rangle - 2 \langle \mathcal{L} | v | \tilde{\Psi} \rangle + \langle \mathcal{L} | v A_x | \tilde{\Psi} \rangle .$$

Finally, collecting all terms in $\mathcal{C}^{\mathcal{L},x}$ in light of such rearrangements gives,

$$\boxed{\mathcal{C}^{\mathcal{L},x}(\lambda, \lambda_0)} = |\lambda_0|^2 + \left(\frac{\tau}{h}\right)^2 |\tilde{\lambda}_0|^2 + \left(\frac{\tau}{\rho h}\right)^2 + \frac{2}{\tau} \frac{h}{\tau} \operatorname{Re} \{ \langle \Psi | \mathbf{1} | \tilde{\Psi} \rangle + \overbrace{\langle \mathcal{L} | A_x^\dagger | \tilde{\Psi} \rangle - \langle \mathcal{L} | \mathbf{1} | \tilde{\Psi} \rangle}^{\boxed{2}} + \overbrace{\langle \Psi | \left(|v(t)\rangle\right) | \tilde{\Psi} \rangle - \overbrace{\left(\left(\langle \mathcal{L} | \{A_x^\dagger - \mathbf{1}\} |v(t)\rangle \right) \{A_x - \mathbf{1}\} \right) | \tilde{\Psi} \rangle}^{\boxed{4}} - \overbrace{\left(\langle \mathcal{L} | \tilde{\lambda}_0 | \tilde{\Psi} \rangle \right) | \tilde{\Psi} \rangle}^{\boxed{5}} - \overbrace{\left(\left\{ \langle \mathcal{L} | \left(A_x^\dagger \tilde{\lambda}_0 - \tilde{\lambda}_0\right) \right\} | \tilde{\Psi} \rangle \right) (A_x - \mathbf{1}) | \tilde{\Psi} \rangle}^{\boxed{6}} + \overbrace{2 \left(\langle \mathcal{L} | v A_x^\dagger | \tilde{\Psi} \rangle - 2 \langle \mathcal{L} | v | \tilde{\Psi} \rangle + \langle \mathcal{L} | v A_x | \tilde{\Psi} \rangle \right) + \langle \Psi | v \left(A_y^\dagger - 2 \times \mathbf{1} + A_y\right) | \tilde{\Psi} \rangle}^{\boxed{7}}} +$$

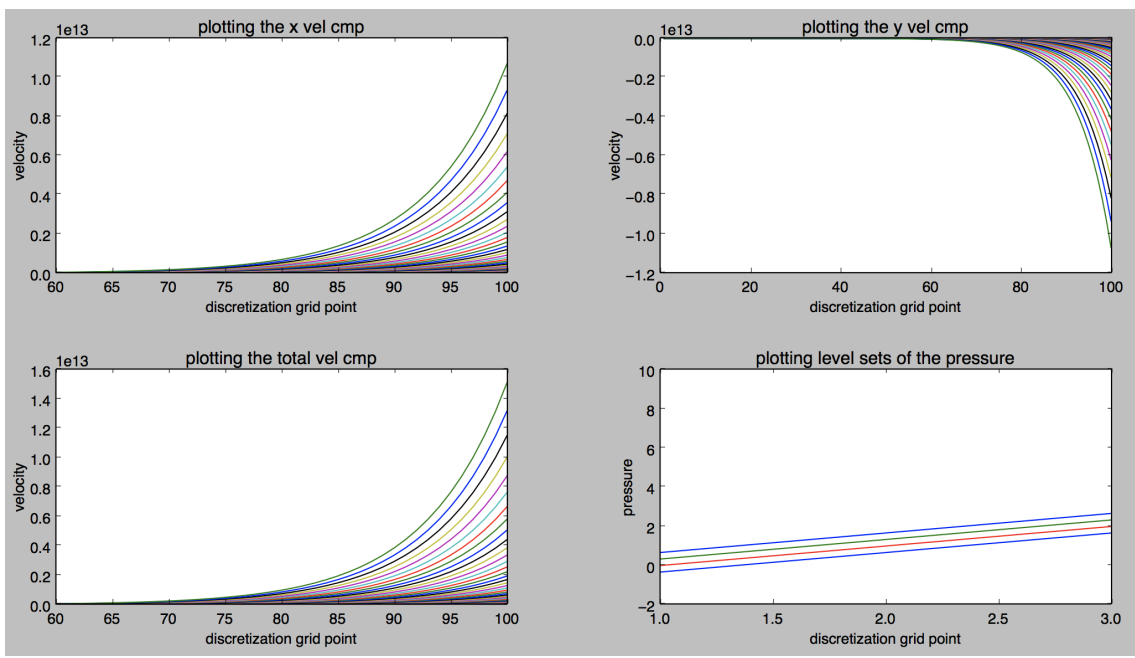


Figure 1: For exact solutions to Navier-Stokes, the x component of the velocity satisfies $v_x = A \exp\left(c/\{\nu(\alpha^2 + \beta^2)\}(\alpha x + \beta y)\right) + B$, while the y component of the velocity satisfies $v_y = 1/\beta\left(c - \alpha B - \alpha A \exp\left(c/\{\nu(\alpha^2 + \beta^2)\}(\alpha x + \beta y)\right)\right)$ where $\alpha, \beta \in \mathbf{R}$. For α and β of agreeing sign, namely both quantities taken to be positive or negative, the individual components of the velocity, in addition to the total component of the velocity of the solution, are illustrated. A free parameter choice which strongly favors α or β , or vice versa, results in components of the solution exhibiting variable rates of exponential growth or decay in the velocity as the grid point of the discretization varies.

2.2 Earlier studies of solutions to Navier-Stokes in the plane

Previous works have investigated several different aspects of the Navier-Stokes equations, whether it be the domain over which solutions are obtained, specific assumptions of the behavior of the pressure gradient under translations and rotations and over discretizations of varying composition [17]. In higher dimensional cases beyond the plane, past works have studied the regularity structure of solutions to the partial differential equation, as well as providing solutions for the equations driven by space time white noise through arguments relating to the construction of Gaussian invariant measures and fixed point mappings [28,29].

On the other hand, efforts have also been made to prove analytical solutions for example pressure distributions to the equations as given in [18]. By comparison with analytical solutions under assumptions on choice of parameters, comparisons between the cost function and exact solutions to the equations can be determined. Next, to observe conservation laws of the system for other quantities, whether it be helicity, 2D entropy or total vorticity of the trajectory, Charnyi, Heister, Olshanskii and Rebholz in [5] introduce numerical methods for simulating the pressure across three dimensional objects including a square cylinder.

With observations stemming from Riemannian geometry and connections to the behavior of the Ricci curvature and trajectory of Brownian motion, Arnaudon and Cruziero [3] make statements of the variational principle allowing for arguments involving the covariant derivative in which symmetry of the Ricci curvature tensor through a damped Laplacian is formalized. Relatedly, Cresson and Darses [7] provide formulations of the Navier-Stokes and Stokes equations for incompressible fluid flow, while Apte, Auroux and Ramaswamy [2] avoid finite differencing the equations to obtain solutions that are finite in time, but with unknown pressure as initial conditions, directly opposite to the procedure in [18]. Figure 1 shows plots of solutions to Navier-Stokes for the x and y components of the velocity solution.

2.3 Organization

We present results from quantum circuits to compute all required expectation values of the cost function. Then, within the framework of the variational algorithm, we present behaviors of expectation terms of the cost function, to discuss overall performance of the variational algorithm.

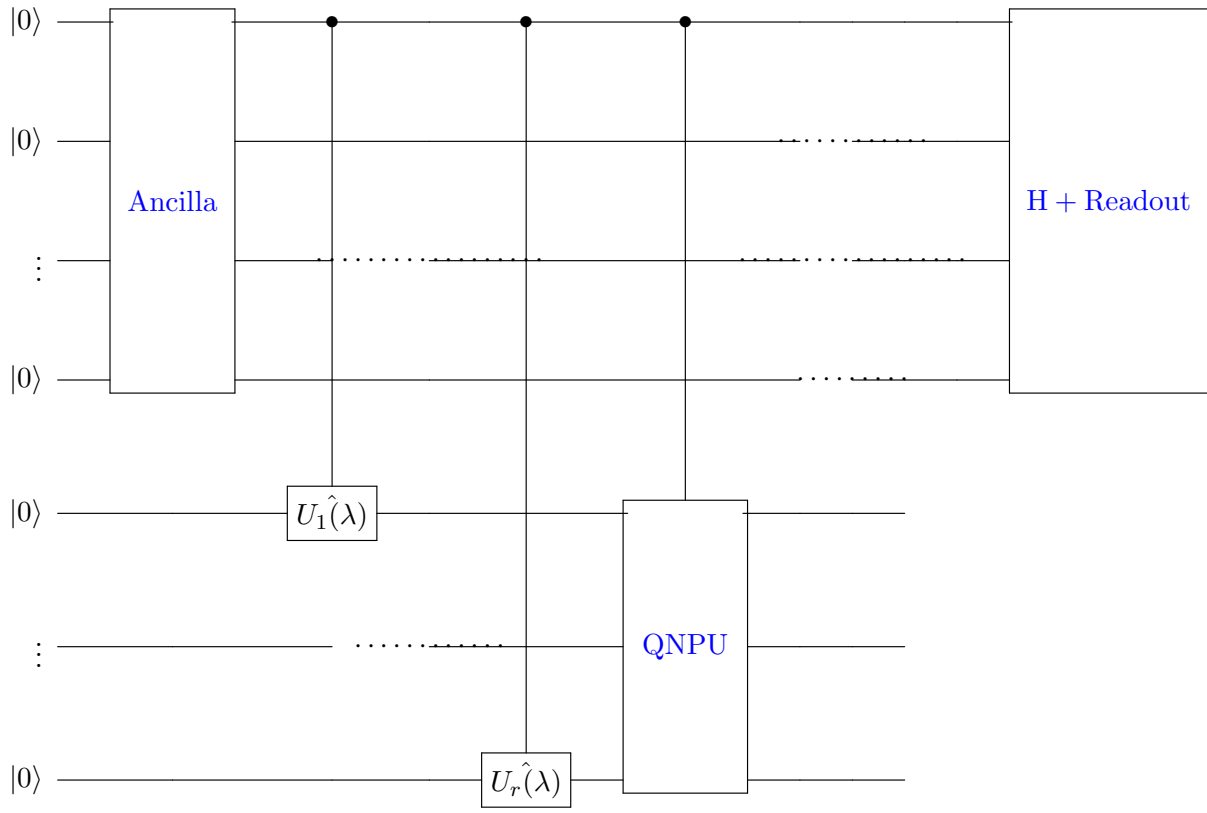


Figure 2: *Quantum circuit diagram for the Navier-Stokes variational algorithm.* With sufficient ancilla registers for carry bits associated with computation of expectation values in \mathcal{C} and each prefactor, the topmost ancilla bits initialized to the 0 states undergo Hadamard gates in the Ancilla block for their first operation before being time evolved and entering the QNPU, in addition to passing through additional Hadamard operations before each read out. From previous specifications on circuit architecture, we include $n = 4$ qubits to account for the time evolution in each direction of freedom. The ancilla bits are significant for storing intermediate computations of \mathcal{C} , which as shown in *Figure 2*, consists of scalar addition and multiplication of quantities dependent on the Reynolds number ρ . The interaction between the control and target qubits after being fed into the QNPU is shown below in *Figure 2*. Additional terms that must be processed within the QNPU are separated based on the quantum state that must be prepared in the computed past the 0 state initialization, including the cost functions introduced in *Section 2.1*. After each ancilla is time evolved forwards, upon entry to the QNPU (below in *Figure 3*) further quantum computation is performed; for our considerations in the circuit diagram above a potential number of time evolution gates is included, but measurements in each time steps for solutions in the plane include computations of each component of the velocity, in addition to the pressure distribution at each grid point. Upon observation, the wave function for each control qubit collapses.

2.4 Acknowledgments

The author would like to thank Professor McMahon for suggesting a direction for the project. Also, many thanks to fellow team members in the McMahon Lab variational PDE subgroup, including Thomas, Leeseok, Rithesh, Yilian, Natalia & Matthew, as well as several others, for simulating discussions and thoughts.

3 Quantum circuits

3.1 Expectation computations from the cost function

Construction of the elementary circuits below demonstrates the sequence of gate operations from which the quantum-classical computational loop is executed. From foundational representations of quantum networks as a sequence of reversible unitary transformations [25], we achieve efficient computations executable through adaptations of the variational algorithm of [15] with hardware efficient algorithm which could be further test in future work for implementation on circuits with more qubits. From terms that are included in the cost function, we introduce circuits for successful quantum computation through enforcement of the number of qubits on which the algorithm will be ran, in addition to peculiar characteristics of nonlinearities of the Navier Stokes equations. In particular, the requisite circuits for the cost function revolve about quantifying the time evolution of Brownian particles under forces which respect conservation of momentum. For quantum circuit representations of expectations in the cost function, the discrete derivative operators about each planar degree of freedom require that we include circuit representations for the plain adder to process quantum computations involving the

time evolution of fluid governed by the equations.

As in [15], the subcircuits listed below will be situated within the QNPU which is necessary for the cost function minimization. To account for complexity posed by the Navier-Stokes cost function, in addition to several other computational problems, ranging from those associated with vanishing gradients of the cost function to ansatz construction [11], expressibility of parametrizations for quantum circuits [23], qubit quality, noise and complexity growth [4,10], different forms of ansatzae for the equations will be studied and qualitatively compared. In particular, for the cost function given on the previous page, we identify all 8 relevant terms and provide the circuit representations. To systematically characterize the coverage of the Hilbert space that we expect from circuit simulations, we identify each of the cross terms from the expansion of the square of the norm of the cost function that is obtained from Euler's method. With suitable circuit representations and tracing of the output, we describe more general architecture of the quantum circuits besides the adder, with implications for complexity of the algorithm and exploration of the optimization landscape.

3.2 Architecture

Before executing gates of the QNPU, to trace output of control qubits in the circuit we illustrate the number of initialized $|0\rangle$ states required for the execution of the variational algorithm from [15]. For nonlinearities of the Navier-Stokes equations, executing nonlinearities raised by the cost function for the QNPU alone requires that we include additional qubits so that the three expectation values from the cost function can be added together. Moreover, we must appropriately situate the input ports into the QNPU from previous gate operations in the circuit following the $|0\rangle$ state initialization.

To execute all relevant gate operations, we perform circuit simulations on $n = \text{target qubits}$. We enforce this number of target qubits in the implementation because it is not only representative of degrees of freedom in the plane for which closed forms have been obtained, but also because it allows for specifications of ancilla bits that must be controlled while performing adder operations upon entry into the QNPU. More specifically, for the first target qubit initialized to $|0\rangle$, after applying the Hadamard gate and time evolving the quantum state forwards, the Navier-Stokes QNPU processes target qubits following these previous gate operations with an adder to compute the shift of all terms in the cost function. To accommodate the circuit construction so that all gates reflect the capability of the algorithm to be applied to other nonlinear equations, we incorporate standard variational parameters λ over which the cost function will be minimized. Throughout the minimization procedure, we incorporate an adder circuit to determine the summation of all terms of the cost function, requiring that we have sufficient ancilla bits for outstanding operations on the quantum computer. Specifically, the operations associated with $C(\lambda)$ include scalar multiplication computations of the variational parameter λ_0 with itself, the variational parameter $\tilde{\lambda}_0$ with $(\frac{\tau}{h})^2$, and $(\frac{\tau}{\rho h})^2$. Besides these terms, additional computations must be dealt with by isolating all accompanying prefactors to each expectation value, including $-\frac{\tau}{h}\lambda_0^*\tilde{\lambda}_0$, $\frac{\tau}{\rho h}\lambda_0^*$, and $-\frac{1}{\rho}(\frac{\tau}{h})^2\tilde{\lambda}_0$, respectively. Finally, additional carry bits must be included in the control port (CP) to the QNPU so that carry bits can be established for adding the three expectation values together before the real part of the resultant is taken. In the following circuit diagram beginning with *Figure 1*, we establish all such specifications on the ancilla within the computational basis. Furthermore, the appropriate multiplication of each prefactor must correspond to a suitable number of ancilla in the CP which must be specified before the time evolution is initiated.

Specifically, in the quantum circuits for the Navier-Stokes equations, we demand that the control port contain two ancilla for operations associated with adding expectation values together. In particular, besides the topmost control qubits which undergo Hadamard gates before entering the QNPU, additional ancilla must be provided for multiplication with each prefactor previously mentioned. With the quantum Fourier Transform (QFT), quantum network representations for dividing scalars can be achieved by loading the divisor and dividend into quantum registers. This scheme is applicable to computations involving each expectation term, which after being computed individually, and multiplied by each corresponding prefactor, has a resultant term from the three values. Because the order in which the expectations are added is irrelevant, for simplicity we group together the first and third expectation values from $C(\lambda, \lambda_0)$ which have the same time, to then determine contributions before taking the real part of the superposition of expectations. The circuit in *Figure 1* illustrates the circuit arrangement over which computations will be executed. The ancilla block on the topmost layer of an arbitrary number of control qubits each undergo Hadamard operations, while the topmost control qubit is responsible for time evolving each of the target qubits represented in the circuit diagram below the [Ancilla](#) block.

The remaining boxes in the circuit are responsible for the following operations. The [QNPU](#) treats nonlinearities of the Navier-Stokes equations from expectation terms in \mathcal{C} , while the [H + Readout](#) block applies the Hadamard gate to each ancilla after the QNPU and reads out each value after an application of $\hat{\sigma}_z$. Furthermore, it is important to quantify the number of control qubits associated with addition or multiplication on the quantum computer from the prefactors that have been previously identified. In light of rearrangements of \mathcal{C} in *Section 2.1*, we present a synopsis below of the number of ancilla required in the topmost registers of the circuit from *Figure 1*; specifically, factoring out the constant from the superposition of expectation terms from the real term of \mathcal{C} in \star before further rearrangements for the cost functions for $|f(t)\rangle$ and $|p(t)\rangle$, outside of the multiplication of scalar terms, permits for one operation of multiplication after the summation of all expectation terms has been computed, to be followed by division by τ . Quantum circuit representations of integer division in [30] are achieved through dedication of ancilla to the divisor and dividends of integers in an expression,

ultimately relying on the QFT for quantum integer division. The "Clifford + T" gate family is applied to individually load divisors, dividends and remainders into the quantum circuit for computation, and in our case can simply be applied to the cost function with dividend and divisor; in the case of the Navier-Stokes cost function, the dividend itself must be loaded in as a scalar product. Outside of the QNPU, results of quantum computation for the cost function are terminated as the final read outs for the ancilla are executed from the **H + Readout** block.

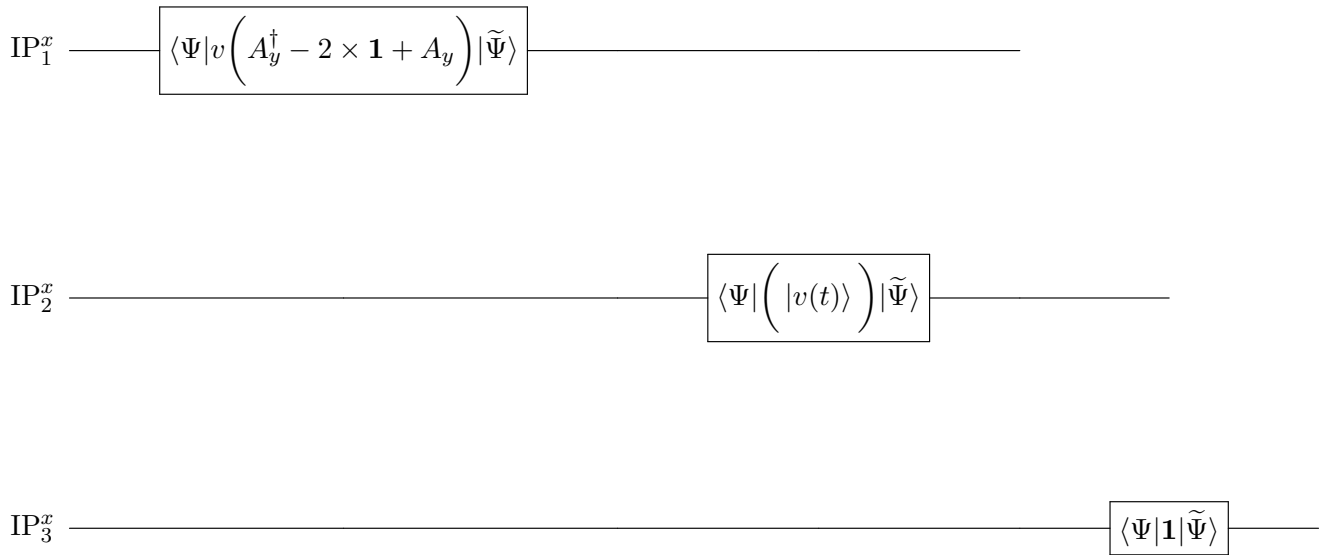


Figure 3: *QNPU circuit diagram, expectation terms from the Navier-Stokes cost function which are independent of the pressure distribution p.* Qubits in each input port to the QNPU are shown after time evolution. The ancilla bits from *Figure 1* demonstrate the portion of the circuit architecture which requires that intermediate results be stored in the quantum computer, either due to addition or scalar multiplication operations. Under the assumption of a vanishing pressure distribution discussed in *2.1.1*, expectation terms within the QNPU can be distributed as follows within the proposed Navier-Stokes circuit architecture. First, we arrange the quantum registers in the QNPU on the basis of the most significant qubits being stored in the uppermost registers of the circuit, which include the expectation terms $\langle \Psi | v \left(A_y^\dagger - 2 \times \mathbf{1} + A_y \right) | \tilde{\Psi} \rangle$,

$\langle \Psi | (|v(t)\rangle) | \tilde{\Psi} \rangle$ and $\langle \Psi | \mathbf{1} | \tilde{\Psi} \rangle$. Second, we arrange each qubit for computation as shown above, in which the expectation term in the topmost qubit is computed by forming the quantum state resulting from the time evolution of qubits initialized to the $|0\rangle$ state below the ancilla qubits in *Figure 1*. The remaining two qubits below are computed by preparing the variational states of $|v(t)\rangle$, and computing the expectation value under the identity state $\mathbf{1}$, respectively. The portion of the QNPU architecture displayed in *Figure 4* illustrates how the first three constant terms which appear in all cost functions \mathcal{C} are computed, and the states that are produced in the three registers above corresponding to pressure independent expectation terms in $\mathcal{C}^{0,x}$ after surpassing the prescribed gates are output from the QNPU, illustrated in the quantum registers below those of the ancilla qubits in *Figure 1*.

We collect all expectation values from terms given in the previous section. Within the broader context of the algorithm, we initially prepare all qubits in the $|0\rangle$ state and furthermore, examine the $\hat{U}_j(\lambda)$ gates, where j runs over the number of qubits. A subset of the expectation terms from the Navier-Stokes cost function are represented in the QNPU for one component of the solution in *Figure 3*, from which further discussion is devoted towards circuit architecture for computations involving both components of the solution.

3.3 Classical sampling

One direction of future interest for optimization the cost function when obtaining readout from the variational algorithm for Navier-Stokes centers about making use of Brownian bridge sampling, as an indication of whether the optimization procedure has encountered a plateau in the energy landscape.

By contrasting the distribution of the random samples within a fixed box B , and outside of the same box, we establish immediate connections between the short and long range interactions of the system. Through the construction of couplings \mathcal{J}_{ij} for a Hamiltonian \mathcal{H} , the time evolution of turbulent flow is modeled under \mathcal{H} by:

- forming a sample array of the bridge values that are randomly assumed within a fixed $B_{x_i}^\epsilon$,
- determining the displacement of the bridge sampling at each neighboring point in the array by forming the pointwise difference between neighboring elements of the array,

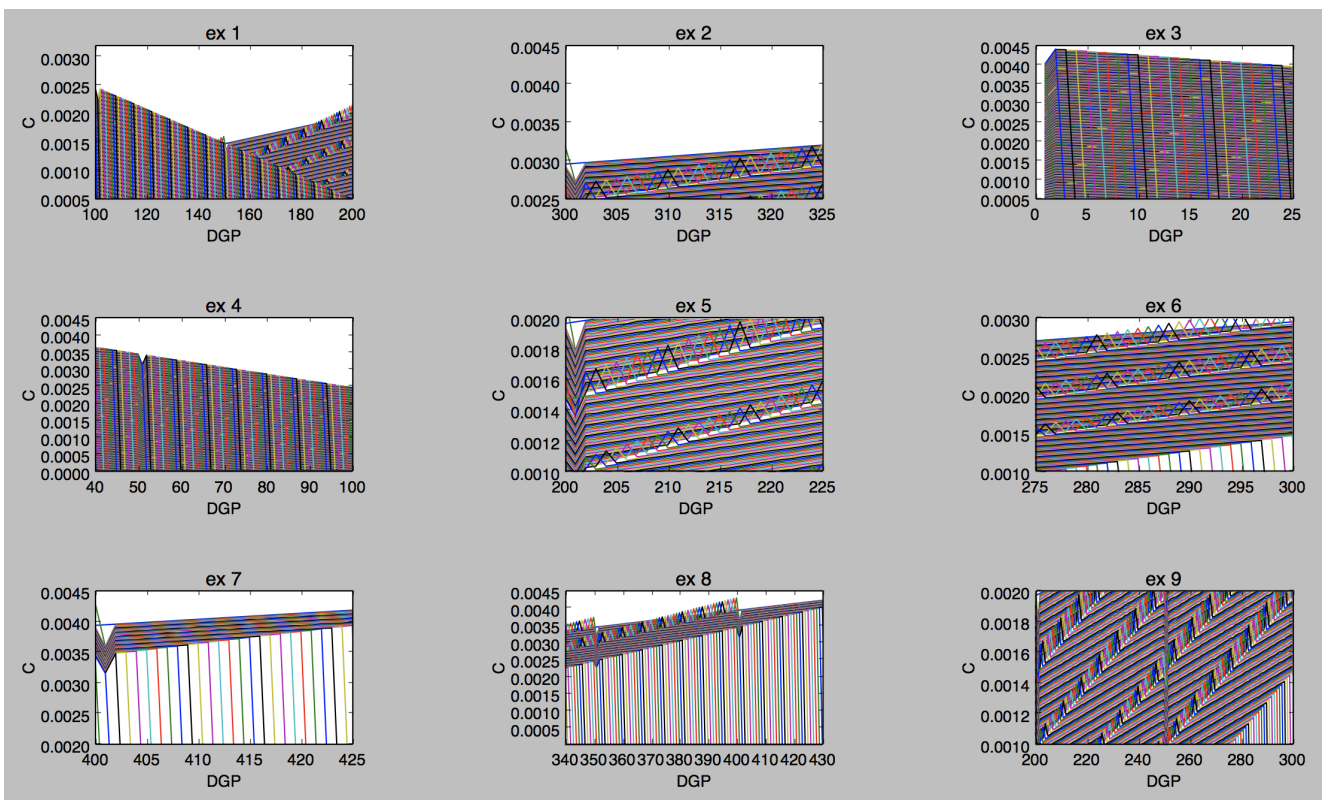


Figure 4: Each entry in the plot above demonstrates more of the self similar, fine grained behavior in the long range couplings plot. In the *first* subplot, a portion of the long range couplings surface exhibits a collection of couplings for which the bridge samples are inversely proportional to the grid point that is sampled, as the number of points increases. DGP indicates the discretization grid point at which a sample is collected. In the second plot, another portion of the surface exhibits the couplings at which different curves, whether colored *yellow* or *blue*, reach a fixed maximum coupling constant which is dependent on the nature of the underlying sampling distribution. In the third plot, another perspective of the decay of the long range couplings is shown, in the *yellow* line which intersects the axis around the fifth discretization point sharply decays in the magnitude of its coupling as the same process proceeds to draw the fifth random variable. In the fourth plot, a similar pattern at the number of discretization point at which the *yellow*, and any other colored lines approach 0 is observed. In the fifth and sixth plots, zoom ins of the peaks of each long range coupling constant sequence from the second plot is given. In the *seventh* plot, the long range couplings numerically decrease in a similar manner as given in the *fourth* plot, but experience a sharp decay after the 400th discretization point. In the eighth plot, the maximum of the triangular interfaces increase monotonically with the discetization point, and approach 0 at a later time. In the ninth plot, the portion of the long range couplings surface in between the maxima of every color line is achieved. In fact, after achieving the maxima, upon close examination one can see that the *yellow* lines continue to increase as the grid discetization point number increases, and then approach to 0 after a sufficient number of samples has been drawn.

- constructing the couplings within $B_{x_i}^\epsilon$, and outside of $B_{x_i}^\epsilon$, which are of the form $\mathcal{J}_{ij} = \frac{|t_i - t_j|}{\sum_{\text{Box}} t_k} \exp(-|x_i - x_j|)$, intentionally defined so that the turbulent flow between points that achieve a maximum distance away from each other in $B_{x_i}^\epsilon$ not only decays exponentially with respect to the Euclidean distance between the point, but also so that the long and short range couplings of \mathcal{H} can be formed by partitioning the sample array into the number of steps \mathcal{N} taken in each box of the discretization,
- computing \mathcal{H} ,
- comparing the probability of different configurations occurring, dependent on the random samples of the bridge from a fixed frame of reference, with the law $\mathbf{P} = \frac{\exp(-\mathcal{H})}{\mathcal{Z}}$, where $\mathcal{Z} = \sum_{\text{Box}} W(t)$, where $W(t)$ is the continuous trajectory of the bridge.

4 References

- [1] Albert, V., Covey, J. & Preskill, J. Robust Encoding of a Qubit in a Molecule. *Phys Rev* **10** 031050 (2020).

- [2] Apte, A., Auroux, D. & Ramaswamy, M. Observers for Compressible Navier-Stokes Equation. arXiv: 1503.05259 (2015).
- [3] Arnaudon, M. & Cruzeiro, A.B. Lagrangian Navier-Stokes Diffusions of Manifolds: Variational Principle and Stability. arXiv: 1004.2176 (2010).
- [4] Brandao, F. et al. Models of quantum complexity growth. arXiv: 1912.04297 (2019).
- [5] Charnyi, S., Heister, T., Olshanskii, M.A. & Rebholz, L.G. On conservation laws of Navier-Stokes Galerkin discretizations. *Journal of Computational Physics* **337** 289-308 (2016).
- [6] Chowdhury, A., Low, G.H. & Wiebe, N. A Variational Quantum Algorithm for Preparing Quantum Gibbs States. arXiv: 2002.00055 (2020).
- [7] Cresson, J. & Darses, S. Lagrangian Structure for the Stokes, Navier-Stokes and Euler Equations. arXiv: 0811.3286 (2008).
- [8] Eremenko, A. Spectral Theorems for Hermitian and Unitary Matrices. *Lecture Notes*.
- [9] Faist, P. et al. Continuous symmetries and approximate quantum error correction. arXiv: 1902.07714 (2019).
- [10] Gidney, C., Ekera, M. How to factor 2048 bit RSA integers in 8 hours using 20 million noisy qubits. arXiv: 1905.09749 (2019).
- [11] Hadfield, S., Wang, Z., O'Gorman, B., Rieffel, E., Venturelli, D. & Biswas, R. From the Quantum Approximate Optimal Algorithm to a Quantum Alternating Operator Ansatz. *Quantum Optimization Theory, Algorithms, and Applications* **34** 12.2 (2019).
- [12] Iverson, J. & Preskill, J. Coherence in logical quantum channels. *New Journal of Physics* **22** 073066 (2020).
- [13] Kandala, A., et al. Hardware-efficient Variational Quantum Eigensolver for Small Molecules and Quantum Magnets. *Nature* **549** 242 (2017).
- [14] Kim, I., Swingle, B. Robust entanglement renormalization on a noisy quantum computer. arXiv: 1711.07500 (2017).
- [15] Lubasch, M., et al. Variational quantum algorithms for nonlinear problems. *Phys Rev* **101** 010301 (2020).
- [16] McClean, J.R. et al. The theory of variational hybrid quantum-classical algorithms. *New J. Phys.* **18** 023023 (2016).
- [17] Nakaji, K. & Yamamoto, N. Expressibility of the alternating layered ansatz for quantum computation. arXiv: 2005.12537 (2020).
- [18] Otarod, S. & Otarod, D. Analytical Solutions for Navier-Stokes Equations In Two Dimensions For Laminar Incompressible Flow. arXiv: physics/0609186v1 (2006).
- [19] Orus, R. A Practical Introduction to Tensor Networks: Matrix Product States and Projected Entangled Pair States. *Annals of Physics* **349** 117-158 (2014).
- [20] Perez-Garcia, D., Verstraete, F., Wolf, M.M. & Cirac, J.I. Matrix Product State Representations. *Quantum Inf. Comput.* **7** 401 (2007).
- [21] Peruzzo, A., et al. A variational eigenvalue solver on a quantum processor. *Nature Communications* **5** 4213 (2014).
- [22] Preskill, J. Quantum computing in the NISQ era and beyond. *Quantum* **2**(79) (2018).
- [23] Sim, S., Johnson, P. & Aspuru-Guzik, A. Expressibility and entangling capability of parametrized quantum circuits for hybrid quantum-classical algorithms. *Advanced Quantum Technologies* **2**(12) (2019).
- [24] Sung, K., et al. Using models to improve optimizers for variational quantum algorithms. *Quantum Science and Technology* **5**(4) (2020).
- [25] Vedral, V., Barenco, A. & Ekert, A. Quantum Networks for Elementary Arithmetic Operations. *ArXiv*: quant-ph/9511018.

- [26] Xu, X. et al. Variational algorithms for linear algebra. arXiv:1909.03898 (2019).
- [27] Zhang, D.B., Zhan-Hao, Y. & Yin, T. Variational quantum eigensolvers by variance minimization. arXiv: 2006. 15781 (2020).
- [28] Zhu, R. & Zhu, X. Three-dimensional Navier-Stokes equations driven by space-time white noise. arXiv: 1406.0047 (2014).
- [29] Grotto, F. & Pappalettera, U. Gaussian invariant measures and stationary solutions to 2D primitive equations arXiv: 2005.03339 (2020).
- [30] Thapliyal, H., Munoz-Coreas, E., Varun, T.S.S. & Humble, T.S. *Quantum Circuit Designs of Integer Division Optimizing T-count and T-depth*. arXiv:1809.09732 (2018).
- [31] Zhuang, Q., Preskill, J. & Jiang, L. Distributed quantum sensing enhanced by continuous-variable error correction. *New Journal of Physics* **22** (2020).
- [32] Abughalia, M.A. On the mathematical solution of the 2D Navier Stokes equations for different geometries. *Advances in Fluid Mechanics* **39** 2006.

Landscape fluctuations in Cas12a binding

Pete Rigas, Lambert Lab

December 1, 2020

1 Introduction

Families of CRISPR proteins have attracted significant attention in recent studies, a few of which have devoted attention towards the regulation of microbial metabolic rate [19], genome engineering applications in Cas9 & Cas12 [6,11,13,15,17,27,35], dynamic imaging of telomeres [7], theoretically driven predictions of protein folding and atomistic simulation [22,24,25,34], and kinetic models detailing the process by which different Cas proteins identify target sequences and impact vital cellular functions [8-9,12,14,20,21,28]. In [29], a thermodynamic approach to model binding determinants is introduced, which is primarily rooted in analyses of the individual stages of Fn Cas12a binding which is comprised of PAM & crRNA inspection, followed by a reconfiguration stage. In the discussion, the authors reflect upon potential generalizations of the thermodynamics approach, particularly in making use of the formalism to interpret binding activity of catalytically active Cas12a nuclease.

Despite other studies which have implemented machine learning techniques to simulate trajectories in the energy landscape in efforts to provide analyses of binding for different proteins [10,16,30], as well as first principled models quantifying the expression of genes through transcription factors [5,33], generalizing the thermodynamic approach of [29] is advantageous in providing more interpretations of individual stages of binding for different Cas proteins which are known to variably depend on the random walk motion that the protein undergoes throughout the PAM inspection phase [29,32], in addition to blunt versus staggered cuts that are characteristic of Cas9 & Cas12, respectively [17,31,35]. To systematically quantify the rates at which particles diffuse across subsequent base pairs to an absorbing boundary as the Cas protein inspects a target sequence for complementarity, a dimensionless ODE from a well posed IVP is solved to obtain exit times. With numerical approximations to the solution, numerical approximations of the exit time of variable absorbing boundary length are obtained through studies of Fokker Plank type equations, whose IVPs can be placed into correspondence with those of the Langevin equation [21].

Computations of mean exit, or passage, times have been previously applied under diverse geometrical and biological constraints, with one study detailing a procedure for the reconstruction of drift terms through a change of variables transformation of the backward Kolmogorov equation to the Schrodinger equation, in addition to a mapping into the Euler Lagrange equations which recovers potentials [2,8]. Numerical manipulations of the solution to the ODE for numerical approximations to the first passage time can be readily adapted to obtain passage times across other base pairs in the target sequence by numerically adjusting the upper limit of integration in the solution, which in the case of simple classes of potentials can be approximated by Gaussians, yielding estimations for the first passage time from Kramer's Result, with other studies of similarly posed diffusion processes obtained from solutions of the Smoluchowski equation in [18].

For CRISPR-Cas binding, an IVP corresponding to the first passage problem can be formulated by enforcing initial conditions which stipulate that the position of the particle undergoing diffusion is centered at the origin when target inspection is initiated, and that the particle subject to a unit initial velocity. As the protein inspection continues for remaining base pairs in the sequence, passage times can be computed by making use of numerical relations from the closed form of solutions to the ODE, primarily based in obtaining three variational formulas involving participation from several terms. To satisfactorily generate realistic binding energy landscapes that proteins encounter throughout inspection, we reflect upon separate approaches to determine mean exit times, from one approach which is capable of obtaining the exit time through numerical approximations of solutions to a stochastically driven oscillator, while another method raises an inverse problem, similar to that studied in [2], in which potential energy landscapes can be uniquely reconstructed from distributions of exit times. The inverse problem formulation presented here is focused towards the construction of the binding landscape potential from collections of exit times up to an absorbing membrane of variable length. Additional comparisons between probability measures, in which probability measures with another Hamiltonian, against the probability measure $p_i = \exp(\nabla U_i)/Z$ with potential U_i , will also be established.

2 Methodology

2.1 Description

The inverse problem poised towards reconstruction of the binding potential from exit time distributions relies on the following framework. To study the rates at which particles diffuse across base pairs in the binding process throughout crRNA inspection, solutions τ to the dimensionless, second order ODE of the form,

$$-\mathcal{A} \frac{d^2\tau}{dx^2} + \mathcal{U}'(x) \frac{d\tau}{dx} = 1 ,$$

are determined where the normalization introduced to obtain the dimensionless equation is proportional to the product of the Boltzmann constant and ambient temperature of bond melting, $\mathcal{A} \equiv \frac{k_b T}{\nu}$, $\mathcal{U}'(x) \equiv \frac{U'(x)}{\nu}$, and $U'(x)$ is the potential landscape before normalization by the driving force ν . To specify classes of binding potentials for which solutions are to be determined, we impose the criterion that candidate potentials from the admissible landscape space possess one degree of freedom for each base pair at which binding occurs. In numerical applications of potential landscape reconstruction for mean exit time distributions, enforcing straightforward conditions on the mean and variance of the exit distributions themselves can respectively be achieved through specifying the first sample that is drawn from the time distribution, in addition to the maximum and minimum sample that can be drawn afterwards to specify the variance of the distribution which is also related to the fatness of its tails. To describe our parameter search for suitable potentials, we provide real and complex solutions to the well posed ODE above.

To provide solution dependent variational expressions for potential recovery given perturbations in mean exit time, in the following we specify the form of the potential from which approximations of mean exit time are obtained, in addition to the corresponding form of the predicted exit time from the solution. For each instance of the exit time τ , superscripts will denote underlying assumptions on the curvature of the potential landscape to obtain solutions. In one admissible class of potentials, solutions for the exit time to the ODE are representative of linear and exponential contributions, with the power of the exponent dependent on fluctuations in the landscape associated with x_1 . In one of the most simple cases, the solution for a potential whose first derivative is constant amongst all base pairs of the target sequence is,

$$\boxed{\tau_0} = -\frac{x(x-c)}{c} ,$$

for arbitrary c , while the solution for a potential with a constant rate of change amongst all base pairs in the target sequence is,

$$\boxed{\tau_{\text{Constant}}} = c - c \exp(-cx) - \frac{x}{\sqrt{c}} .$$

The power of the exponent quickly grows in complexity in correspondence to fluctuations of the potential. For the most complicated class of potentials which are composed of nonzero polynomial terms for each base pair in the target sequence, the power in solutions for exit time approximation takes the form

$$\boxed{\tau_{\text{Asym}}} \approx \int_0^x \int_0^x -\exp(-U) \exp(U) dudu + \int_0^x \int_0^v \exp(-V) \exp(-U) du dv + \int_0^x \exp(-U) du ,$$

where $U \equiv U(u)$, $V \equiv V(v)$ is an intermediate variable of integration for numerical approximation of the second term, and the subscript on the exit time τ indicates that the potential \mathcal{U} from which the solution is obtained has a higher order degree term dominating interactions from the potential, in addition to a lower degree term also responsible for fluctuations in the landscape and exhibits asymmetry. The fluctuations are precisely determined from polynomial terms in the potential, and can take the form

$$U = \frac{\pm}{\prod_i d^i} \sum_{\text{degrees}} p^{i+1} ,$$

where the product of nonzero polynomial terms p is proportional to the number of competing terms in the potential, d^i are the degrees of each nonzero term, and the normalization is proportional to the product of the degree of all nonzero terms. From the standard polynomial vector space, each potential can be placed into correspondence with one subspace. The complexity in the power of the exponential is similar to that of harmonic trap potentials, namely potential functions which, whether quadratic or cubic, provide solutions in which the complexity of U differs in the number of terms in the solution. Within this potential class, potentials with roots at the origin yield complex solutions, where from previous solutions of τ_{Asym} , exhibit a change of behavior in portions of the three integral terms for the approximation, as seen through contributions from incomplete Gamma function factors,

$$\boxed{\tau_{\Gamma \text{ Inc}}} \approx \frac{u^{\frac{1}{\text{Deg}}} \Gamma\left(\frac{1}{\text{Deg}}\right)}{\text{Deg}} - \frac{(\text{Deg})^{\frac{1}{\text{Deg}}} \Gamma_{\text{Inc}}\left(\frac{1}{\text{Deg}}, \frac{u^{\text{Deg}+1}}{\text{Deg}+1}\right)}{\text{Deg}+1} + (\text{Deg})^{\frac{1}{\text{Deg}}} \left(\Gamma_{\text{Inc}}\left(\frac{1}{\text{Deg}}, \frac{u^{\text{Deg}+1}}{\text{Deg}+1}\right) \right) \left(\int_0^x \exp\left(\frac{u^{\text{Deg}+1}}{\text{Deg}+1}\right) du \right) - \int_0^x \frac{(\text{Deg})^{\frac{1}{\text{Deg}}} \exp\left(\frac{u^{\text{Deg}+1}}{\text{Deg}+1}\right) \Gamma_{\text{Inc}}\left(\frac{1}{\text{Deg}}, \frac{u^{\text{Deg}+1}}{\text{Deg}+1}\right)}{\text{Deg}+1} du . \quad (\star)$$

where Deg is the degree of the singular term in the potential. Each $\Gamma, \Gamma_{\text{Inc}}$ factors in the solution is concentrated about the vanishing singularity, and by definition are, respectively, the Gamma and Incomplete Gamma factors,

$$\Gamma\left(\frac{1}{\text{Deg}}\right) = \int_0^\infty x^{\frac{1}{\text{Deg}}-1} \exp(-x) dx ,$$

and

$$\Gamma_{\text{Inc}}\left(\frac{1}{\text{Deg}}, \frac{u^{\text{Deg}+1}}{\text{Deg}+1}\right) = \int_{\frac{u^{\text{Deg}+1}}{\text{Deg}+1}}^\infty t^{\frac{1}{\text{Deg}}-1} \exp(-t) dt .$$

In the highest degree of polynomial complexity, statistical weights are assigned to each base pair of the sequence, and result in a similar expression, with solutions to the ODE taking the form

$$\boxed{\tau_{\text{Poly}}} \approx \int_0^x \int_0^x \prod_{i=2}^{20} \exp\left(-\frac{u^i}{i}\right) \prod_{i=2}^{20} \exp\left(\frac{v^i}{i}\right) du dv + \int_0^x \int_0^v \left\{ \prod_{i=2}^{20} \exp\left(-\frac{u^i}{i}\right) du \right\} \prod_{i=2}^{20} \exp\left(\frac{v^i}{i}\right) dv + \int_0^x \prod_{i=2}^{20} \exp\left(-\frac{u^i}{i}\right) du , \quad (\star\star)$$

reflective of contributions from all nonzero polynomial terms specified in the candidate potential. Under simple rearrangements, variational formulae for the difference of exit times $\Delta_\tau = \tau_{x_2} - \tau_{x_1}$ are obtained through analyzing, on a case by case basis, the space of possible combinations of absorbing membrane lengths at arbitrary positions $x_1 < x_2$ of the target sequence. Once the formulae have been established, further discussion will be devoted towards the construction of admissible distributions from which potential landscapes can be reconstructed. Before derivations of the variational formulae, we characterize the dependence between solutions and the class of potentials that we have identified, with solutions for varying arrangements of absorbing membranes.

Within the potential space, the goal of numerically obtaining mean exit times is to generate small perturbations to the energy landscape corresponding to small perturbations in the exit time. Regardless of experimental constraints in experiments that have been carried through measurements of the rate at which reactants are consumed in Fn Cas12a binding [29], the inverse problem of recovering the landscape can be numerically realized readily in several ways. First, one method involves producing approximations of the mean exit time from a given potential through Gaussian approximations on the integral terms from τ , while another second closely related numerical approach involves numerically approximating the exit time after rearranging terms from τ through possible values on the innermost variable v of integration from the second term in τ . Third, another approach entails that we rearrange terms from τ depending on the position of the exit time of interest v , in which it is possible to make use of linearity of the integral to obtain variational relations below.

Before proceeding with computations to determine the participation from different fluctuation modes in the landscape, we denote solutions \mathcal{S} for the relation corresponding to each assumption considered thus far on \mathcal{U} . For landscape potentials

corresponding to τ_0 , variational relations will first be derived, to then accommodate more complicated relations for more complex landscapes.

Finally, before more remarks surrounding the procedure and variational relations from different classes of potentials, another class of potentials from the natural logarithm allow for simplifications to τ approximations, under the same general form of τ_{Asym} for arbitrary c ,

$$\begin{aligned} \tau_{\log} \approx & \int_0^x \int_0^x -\exp\left(\{\log(u-c)-1\}(u-c)\right) \exp\left(-\{\log(u-c)-1\}(u-c)\right) du \, du - \\ & \exp\left(c-\log(c)\right) \int_0^x \exp\left(-\{\log(u-c)-1\}(u-c)\right) du + \\ & \int_0^x \int_0^v \exp\left(\{-\log(v-c)-1\}(v-c)\right) \exp\left(\{\log(u-c)-1\}(u-c)\right) dv \, du , \end{aligned}$$

which can be simplified significantly, through rearrangements of the power of the exponent of the integrand

$$\pm \exp\left(\pm \{\log(u-c)-1\}(u-c)\right) = \pm \exp\left(\pm u \log(u-c) \mp c \log(u-c) \mp u \pm c\right) ,$$

in turn resulting with an expression dependent on the variable position of exit time x , which is of the form

$$\begin{aligned} \tau_{\log} \approx & \int_0^x \left\{ \int_0^x - (u-c)^{u-c} e^{c-u} du \right\} \frac{1}{(u-c)^{u-c} e^{c-u}} du - \\ & \exp\left(c-\log(c)\right) \int_0^x \frac{1}{(u-c)^{u-c} e^{c-u}} du + \\ & \int_0^x \int_0^v \exp(-v) \exp(c) (v-c)^{-v+c} dv \exp(v) \exp(-c) (v-c)^{v-c} du , \end{aligned}$$

an expression dependent on linear, quadratic and exponential terms. Finally, cancellations yield

$$\boxed{\tau_{\log}} \approx -\exp\left(c-\log(c)\right) \int_0^x \frac{1}{(u-c)^{u-c} e^{c-u}} du .$$

For exit time approximations τ_0 corresponding to potentials with a vanishing first derivative, fluctuations in the landscape from corresponding fluctuations in the landscape can be studied with the following procedure. For each variational relation, several approximations provided in *Table 2* are obtained from apriori knowledge of the exit time and associated potential at an arbitrary position x_1 .

Numerical approximations in future sections are readily obtained from rearrangement with the intermediate variable of integration v , in addition to specification of the position up to which the mean exit time is to be computed. From $\mathcal{S}_{v \neq x}$, terms from the numerical approximation of exit times are implemented in the following cases. In the formulae, the passage time up to the first position x_1 , interactions over the passage time to x_2 , and the intermediate interactions between the first and second passage times numerically contribute, from which variations in one exit time parameter generate classes of potential landscapes. For the inverse problem, at onset we require specification of one basis element in the potential space, and its corresponding exit time, in addition to the deviation from the exit time through specification of the second exit time. The potential corresponding to the second exit time can be recovered through numerical approximation of the variational formulae. To distinguish between potential landscapes, we denote free variables of the potential associated with the second exit time τ_2 at x_2 with $u_{x_2} \equiv u_2$, and similarly, free variables of the potential associated with the remaining exit time at an earlier position x_1 with $u_{x_1} \equiv u_1$. Before numerically approximating the final expression, we must evaluate the inner order of integration with intermediate variables v_1 and v_2 . Tables corresponding to each formula in *Section 2* illustrate approximations associated with the exit time for potential recovery up to x_1 , besides the upper limit of the second order of integration that can be numerically adjusted to obtain exit times of varying base pair length. Over previous works that have been mentioned, advantages of this approach include the flexibility to determine fluctuations in the energy landscape up to a base pair position at which the exit time is determined. Sampling at random from exit time distributions enables potential recovery with the variational relations.

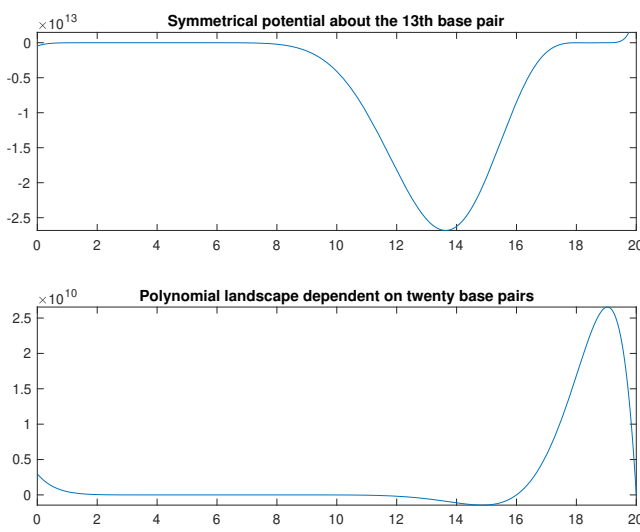


Figure 1: (i) Plots of exit time distributions for logarithmically dependent class of potentials. Symmetrical potential about the 13th base pair. A third class of admissible potentials from which exit time approximations are presented for is τ_{Sym} . About the thirteenth base pair of the sequence, the landscape potential exhibits a potential well, and is otherwise roughly constant. (ii) Polynomially dependent on twenty base pairs. A final potential is shown which is asymmetrically balanced, as contributions from the potential heavily rely on the last few base pairs of the target sequence.

In the following, depending on the case it is necessary that we isolate intervals over which the exit time is computed to ease numerical approximation by combining integral terms together. Instead of having to solve multiple IVPs in parallel at once to determine the exit time, we formulate an approach to study an inverse problem for determining the landscape potential corresponding to the exit time. For numerical approximations of fluctuations in exit time, the potential corresponding to x_1 can be expressed in terms of contributions from the potential variables for x_1 and those for x_2 . As an implicitly defined surface in potential variables of x_1 and x_2 , the fluctuations of the landscape corresponding to passage at x_2 is a locus of points in the (x_1, x_2) plane. Taking level sets of the surface of the curve in the plane corresponds to horizontally or vertically displaced intersections of the expression of potential variables for x_1 and x_2 . In the realization of the variational formula, solutions can be fashioned towards recovering potential landscapes for the passage times through a fluctuation of the exit time encountered at x_1 with τ_{x_1} by choosing another exit time τ_{x_2} , in which Δ_τ takes the form, for solutions $\mathcal{S}_{v \neq x} \equiv \mathcal{S}$,

$$\Delta_\tau \equiv \tau_{x_2} - \tau_{x_1} = \mathcal{S}(x_2) - \mathcal{S}(x_1) ,$$

in which case the subscript draws attention towards the role of v as an intermediate variable of integration which is independent of the variable boundary of the absorbing membrane at x .

For instance, in each previous expression of τ , the procedure described below through the variational relation approximates admissible potentials within the landscape space, through the order of fluctuation $\Delta_\tau = \tau_{x_2} - \tau_{x_1}$ for exit times τ_{x_1} and τ_{x_2} , are provided in *Table 1*. Each relation coincides with an approximation for the implicitly defined surface in the plane dependent on the potential associated with the exit time at x_1 , in addition to the potential at x_2 . c_1, c_2 are arbitrary.

For exit time approximations with three integral terms, as shown below, computing the order of Δ_τ requires manipulation. We introduce straightforward relations for linearity amongst the inner, and outermost, variables, respectively, in which interchanging the order in the outermost variable in the second term yields for exit time approximations from polynomially dependent potentials,

$$-\int_0^{x_2} \left(\int_{u_2}^{x_2} \left\{ \prod_{i=2}^{20} \exp\left(\frac{v_2^i}{i}\right) - 1 \right\} dv_2 \right) \prod_{i=2}^{20} \exp\left(\frac{u_2^i}{i}\right) du_2 = -\int_0^{x_1} \left(\int_{u_2}^{x_2} \left\{ \prod_{i=2}^{20} \exp\left(\frac{v_2^i}{i}\right) - 1 \right\} dv_2 \right) \prod_{i=2}^{20} \exp\left(\frac{u_2^i}{i}\right) du_2 - \int_{x_1}^{x_2} \left(\int_{u_2}^{x_2} \left\{ \prod_{i=2}^{20} \exp\left(\frac{v_2^i}{i}\right) - 1 \right\} dv_2 \right) \prod_{i=2}^{20} \exp\left(\frac{u_2^i}{i}\right) du_2 . \quad (\text{Lin})$$

Formula	Approximation of recovered modes
Var1,	$\mathcal{R} \approx \sum_{i=2}^{20} \left(-\frac{x_1^{i+2}}{(i+1)(i+2)} + \frac{x_1^{i+1}}{i+1} \right)$
Var2	$\mathcal{R} \approx \mathbf{Var1} + \frac{1}{2} \sum_{i=2}^{20} \frac{x_1^{3i+2}}{i^2(i+1)} \left(\frac{1}{3i+2} - \frac{1}{2i+1} \right)$
Var3	$\mathcal{R} \approx \mathbf{Var2} + \frac{1}{3} \sum_{i=2}^{20} \frac{x_1^{i+5}}{3i+3} \left(\frac{1}{i+5} - \frac{1}{4} \right)$
general Var	$\mathcal{R} \approx \mathbf{Var3} + \sum_{j \in \mathcal{M}_{-3}} \sum_{i=2}^{20} \frac{x_1^{i+j+2}}{j(i+1)} \left(\frac{1}{i+j+2} - \frac{1}{j+1} \right)$

Table 1: *Numerical instances of (Var) with membranes of absorbing unit or varying boundary length.* In each instance, Variational relations from (Var) in the Poly polynomial class of potentials are obtained from enforcing numerical approximations from fixed values of x_1 and x_2 . From the specification of these free parameters, corresponding numerics can be performed to recover all corresponding potential modes, in light of the formulation for \mathcal{R} given in *Table 1*. Fluctuations of the potential landscape from the exit time corresponding to x_1 can be approximated from the deviation between exit times τ_{x_1} & τ_{x_2} . The approximation returns an surface in x_1 and x_2 . As a generalization of the approximation for recovered modes, in the final row an expression for additional terms in the expansion is provided. The j summation is taken over the collection of modes \mathcal{M} indexed by the naturals, and $\mathcal{M}_{-3} = \mathcal{M} \setminus \{1, 2, 3\}$.

2.2 Left hand side of (Var) relation for Poly class

To obtain equations for implicitly defined surfaces in terms of x_1 and x_2 potential variables, we illustrate typical rearrangements of terms from numerical approximations for the Poly class of potentials. Substituting in for solutions \mathcal{S} gives

$$\begin{aligned}
& - \int_0^{x_2} \left(\int_{u_2}^{x_2} \left\{ \prod_{i=2}^{20} 2 \exp\left(-\frac{v_2^i}{i}\right) \right\} \right) dv_2 \prod_{i=2}^{20} \exp\left(\frac{u_2^i}{i}\right) du_2 + \int_0^{x_2} \prod_{i=2}^{20} \exp\left(-\frac{u_2^i}{i}\right) du_2 + \\
& \int_0^{x_1} \left(\int_{u_1}^{x_1} \left\{ \prod_{i=2}^{20} 2 \exp\left(-\frac{v_1^i}{i}\right) \right\} \right) dv_1 \prod_{i=2}^{20} \exp\left(\frac{u_1^i}{i}\right) du_1 - \int_0^{x_1} \prod_{i=2}^{20} \exp\left(-\frac{u_1^i}{i}\right) du_1 .
\end{aligned}$$

For exit times in which the length of the absorbing boundaries at exit times τ_{x_1} and τ_{x_2} for x_1, x_2 along the genome, the variational formula (Var) permits for solutions to the inverse exit time problem through specification of the exit time parameters and distribution. We further rearrange terms to obtain the desired relation, through relevant applications of (Lin) to collect like terms,

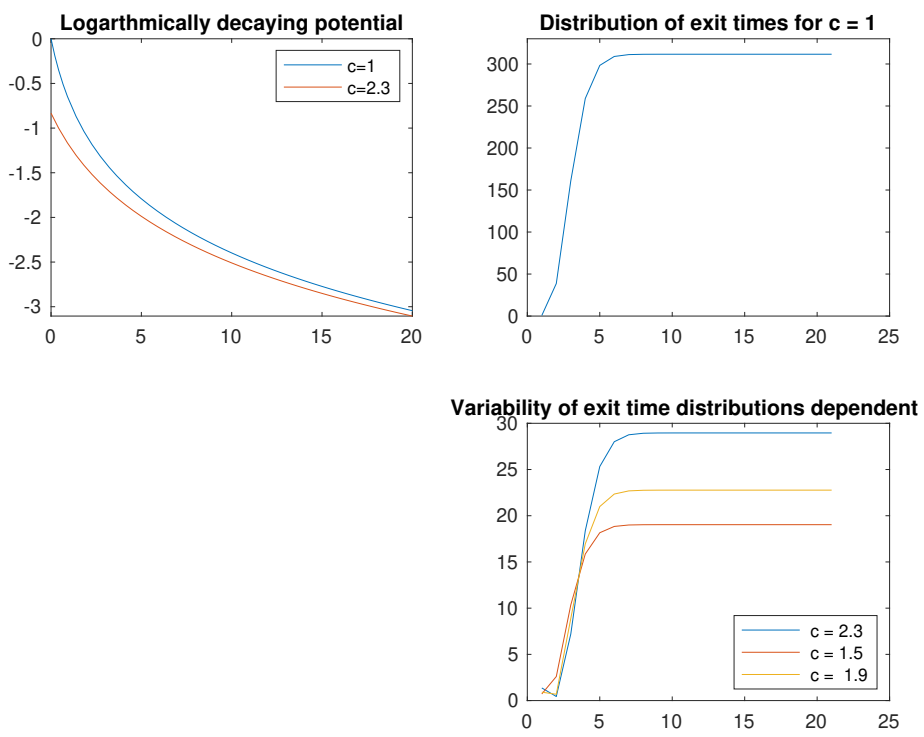


Figure 2: Plots of exit time distributions for logarithmically dependent class of potentials. (i) Potentials decaying logarithmically with respect to the location of the base pair of the target sequence are shown for $c = 1$ & $c = 2.3$. (ii) Plot of the distribution of exit times for $c = 1$. As the length of the absorbing membrane is varied across the length of the target sequence, numerical approximations of the exit time asymptote to a stationary time of approximate magnitude 300. (iii) Additional plots of exit time distributions for other c .

$$\int_0^{x_2} \left\{ \int_{u_2}^{x_2} \prod_{i=2}^{20} 2 \exp\left(-\frac{v_2^i}{i}\right) dv_2 + 1 \right\} \prod_{i=2}^{20} \exp\left(-\frac{u_2^i}{i}\right) du_2 - \int_0^{x_1} \left\{ \int_{x_1}^{u_1} \left\{ \prod_{i=2}^{20} 2 \exp\left(-\frac{v_1^i}{i}\right) dv_1 - 1 \right\} \prod_{i=2}^{20} \exp\left(-\frac{u_1^i}{i}\right) du_1 \right\}$$

(Var)

In Table 1 and Table 2, we provide expressions for the variational relations which allows for comparisons between the composition of the potential and the corresponding exit time approximation.

2.3 Numerical test cases

We review the composition of each variational relation for potential recovery.

- **(Var), (Var1):** The first two variational formulas encapsulates straightforward numerical behaviors of the fluctuations in the potential landscape from corresponding fluctuations in the exit time. From the expression, fluctuations up to first order are captured from terms in the potential expansion.
- **(Var2):** For exit times at x_1 & x_2 , the second variational formula encapsulates higher order fluctuations in the landscape with an additional term in the series expansion. For convenience, we rearrange terms by collecting powers of the common x_1 term, while leaving the remaining fractional terms separately.
- **(Var3):** For exit times at x_1 & x_2 , cubic order terms from the expansion in (Var3) capture fluctuations farther along the target sequence.
- general **(Var):** For exit times at x_1 & x_2 , the final variational formula is comprised of a mixture of contributions similar to the previous ones, in which contributions from the series are indexed by j which runs along \mathcal{M} which could contain an arbitrary number of modes. All previous terms in (Var1), (Var2), (Var3) can be determined by respectively taking the $j = 1, 2, 3$ mode from the series.

Exit time class	Recovery formulation \mathcal{R} of u_1 terms of potential
τ_0	$\Delta_\tau + \frac{x_2(x_2 - c_1)}{c_1}$
τ_{Constant}	$\Delta_\tau - c_1 - c_1 \exp(-c_1 x) - \frac{x}{\sqrt{c_1}}$
$\tau_{\text{Asym}\setminus\text{Sym}}, \tau_{\text{Poly}}$	$\Delta_\tau - \int_0^x \int_0^x -\exp\left(\frac{\sum_{\text{degrees}} p(u)^{i+1}}{\prod_i d^i}\right) \exp\left(\frac{\sum_{\text{degrees}} p(u)^{i+1}}{\prod_i d^i}\right) du \, du - \int_0^x \int_0^v \exp\left(-\frac{\sum_{\text{degrees}} p(v)^{i+1}}{\prod_i d^i}\right) \exp\left(\frac{\sum_{\text{degrees}} p(u)^{i+1}}{\prod_i d^i}\right) du \, dv - \int_0^x \exp\left(-\frac{\sum_{\text{degrees}} p(u)^{i+1}}{\prod_i d^i}\right) du$
$\tau_{\Gamma \text{ Inc}}$	$\Delta_\tau - \frac{1}{\text{Deg}+1} \left((\text{Deg})^{\frac{1}{\text{Deg}}} \Gamma_{\text{Inc}}\left(\frac{1}{\text{Deg}}, \frac{u^{\text{Deg}+1}}{\text{Deg}+1}\right) - \int_0^x \text{Deg}^{\frac{1}{\text{Deg}}} \exp\left(\frac{u^{\text{Deg}+1}}{\text{Deg}+1}\right) \Gamma_{\text{Inc}}\left(\frac{1}{\text{Deg}}, \frac{u^{\text{Deg}+1}}{\text{Deg}+1}\right) \right) + \dots$
τ_{\log}	$\Delta_\tau + \exp\left(c_1 - \log(c_1)\right) \int_0^{x_1} (u - c_1)^{-(u - c_1)} e^{-(c_1 - u)} du$

Table 2: *General formula for potential recovery from (Var)*. The relation is obtained through straightforward rearrangements of Δ_τ , returning an expression for the potential energy landscape up to x_1 . To readily apply the formula, we introduce approximations of $\exp(\sum_{i=2}^{20} -\frac{u_i^i}{i}) \sim 1 + \frac{(\sum_i -\frac{u_i^i}{i})^2}{2} + \dots + \frac{(\sum_i -\frac{u_i^i}{i})^n}{n} + \dots$. We make use of this guiding approximation to obtain recovered modes in *Table 2* below. Fluctuations of the energy landscape are obtained by incorporating terms from the mode approximation of the landscape potential as the position of exit time along the target sequence increases. From each approximation of τ that is introduced under different assumptions on the potential, the approximation between the recovered terms of the potential \mathcal{R} enables approximations of the landscape corresponding to the magnitude of the exit time τ_{x_2} at x_2 . With additional information regarding another position x_1 , in comparison to for potentials in correspondence with subspaces of the standard polynomial vector space of up to dimension 20. Across all relations, observe that the magnitude of Δ_τ is common, with fluctuations to Δ_τ from contributions of potential dependent terms. Perturbing the order of the fluctuation readily impacts the distribution of exit times for a particular CRISPR protein. \mathcal{R} provided for the cases $\tau_{\text{Asym}\setminus\text{Sym}}, \tau_{\text{Poly}}$ is identical to τ_{Poly} provided in $\star\star$. Within the Poly class, the solutions to well posed IVPs with initial position zero and initial unit velocity are of the form, $\mathcal{S}_{v \neq x}(v, x) \equiv -\int_0^x (\int_v^x \{\prod_{i=2}^{20} 2 \exp(-\frac{u^i}{i})\}) du \prod_{i=2}^{20} \exp\left(\frac{v^i}{i}\right) dv + \int_0^x \prod_{i=2}^{20} \exp\left(-\frac{u^i}{i}\right) du$. In \mathcal{R} for τ_{Log} , $p(u)$ and $p(v)$ denote contributions from a logarithmically dependent landscape in u and v , with v integrated out.

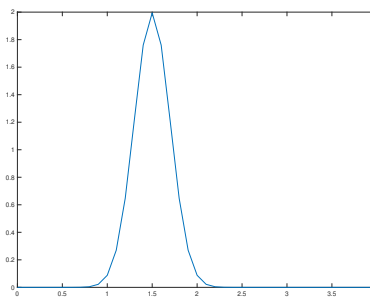


Figure 3: Normal distribution from which samples can be drawn for approximation of time increments $\Delta\tau$. Dependent on the fluctuation magnitude, samples from a normally distributed exit time distribution can be drawn within two standard deviations above or below the mean of the distribution to observe corresponding fluctuations in the landscape surface up to the position of exit at x_2 . Amongst different classes of potentials, the composition of the potential itself (*Tables 1 & 2*) demonstrate the order of fluctuation on $\Delta\tau$ from contributions of potential variables in x_1 .

2.4 Generating exit time distributions

We readily generate exit time distributions from which potential landscapes will be recovered. In a suitable free parameter generalization for different Cas proteins, the exit time formalism must be capable of determining the perturbation in the landscape given an initial potential choice with degrees of freedom at each base pair. The three variational formulae that have been presented are capable of executing the potential reconstruction, in addition to other quantities pertaining to the drift terms associated with well characterized properties of protein kinetics [2].

This final subsection is devoted towards not only a description of how the visit distributions for the exit times can be generated, but also how apriori choices of the exit times at both positions, in addition to the potential corresponding to the first exit time, can be enforced. The implementation of our approach is capable of recovering potentials associated with the free exit time, permitting for numerical simulations of energy landscapes for different Cas proteins. To numerically implement the variational formulae for landscape reconstruction, we make use of individual instances of the relation described extensively above. Primarily, we are interested in determining the order of difference in the exit times across subsequences of the target sequence that are at least one base pair long, despite being able to compute orders of magnitude of difference between exit times across shorter nucleotide lengths than 1. To identify the order of fluctuations within the parameter space that are valuable for physical interpretation, we devote the most attention towards cases of the formulae which are applicable in experiments for analyzing curvature of the energy landscape.

2.5 Procedure

We provide numerical results and interpretations in light of the relations given in the previous section. The ingredients are listed below.

2.5.1 Representative distributions

We execute numerical experiments to recover potential landscapes from candidate distributions. Normal distributions as shown in *Figure 1* are one suitable distribution class given that any exit time can be sampled from the distribution within two standard deviations to obtain fluctuations in the energy landscape. To recover corresponding potential landscapes, we evaluate terms of the series given in **(Var1)**, **(Var2)**, **(Var3)**, general **(Var)**, in turn obtaining x_1 variables for the potential which are normalized by terms dependent on i . In the vanishing limit of the variance of the distribution, the concentration of exit times about the mean of the distribution provides more fine grain numerical measures of the perturbation to the energy landscape at given positions of exit x_1 and x_2 .

2.6 Computations for potential recovery at x_2

To recover approximations of landscape modes, we further illustrate how sampling from typical distributions, as shown above, enable for efficient landscape recovery. First, it is necessary that we specify the initial exit time up to x_1 , from which the corresponding potential landscape can be obtained. Recall that from approximations of τ for solutions of the dimensionless second order ODE, specifying τ_{x_1} readily yields the following landscape associated with the exit time, through rearrangements for the potential modes given a polynomial locus in u_1 . Term by term we determine the landscape associated with $x \equiv x_1$, from the approximations of τ . We analyze contributions from well posed solutions through numerical investigation of the relations provided in *Table 2*.

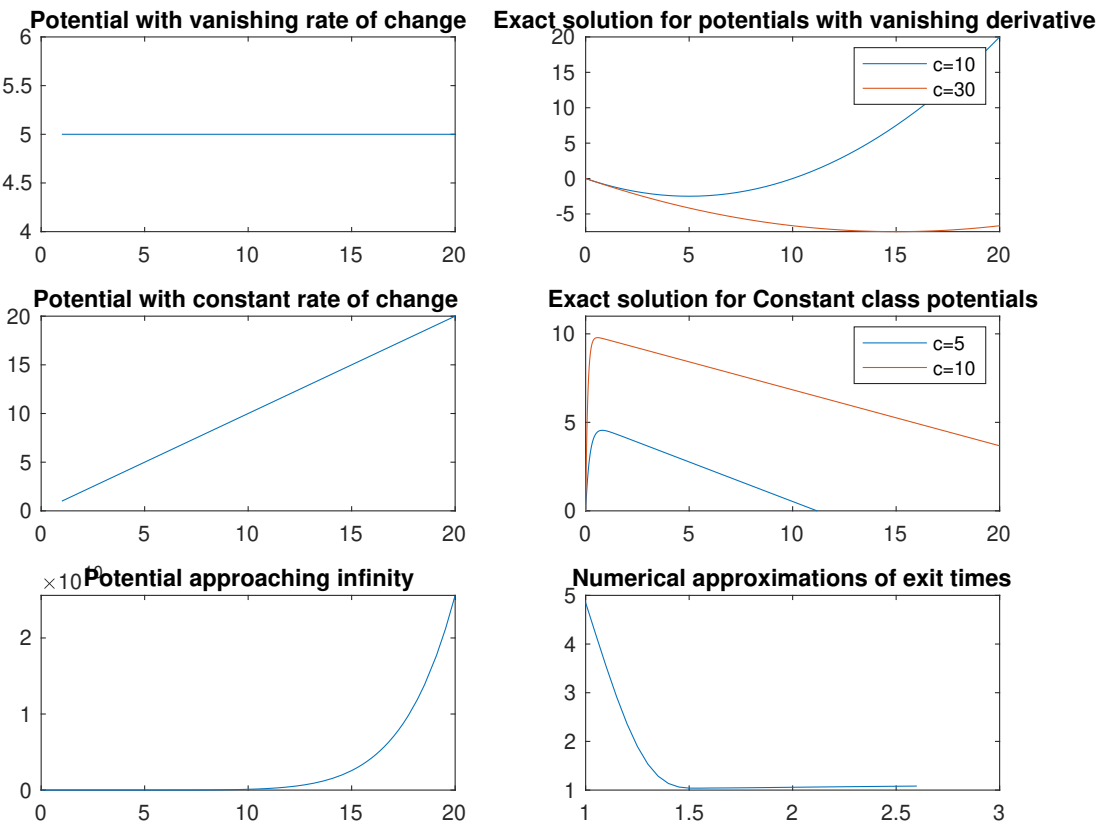


Figure 4: Plotting τ as a function of absorbing membrane boundary length. (i) Potential with vanishing rate of change. A potential which is constant across all base pairs can yield solutions to the right with different limiting exit times for base pairs infinitely far down the genome. (ii) Exact solution for potentials with vanishing derivative. The plots of exit time distributions for two values of c are shown. For $c = 10$, the exit time distribution increases monotonically with respect to the base pair of the target sequence, while for $c = 15$, the exit time decreases monotonically with respect to the base pair of the target sequence. (iii) Potential with constant rate of change. Another class of potentials from which expressions of τ_{Constant} were provided is the potential family whose landscape varies linearly with respect to the base pair of the target sequence. (iv) Exact solution for constant class of potentials. The exit time distributions for $c = 5$ and $c = 10$ are shown. For the corresponding exit time distribution accompanying the Constant potential class, perturbing the value of c impacts the duration of base pairs along the sequence before which the exit time vanishes. (v) Potential approaching infinity. Within the polynomial class of potential landscapes, taking the potential $\mathcal{U}' = x^8$ yields numerical approximations for the exit time which are provided in the accompanying plot to the right. (vi) Numerically, finite exit times can be readily approximated for up to two base pairs. The scheme to obtain the points along the exit time distribution are obtained as follows. From expressions in the solutions to the IVP discussed previously, from which exit times are numerically approximated between the first and second base pair of the binding sequence by varying the upper limit of integration x .

2.7 Numerical experiments

To further study recovered modes of landscapes, we implement the procedure to estimate \mathcal{R} from *Table 1*, to then apply higher modes of the landscape given in *Table 2*. Specifically, we establish the following criterion to generate theoretical predictions with regards to fluctuations of the landscape up to positions x_2 given initial data of the exit time magnitude and potential landscape at x_1 . To this end, we gather results surrounding different classes of potentials and plots of the corresponding exit times with respect to membrane boundary length. Partial results are provided in *Figure 4* above.

3 Alternative formulation of the probability measure on binding configurations

Alternatively, to establish another point of comparison from the probability measure $p_i = \exp(\nabla U_i)/Z$, from first principles another probability measure will be constructed as follows. Drawing inspiration from statistical mechanical models for Fn Cas12a binding in [29], we define the measure

$$\mu(N, N_{\text{mis}}, |X_{\text{mis}}|, |\text{mis}|, \lambda_{\text{mis}}) = \frac{\exp\left(\sum_{i \sim j} -\frac{w}{(|\{\text{mat}\}|+2)^3} \mathcal{J}_{ij} \sigma_i \sigma_j - \sum_{i \not\sim j} \frac{w}{(|\{\text{mis}\}|+2)^3} \mathcal{J}_{ij} (1 - \sigma_i \sigma_j)\right)}{1 + \lambda_c e^{-\beta \epsilon_{\text{PAM}}} + N_{\text{mis}} \sum_{\text{mis}} \lambda_{\text{mis}} e^{-\lambda_{\text{mis}} X_{\text{mis}}}},$$

as a function of the binding site N of the protein, the number of mismatches at sites N_{mis} , the locations of mismatches between the target and guide sequence $|X_{\text{mis}}|$, the cardinality of mismatches throughout the protein inspection phase $|\text{mis}|$, w is a suitably chosen statistical weight for each base pair, and an auxiliary parameter λ_{mis} which numerically allows for modulation of the probability of a binding configuration in the presence of mismatches between the target and guide sequences. The couplings from the Hamiltonian satisfy $\mathcal{J}_{ij} = |N - j|$ if $\sigma_i = \sigma_j$ and $\mathcal{J}_{ij} = 1 - |N - j|$ otherwise. The partition function which normalizes the numerator so that μ is a probability measure over the binding configuration sample space has separate exponentials to account for energy associated with the PAM inspection of Fn Cas12a, in addition to the summation over mismatch terms which themselves are also exponentials with λ_{mis} freely chosen.

For convenience, by elementary properties of the exponential we can rearrange terms to obtain a product measure over the match and mismatch terms between the guide and target sequences, which takes the form,

$$\begin{aligned} \exp(-\mathcal{H}) &= \exp\left(-\frac{w}{(|\{\text{mat}\}|+2)^3} \sum_{i \sim j} \mathcal{J}_{ij} \sigma_i \sigma_j - \frac{w}{(|\{\text{mis}\}|+2)^3} \sum_{i \not\sim j} \mathcal{J}_{ij} (1 - \sigma_i \sigma_j)\right) \\ &= \prod_{i \sim j} \exp\left(-\frac{w}{(|\{\text{mat}\}|+2)^3} \mathcal{J}_{ij} \sigma_i \sigma_j\right) \prod_{i \not\sim j} \exp\left(-\frac{w}{(|\{\text{mis}\}|+2)^3} \mathcal{J}_{ij} (1 - \sigma_i \sigma_j)\right), \end{aligned}$$

The resulting measure on binding configurations is,

$$\mu(N, N_{\text{mis}}, |X_{\text{mis}}|, |\text{mis}|, \lambda_{\text{mis}}) = \frac{\prod_{i \sim j} \exp\left(-\frac{w}{(|\{\text{mat}\}|+2)^3} \mathcal{J}_{ij} \sigma_i \sigma_j\right) \prod_{i \not\sim j} \exp\left(-\frac{w}{(|\{\text{mis}\}|+2)^3} \mathcal{J}_{ij} (1 - \sigma_i \sigma_j)\right)}{1 + \lambda_c e^{-\beta \epsilon_{\text{PAM}}} + N_{\text{mis}} \sum_{\text{mis}} \lambda_{\text{mis}} e^{-\lambda_{\text{mis}} X_{\text{mis}}}},$$

where the contributions from the base pair matches and mismatches in the target sequence are normalized by a constant dependent on the total number of matches and mismatches between the guide and target sequences. Thermodynamically, CRISPR proteins that successfully bind to target along the genome form a stably bound complex that occupies the binding site for an interval of time that has been measured from experiments discussed in [29]. From the measure above, the stationary distribution of visits of a random walk whose transition probabilities are in correspondence with probabilities of obtaining binding configurations that can be readily computed from μ above arise from the following condition

$$\mu(N, N_{\text{mis}}, |X_{\text{mis}}|, |\text{mis}|, \lambda_{\text{mis}}) < \mu(N, N_{\text{mis}+1}, |X_{\text{mis}+1}|, |\text{mis}+1|, \lambda_{\text{mis}+1}).$$

The condition above stipulates that the probability of the random walk surpassing an arbitrary threshold of visits at a mismatch position between the target and guide sequences is smaller than the probability of the random walk surpassing an arbitrary threshold of visits at the position had there been a match between the target and guide sequences, leading to the rearrangements,

$$\begin{aligned} &\frac{\prod_{i \in \text{Mat}_i} e^{-\frac{w_i}{N} \mathcal{J}_{ij} \sigma_i \sigma_j} \prod_{i \in \text{Mis}_i} e^{-\frac{w_i}{N} \mathcal{J}_{ij} (1 - \sigma_i \sigma_j)}}{1 + \lambda_p e^{-\beta \epsilon_p} + \frac{|\text{Mat}_i|}{N} \lambda_c e^{-\beta \epsilon_c} + (N - X_{\text{mis}})^3 \sum_{\text{mis}} \dots} \\ &< \frac{\prod_{i \in \text{Mat}_{i+1}} e^{-\frac{w_i}{N} \mathcal{J}_{ij} \sigma_i \sigma_j} \prod_{i \in \text{Mis}_{i+1}} e^{-\frac{w_i}{N} \mathcal{J}_{ij} (1 - \sigma_i \sigma_j)}}{1 + \lambda_p e^{-\beta \epsilon_p} + \frac{|\text{Mat}_{i+1}|}{N} \lambda_c e^{-\beta \epsilon_c} + (N - X_{\text{mis}})^3 \sum_{\text{mis}} \dots} \end{aligned}$$

which implies,

$$\begin{aligned}
1 + \frac{|\text{Mat}_{i+1}|}{N} e^{-\beta\epsilon_c} \lambda_c + \sum_{\text{mis} \in \text{Mis}_{i+1}} (N - X_{\text{mis}})^3 \lambda_{\text{mis}} e^{-\lambda_{\text{mis}} X_{\text{mis}} + \ln(N_{\text{mis}})} &< \prod_{i \in \text{Mis}_i \cap \text{Mis}_{i+1}} e^{-\frac{w_i}{N} \mathcal{J}_{ij} \sigma_i \sigma_j} \left(1 + \frac{|\text{Mat}_i|}{N} e^{-\beta\epsilon_c} \lambda_c \right. \\
&\quad \left. + \sum_{\text{mis} \in \text{Mis}_i} (N - X_{\text{mis}})^3 \lambda_{\text{mis}} e^{-\lambda_{\text{mis}} X_{\text{mis}} + \ln(N_{\text{mis}})} \right), \\
&\Updownarrow \\
1 + \left(\frac{|\text{Mat}_{i+1}|}{N} - \frac{|\text{Mat}_i|}{N} \prod_{i \in \text{Mis}_i \cap \text{Mis}_{i+1}} e^{-\frac{w_i}{N} \mathcal{J}_{ij} \sigma_i \sigma_j} \right) e^{-\beta\epsilon_c} \lambda_c + \sum_{\text{mis} \in \text{Mis}_{i+1}} (N - X_{\text{mis}})^3 \lambda_{\text{mis}} e^{-\lambda_{\text{mis}} X_{\text{mis}} + \ln(N_{\text{mis}})} \\
&- \prod_{i \in \text{Mis}_i \cap \text{Mis}_{i+1}} e^{-\frac{w_i}{N} \mathcal{J}_{ij} \sigma_i \sigma_j} \sum_{\text{mis} \in \text{Mis}_i} (N - X_{\text{mis}})^3 \lambda_{\text{mis}} e^{-\lambda_{\text{mis}} X_{\text{mis}} + \ln(N_{\text{mis}})} &< \prod_{i \in \text{Mis}_i \cap \text{Mis}_{i+1}} e^{-\frac{w_i}{N} \mathcal{J}_{ij} \sigma_i \sigma_j},
\end{aligned}$$

For multiple base pair mismatches between the target and guide sequences, one obtains a similar expression,

$$\begin{aligned}
(N - X_{\text{mis}_{i+1}})^3 \lambda_{\text{mis}} e^{-\lambda_{\text{mis}} X_{\text{mis}} + \ln(N_{\text{mis}})} + \sum_{\text{mis} \in \text{Mis}_i} \left(1 - \prod_{i \in \text{Mis}_i \cap \text{Mis}_{i+1}} e^{-\frac{w_i}{N} \mathcal{J}_{ij} \sigma_i \sigma_j} \right) (N - X_{\text{mis}})^3 \lambda_{\text{mis}} e^{-\lambda_{\text{mis}} X_{\text{mis}} + \ln(N_{\text{mis}})} \\
< \prod_{i \in \text{Mis}_i \cap \text{Mis}_{i+1}} e^{-\frac{w_i}{N} \mathcal{J}_{ij} \sigma_i \sigma_j} \\
&\Updownarrow \\
(N - X_{\text{mis}_{i+1}})^3 \lambda_{\text{mis}} e^{-\lambda_{\text{mis}} X_{\text{mis}} + \ln(N_{\text{mis}})} + \sum_{\text{mis} \in \text{Mis}_i} \left(1 - \prod_{i \in \text{Mis}_i \cap \text{Mis}_{i+1}} e^{-\frac{w_i}{N} \mathcal{J}_{ij} \sigma_i \sigma_j} \right) \\
(N - X_{\text{mis}})^3 \lambda_{\text{mis}} e^{-\lambda_{\text{mis}} X_{\text{mis}} + \ln(N_{\text{mis}})} &< \prod_{i \in \text{Mis}_i \cap \text{Mis}_{i+1}} e^{-\frac{w_i}{N} \mathcal{J}_{ij} \sigma_i \sigma_j}.
\end{aligned}$$

One future direction of interest is to further explore connections between the measure and solutions from the exit time formalism.

4 References

- [1] Allison, D. & Wang, G. R-loops: formation, function, and relevance to cell stress. *Cell Stress* **3**(2) (2019).
- [2] Bal, G. & Chou, T. On the reconstruction of diffusions from first-exit time distributions. *Inverse Problems* **20**(4) (2004).
- [3] Bintu, L., Buchler, N. E., Garcia, H. G., Gerland, U., Hwa, T., Kondev, J., Kuhlman, T., & Phillips, R. Transcriptional regulation by the numbers: applications. *Current opinion in genetics & development*, **15**(2), 125–135 (2015).
- [4] Borys, P. & Grzywna, Z. The Fokker-Planck Equation for Chaotic Maps. *Acta Physica Polonica B* **37**(2) (2006).
- [5] Brewster, R., Weinert, F., Garcia, H., Song, D., Rydenfelt, M. & Phillips, R. The Transcription Factor Titration Effect Dictates Level of Gene Expression. *Cell* **6**, 1312–1323 (2014).
- [6] Chen, J., Dagdas, Y., Kleinstiver, B., Welch, M., Sousa, A., Harrington, L., Sternberg, S., Joung, J., Yildiz, A. & Doudna, J. Enhanced proofreading governs CRISPR-Cas9 targeting accuracy. *Nature*, **550**, 407–410 (2017).
- [7] Chen, B., Gilbert, L., et al. Dynamic Imaging of Genomic Loci in Living Human Cells by an Optimized CRISPR/Cas System. *Cell*, **155**(7) 1479–1491 (2013).
- [8] Chou, T. & D’Orsogna, M. First Passage Problems in Biology. *Arxiv* (2014).
- [9] D’Orsogna, M., Lakatos, G. & Chou, T. Stochastic self-assembly of incommensurate clusters. *J Chem Phys* **136**(8) (2012).
- [10] Eitzinger, S., Asif, A., Watters, K. E., Iavarone, A. T., Knott, G. J., Doudna, J. A., & Minhas, F. Machine learning predicts new anti-CRISPR proteins. *Nucleic acids research*, **48**(9), 4698–4708 (2020).

- [11] Esvelt, K. M., Mali, P., Braff, J. L., Moosburner, M., Yaung, S. J., & Church, G. M. Orthogonal Cas9 proteins for RNA-guided gene regulation and editing. *Nature methods*, **10**(11), 1116–1121 (2013).
- [12] Eslami-Mossallam, B., Klein, M., Smagt, C., Sanden, K., Jones Jr, S., Hawkins, J., A kinetic model improves off-target predictions and reveals the physical basis of SpCas9 fidelity. *Preprint*.
- [13] Garneau, J. et al. the CRISPR/Cas bacterial immune system cleaves bacteriophage and plasmid DNA. *Nature* **468** 67–71 (2010).
- [14] Horlbeck, M. A., Witkowsky, L. B., Guglielmi, B., Replogle, J. M., Gilbert, L. A., Villalta, J. E., Torigoe, S. E., Tjian, R., & Weissman, J. S. Nucleosomes impede Cas9 access to DNA in vivo and in vitro. *eLife*, **5**, e12677 (2016).
- [15] Hultquist, J. F., Hiatt, J., Schumann, K., McGregor, M. J., Roth, T. L., Haas, P., Doudna, J. A., Marson, A., & Krogan, N. J. CRISPR-Cas9 genome engineering of primary CD4+ T cells for the interrogation of HIV-host factor interactions. *Nature protocols*, **14**(1), 1–27 (2019).
- [16] Jackson, S., Suma, A. & Micheletti, C. How to fold intricately: using theory and experiments to unravel the properties of knotted proteins. *Current Opinion in Structural Biology* **42**, 6–14 (2017).
- [17] Jeon, Y. et al. Direct observation of DNA target searching and cleavage by CRISPR-Cas12a. *Nature Communications*, **9**, 2777 (2018).
- [18] Keener, J. Mathematical Biology Course Lecture Notes.
- [19] Kim, B., Kim, H. & Lee, S. Regulation of Microbial Metabolic Rates Using CRISPR Interference with Expanded PAM Sequences. *Frontiers in Microbiology* **11**(282), (2020).
- [20] Kinney, J., Tkacik, G. & Callan, G. Precise physical models of protein-DNA interaction from high-throughput data. *PNAS*, **104**(2), 501–506 (2007).
- [21] Krapivsky, P., Redner, S. & Ben-Naim, E. A Kinetic View of Statistical Physics. *Cambridge University Press* 978-0-521-85103-9 (2010).
- [22] Mallamace, F. et al. Energy landscape in protein folding and unfolding. *PNAS*, **113**(12), 3159–3163 (2016).
- [23] Mekler, V., Minakhin, L., Semenova, E., Kuznedelov, K., & Severinov, K. Kinetics of the CRISPR-Cas9 effector complex assembly and the role of 3'-terminal segment of guide RNA. *Nucleic acids research*, **44**(6), 2837–2845 (2016).
- [24] Mirny, L. & Shakhnovich, E. Protein Folding Theory: From Lattice to All-Atom Models. *Annual Reviews Biophysics*, **30** 261–96 (2001).
- [25] Morra, G., Genoni, A. & Colombo, G. Protein Dynamics and Drug Design: The Role of Molecular Simulations. *Protein-Protein Complexes*, 340–385 (2010).
- [26] Peled, R. Topics in Statistical Physics and Probability Theory. *Lecture Notes*.
- [27] Ran, F., Hsu, P., Wright, J. Agarwala, V., Scott, D. & Zhang, F. Genome engineering using the CRISPR-Cas9 system. *Nature Protocols* **8** 2281–2308 (2013).
- [28] Satori, P. & Leibler, S. Lessons from equilibrium statistical physics regarding the assembly of protein complexes. *PNAS* **117**(1) 114–120 (2020).
- [29] Spcht, D., Xu, Y. & Lambert, G. Massively parallel CRISPRi assays reveal concealed thermodynamic determinants of dCas12a binding. *PNAS* **117**(21) 11274–11282 (2020).
- [30] Slutsky, M. & Mirny, L. Kinetics of Protein-DNA Interaction: Facilitated Target Location in Sequence-Dependent Potential. *Biophysical Journal*, **87** 4021–4035 (2004).
- [31] Stella, S. et al. Conformational Activation Promotes CRISPR-Cas12a Catalysis and Resetting of the Endonuclease Activity. *Cell* **175** 1856–1871 (2018).
- [32] Sternberg, S. H., Redding, S., Jinek, M., Greene, E. C., & Doudna, J. A. DNA interrogation by the CRISPR RNA-guided endonuclease Cas9. *Nature* **507**(7490), 62–67 (2014).

- [33] Tkacik, G., Callan, C. & Bialek, W. Information flow and optimization in transcriptional regulation. *PNAS*, **105**(34), 12265-12270 (2008).
- [34] Wolf, S., Lickert, B., Bray, S. & Stock, G. Multisecond ligand dissociation dynamics from atomistic simulations. *Nature Communications*, **11**, 2918 (2020).
- [35] Xu, X., Duan, D. & Chen, S. CRISPR-Cas9 cleavage efficiency correlates strongly with target-sgRNA folding stability: from physical mechanism to off-target assessment. *Sci Rep* **7**, 143 (2017).

Modeling exponential decay in maximum capacitance across specified flight patterns in small aircraft

Pete B. Rigas¹, and Chetan S. Kulkarni²,

¹ Cornell University, Ithaca, NY, 14850, USA
pbr43@cornell.edu

² KBR, Inc., NASA Ames Research Center, Moffett Field, CA, 94035, USA
chetan.s.kulkarni@nasa.gov

ABSTRACT

With increased autonomy being an integral part of unmanned aerial system (UAS), during flight a vehicle needs to have an accurate estimation of its state of health and capabilities to perform and achieve mission success with utmost safety. Batteries are of key importance in electric-propulsion aircraft and are its most pertinent resource. It is important to know the state of charge of the battery not only because the health state is directly related to the flight profiles flown by the vehicle, but also because the state of charge of the vehicle and its operational condition must be estimated after each flight.

In this work a methodology is presented to generate predictions for flight plans that experience anomalies, or unexpected system failure in due to a parasitic load in a specified stage of the flight that must return to its starting point of origin. We begin by describing the procedures by which a sequence of steps will be carried out to exponentially weigh the impact of different stages of a flight towards thermal strain on the capacitance C_{\max} of the battery during each flight.

1. INTRODUCTION

Drawing from a previous 2014 work (Hogge & et. al, 2014) in which the authors sought to improve methods of generating flight predictions for small aircraft, the methodology and approach that follows will generate flights predictions of a similar type, namely for flights with individual stages of specified duration, so as to improve the maintenance of batteries and other equipment that are involved in the aircraft. Moreover, to avoid having to perform laboratory tests on batteries after a fixed

Pete Rigas et al. This is an open-access article distributed under the terms of the Creative Commons Attribution 3.0 United States License, which permits unrestricted use, distribution, and reproduction in any medium, provided the original author and source are credited.

number of flights within a cycle, the framework heavily relies on a free parameter choice to model the expected decay in battery capacity.

In contrast to the remaining flight time estimates that are put forth in (Hogge & et. al, 2014), the approach is also aimed towards quantifying the exponential decay in the maximum capacitance due to a parasitic load that is inserted within a fixed stage of the flight, which can be imposed for the remaining duration of the flight. To categorically separate and study the rate of change of exponential decay of the maximum capacitance of different batteries, parasitic loads of exponential, or of polynomial, magnitude are computed for choices of β parameters. From the percentage of the maximum capacitance that the battery is observed to hold after a given cycle, the exponential factor is temporally weighed in the duration of all stages of the flight. As a result, introducing this factor allows for a broader prognostics reflection not only pertaining to equipment maintenance but also to the total duration of a flight and the accompanying SOC before a failure occurs. Other works, including (Goebel & Eklund, 2007),(Kulkarni et al., 2010),(Kulkarni et al., 2011),(Sankararaman & Goebel, 2013a),(Sankararaman & Goebel, 2013b),(Saha, Saha, & Goebel, 2009) offer detailed discussions of either the experimental set up of tests which were used to test the accuracy of different numerical models, in addition to the architectural schemes of offline battery maintenance, insofar as to further study capacity degradation due to aging.

With example upper and lower bounds on the maximum capacity decay for a variety of flights from different batteries in the publicly available HIRF repository (Kulkarni et al., 2015), we are interested in building upon previous studies to further study the capacitance degradation. The publicly available data set contains HIRF tests and experimental data conducted on an electric fixed wind UAV Edge 540. The e-UAV is a 33% sub-

scale version of the Zivko Aeronautics Inc. Edge 540 T tandem seat aerobatic aircraft. This vehicle has been actively used to facilitate the rapid deployment and evaluation of remaining flying time prediction algorithms for electric aircraft(Hogge & et. al, 2014).

The parameter choice and resulting numerical behavior provides a formalism through which experiments consisting of flights with either longer duration, more complicated pattern with more stages in the flight, or varying magnitude of electromagnetic radiation in the ambient environment, can be accounted for through adjustment of the free parameters.

To characterize different flight plans from which sets of predictions will be generated, the approach detailed below provides approximations of the time duration of each segment of a flight, depending on the magnitude of the current exerted by the engine over each time interval. To readily generate valuable prognostics predictions, we introduce an exponentially decaying factor whose magnitude is numerically determined by enforcing choices of parameters $\{\beta_i\}$ which multiply the approximate duration of each time interval of the flight. Finally, with a smooth polynomial approximation to the flight data, we compute the Fourier coefficients and series of current versus time plots of a given flight, to generate predictions for upcoming flight plans. From batteries of a given type, the magnitude of the exponential factor will be leveraged to model the decay in the maximum capacitance of the battery across multiple flights.

2. GENERAL APPROACH

In this section an overview of the developed approach is discussed. The Fourier series representation of each flight plan is obtained by approximating the temporal duration of each segment of an arbitrary flight plan through each stage of the flight, which includes imposing a coordinate axis to measure applicable sine or cosine modes of the Fourier series representation which will be enforced after coefficients corresponding to each stage of the flight have been determined.

Next, we compute a sufficient number of Fourier coefficients so that the corresponding series representation of the flight plan sufficiently represents current measurements for each point in time of the flight plane, which is obtained through a trigonometric basis $\{\sin(\frac{n\omega_0 t}{T}), \cos(\frac{n\omega_0 t}{T})\}_{n \in \mathbb{N}}$, where a normalizing factor T is introduced.

For one example flight, we determine a threshold of the Fourier modes N for which the mean squared error, of the form $\sum_n a_n^2 + b_n^2$, or equivalently $\sum_n a_n^2$ or $\sum_n b_n^2$, is determined. Across numerical experiments in which up to 20,000 Fourier modes are computed, we conclude

that the approach is computationally accessible because a MSE of magnitude ≈ 0.192 demonstrates that the methodology is capable of generating reliable predictions for varying flight profiles without having to include hundreds of Fourier modes (in particular, no more than 20 from the worked example in Section 4.2) in the series expansion. From either a Fourier cosine or sine series, informative and reliable predictions can be generated by determining the final time stamp up to which the polynomial approximation of flight data will be enforced.

Next, given such a Fourier series representation of the flight, the exponentially decaying factor for computing the change in the maximum and minimum capacitance will be defined. In turn, the approach will generate predictions for flights plans of the following types, all of which are dependent on the duration of the specific stage of the flight as well as the time stamp throughout the stage of the flight at which the plan is terminated. It is important to emphasize that the time stamp at which the flight will be terminated is arbitrary and will therefore impact the corresponding number of Fourier modes and MSE that can be computed. In what follows, we will distinguish between different flight plans, depending on the number of stages in a flight, at which the flight can be arbitrarily terminated.

Flight Plan Type A: Given a set of experimental trials, we will demonstrate how to compute an accompanying rate of exponential decay in the maximum capacitance over successive flights that is proportional to the magnitude, and duration, of the thermal stress in addition to the mechanical work that is applied to the engine for each stage of the flight. From this factor, predictions will be readily generated for flights that are terminated in the first stage of the flight by computing the exponential decay of the maximum capacitance C_{\max} . In addition to examining the sharpness of decay in C_{\max} , our methodology is also capable of accommodating different series expansions, namely expressions with a different number of Fourier modes N that can be used to accommodate predictions for different time stamps throughout some fixed stage of the flight. Within a given stage of the flight, the smooth polynomial approximation of flight data is capable of generating distinct Fourier series expansions, each of which correspond to flight plans in which the rightmost endpoint in time is continuously varied. With variable time stamps at which the flight is terminated, the polynomial root finding method generates smooth approximations from experimental current versus time plots.

Flight Plan Type B: Given a set of experimental trials, predictions for more complicated flight patterns can be generated by making use of the predictions generated for flights of the previously defined type, in the sense that

a flight pattern of Type B can be analyzed, from predictions of flights of Type A by implementing the following. First, it is imperative that we include a prescribed number Fourier modes \mathcal{N} in the series expansion for the beginning phase of the flight during which current flows through the circuit. In this initial stage, predictions of the termination of the flight plan in the next stage of the flight, hence the name Flight Plans of Type B, can be generated by implementing the change in maximum capacitance from the previous flight plan. From the free parameters β_i that we have injected into the power of the exponent to measure the decay in C_{\max} , we can also generate sets of inequalities to capture the minimum and maximum rates of exponential decay in C_{\max} , granted that the smooth polynomial approximation not violate the condition that $|R(t_i) - f(t_i)| < \epsilon$ for all times t_i preceding the unforeseen abortion of the flight in its earlier stage. In this inequality, the precision that we demand between the smooth polynomial approximation of the flight plan data and the current measurements holds for arbitrary ϵ , where the quantity R denotes the experimentally gathered flight plane for all time stamps t_i in the flight, and the quantity f denotes the smooth polynomial approximation of the current measurements. When running the polynomial root finding algorithm, we enforce that a maximum discrepancy ϵ between the experimental data, and approximations of the data, is satisfied across all t_i .

Flight Plans Types C,D,E: Repeating the same observations and formulations for flight plants of Type A and Type B mutatis mutandis gives immediate generalizations of other flight plans for which the unforeseen abortion of the flight can occur. In particular, flight plans of Types C, D and E, respectively, describe excursions over which the same maximum capacitance value (which is the C_{\max} value computed from previous flights in a given sequence, determined from an initial capacitance value in the first flight of the sequence which we set to be at a 100% threshold), the final time stamp t_f are which the flight is terminated.

Flight Plan Type X: Pursuant of further generalizations, the preceding observations and formalism can be applied mutatis mutandis to new flights patterns, of emerging interest, for an arbitrary but countable number of intervals over which a flight can be terminated.

The authors suggest that generalizing the approach to new experiments with small aircraft of varying construction and battery types is worthwhile. The publicaly available dataset from NASA includes collections of current time measurements, which can be modeled with the following approach by roughly determining the duration of each period of the flight, from which additional flight tra-

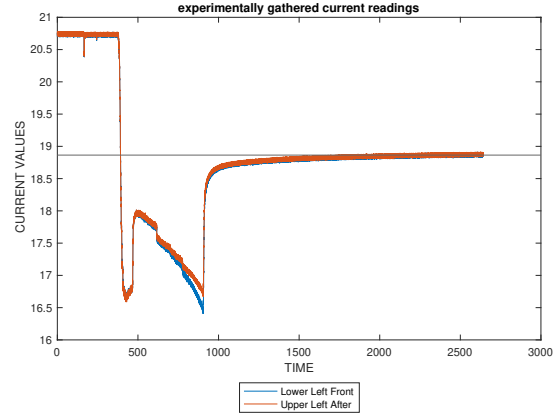


Figure 1. Example of Set 6, HIRF 77, plot of horizontal line for flight plan of Case 1

jectories rather than those carried out by experiment can be simulated with varying free parameter choices.

3. IMPLEMENTATION

To test the Fourier series implementation and exponentially decaying capacitance factor in flight plans, we implement the approach in a set of training data through a given sequence of flights by executing the following.

We run an auxiliary algorithm in Matlab which returns the approximate time intervals, and respective duration, of each stage of a given flight. Systematically, we deal with the following cases.

Case 1: (Flight plans in which the current reading at the final stage of the flight vertically asymptotes to a current measurement higher than that of preceding stages of the flight) For flight plans of Case 1, one can easily generate time intervals for intermediate stages of the flight plan by extending a horizontal line past the stage of the flight, and then linearly searching below a determined threshold to obtain isolated segments of the flight during which polynomial approximations from the root finding method can be obtained. From the current value that is exerted near the end of the flight from which the horizontal line is extended, a threshold δ will be chosen so that all current values below those of $\mathcal{H} - \delta$ are returned.

Case 2: (Flight plans in which the final current reading for the last stage of the flight vertically asymptotes to a value that is lower than that of the preceding stage of the flight) For flight plans of Case 2, one can generate analogous results corresponding to the time intervals for disjoint segments of a given flight plan. For Case 2, we instead linearly search above the current value that the data asymptotically approaches at the final time

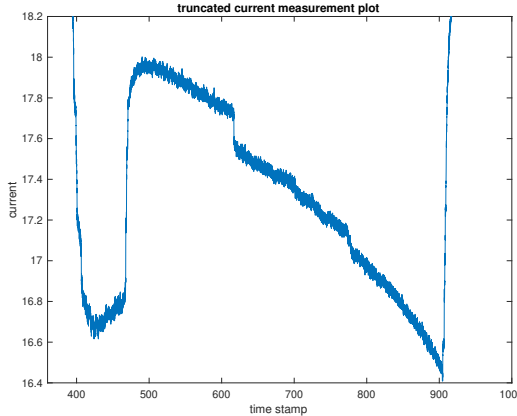


Figure 2. Plot of individual stages of the flight which are determined by linear inspection of the data through a specified threshold δ of the current asymptotic value given by the horizontal line at the end of the flight, with $\delta = -0.5$.

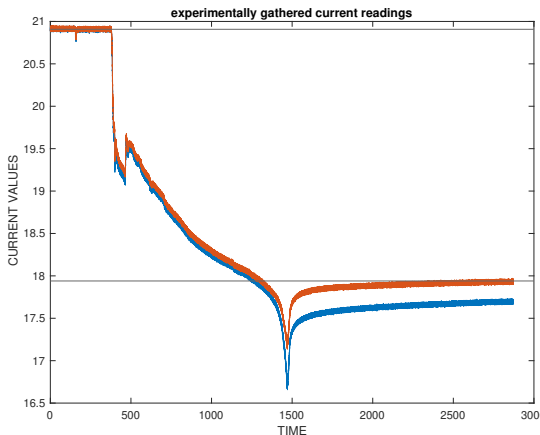


Figure 3. Example of Set 6, HIRF 80, plot of two horizontal lines for flight plans falling under Case 2

stamp of the given flight, while simultaneously conditioning that the search enforce that the isolated segments of the flight not exceed the initial current starting value in the initial stages of the flight. After executing such a search, the auxiliary algorithm similarly returns a set of times for each stage of the flight.

With the time duration of each stage, the resulting values inform the magnitude of an exponentially decaying factor which measures the change in C_{\max} value across subsequent flights. This temporally weighed factor is of central importance for the methodology because the exponential factor informs the sharpness of capacitance decay which is inversely proportional to the total flight time. From the flight examples above, we observe the following.

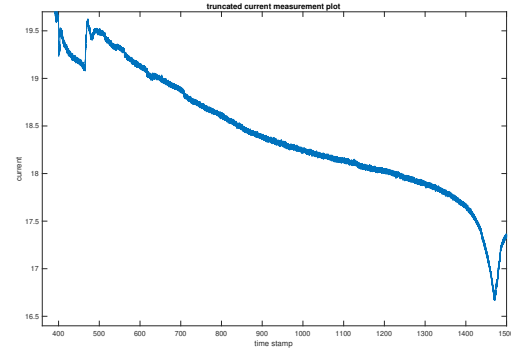


Figure 4. Plot of individual stages of the flight which are determined by linear inspection of the data through a specified threshold δ' of the current asymptotic value given by the horizontal line at the end of the flight, with $\delta = 1.5$.

Case	Parameters	C_{\max} on flight 2
1	$\beta_1 = \frac{1}{500}, \beta_2 = \frac{1}{5000}$	$\approx 0.73184C_1$
2	$\beta_1 = \frac{1}{100}, \beta_2 = \frac{1}{5000}$	$\approx 0.43509C_1$
3	$\beta_1 = \frac{1}{2500} = \beta_2$	$\approx 0.67686C_1$
4	$\beta_1 = \frac{1}{25000} = \beta_2$	$\approx 0.99610C_1$

Table 1. Table providing choice of parameters for each of the 4 cases in Figure 5

From Set 6, HIRF 77, disregarding the middle portion of the flight during which the magnitude of the loading current is approximately constant, one may compute the exponential decay in C_{\max} by enforcing choice of free β_i . In this specific instance, the choice of free parameters correspond to the real numbers that are linearly weighed in the temporal duration of all segments of the flight. Upon drawing inspiration from exponential solutions to the one dimensional separable differential equation, we expect that comparing the temporal duration of different stages of a flight, from the example in Set 6, HIRF 77 above, yields an exponential decay C_{\max} that would further reduce the change in capacitance in the second flight. It is natural to expect that the rate of capacitance decay will decay more sharply if there are more time stamps in a given stage of the flight, in which $C_{\max_1}^{1 \rightarrow 2} \geq C_{\max_2}^{1 \rightarrow 2} \Leftrightarrow |T_{6,77}^1| = |\{t_i \in T_{6,77}^1\}| \leq |T_{6,77}^2| = |\{t_j \in T_{6,77}^2\}|$. The ordered pair (C_{\max_2}, T^2) denotes the capacitance and stage duration, respectively, of the stage $T_{6,77}^1$ of an arbitrary flight plan.

On the other hand, from Set 6, HIRF 80, the return values of the auxiliary algorithm permit calculations of the exponential decay in C_{\max} for flights of Case 2. From noticeable differences in the trajectory of the flight from

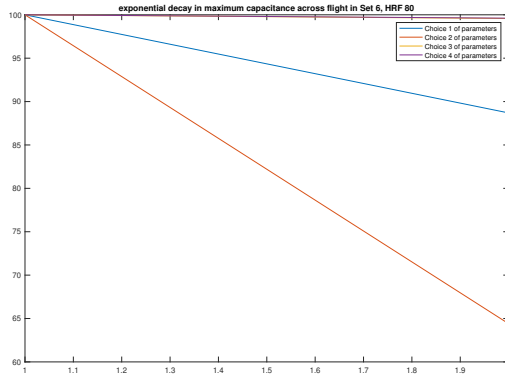


Figure 5. From the two demarcated stages of the flight given the return values of the auxiliary algorithm, the exponential decay in C_{max} is exhibited across each stage of the flight. A clear dependence between the reported C_{max} and β_i is exhibited.

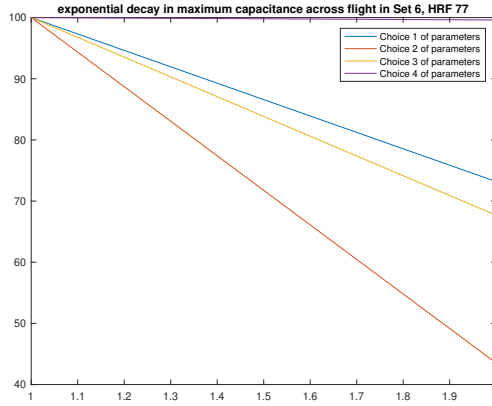


Figure 6. From the two demarcated stages of the flight given the return values of the auxiliary algorithm, the exponential decay in C_{max} is shown across the first stage of the flight.

Set 6, the exponential decay in C_{max} is more sharp across the sequence of flights in comparison to that of HIRF 80.

Finally, to establish sets of predictions for flight of varying types, namely flights of the previously defined types, a Fourier series expansion will be introduced by computing the Fourier coefficients from the polynomial approximation.

3.1. Exponentially decaying capacitance

With the different choices of β parameters that will be further expounded upon in more sensitive calculations of the exponential decay in C_{max} that are inclusive of the beginning and ending periods of the flight, we will make the choice of free β parameters so that the decay of the maximum capacitance between neighboring flights

Case	Parameters	C_{max} after flight 2
1	$\beta_1 = \frac{1}{1000}, \beta_2 = \frac{1}{5000}$	$\approx 0.88692C_1$
2	$\beta_1 = \frac{1}{200}, \beta_2 = \frac{1}{5000}$	$\approx 0.644036C_1$
3	$\beta_1 = \frac{1}{300000}, \beta_2 = \frac{1}{50000}$	$\approx 0.995742C_1$
4	$\beta_1 = \frac{1}{300} = \beta_2$	$\approx 0.99610C_1$

Table 2. Table providing choice of parameters for each of the 4 cases in Figure 7.

reflects a rate of decay in the capacitance that is appropriate, in the sense that the rate of exponential decay does not fall into any one of the cases above in which the maximum capacitance in one flight from a previous one is almost left unchanged, at or around 99% of the previous C_{max} , or at around 50% of the C_{max} for a typical flight.

4. WORKFLOW

Before proceeding with our formalism to define quantities that are of computational value to help with generating flight predictions, the items below provides a high level summary of each step in the approach.

1. The auxiliary algorithm uses flight plan data as input, which returns the approximate time intervals of each stage of the flight, depending on the magnitude of the current at the beginning and ending stages of the flight.
2. We enforce choices of free $\{\beta_i\}_{i \in \mathbb{N}}$ for calculating the exponential decay of C_{max} .
3. With lower and upper bounds on such a decay rate, polynomials are introduced to smoothly approximate chamber data for current measurements in the aircraft engine, from which estimates of each stage of the flight are generated.
4. To approximate flight plan data with a Fourier series, smooth polynomial approximation is used on the flight data obtained in the previous step, as we compute the sine and cosine coefficients of the Fourier series expansion.
5. As a result, sets of predictions for future flights are generated, within the combinatorial space of distinct outcomes, by computing the range of Fourier modes that can be used in the series to approximate the flight plan data. With the Fourier coefficients of our expansion, we can also determine corresponding MSE values. From numerical experiments on data from the NASA prognostics repository, we are interested in determining whether there is a critical value of the Fourier modes, \mathcal{F}_{crit} , beyond which increasing the number of Fourier modes in the series expand-

sion does not yield a lower MSE. Qualitatively, we attribute a lower MSE to a higher confidence in the set of predictions for a flight on which the algorithm is ran, while we attribute a higher MSE to a lower confidence in the set of predictions.

6. Within the space of outcomes, we will introduce numerical bounds, based on the 30% SOC threshold cutoff, at which a flight can safely operate for a specified duration of time.

4.1. Fourier series approach

With a polynomial approximation obtained via the root finding method, given an arbitrary number of time stamps before the flight plan is to be terminated, a modification to the usual Fourier sine and cosine coefficients will be introduced with each of the coefficients taking the form

$$a_n = \frac{1}{\sum_i t_i} \int_{\mathcal{T}_i} f(t) \cos\left(\frac{n\omega_0 t}{\mathcal{T}_i}\right) dt, \quad (1)$$

and

$$b_n = \frac{1}{\sum_i t_i} \int_{\mathcal{T}_i} f(t) \sin\left(\frac{n\omega_0 t}{\mathcal{T}_i}\right) dt, \quad (2)$$

where \mathcal{T} denotes the stage of the flight over which the polynomial approximation is obtained, and the normalizing constant for the period in the Fourier coefficients is the summation over all time stamps of the particular stage of the flight. As expected, f is smooth and from these expressions, one can obtain a series expansion of the form

$$F(x) = \frac{a_0}{2} + \sum_{n,t \in \mathcal{T}_i} a_n \cos\left(\frac{n\omega_0 t}{\mathcal{T}_i}\right) + b_n \sin\left(\frac{n\omega_0 t}{\mathcal{T}_i}\right), \quad (3)$$

where each period \mathcal{T}_i is not only dependent on the duration of the time interval of the stage of the flight, but also on the current of the magnitude \mathcal{I} exerted on the engine given a trajectory. With such a Fourier series that one can obtain from the aforementioned trigonometric basis, introduced over each respective \mathcal{T}_i , flight predictions for plans of type A can be generated for arbitrary time stamps t_j before the initial stage of the flight by first introducing a polynomial approximation of the flight data up to t_j , from which the MSE of all modes included in the expansion, $\sum_n a_n^2 + b_n^2$, is computed. Up to the stage of interest, we make use of the truncated Fourier series,

$$F_{\mathcal{T}_i, t_i} = \frac{a_0}{2} + \sum_{n=1}^{\mathcal{M}_{t_i}} a_n \cos\left(\frac{n\omega_0 t}{\mathcal{T}_i}\right) + b_n \sin\left(\frac{n\omega_0 t}{\mathcal{T}_i}\right), \quad (4)$$

for a sufficient number of modes $\mathcal{M}_{t_i} < \mathcal{N}$. With a series approximation $F_{\mathcal{T}_i, t_i}$ above denoting the series truncation corresponding to the maximum time stamp $t_i < t_j$ for which the 30% SOC threshold can be maintained when the flight is terminated at the later time t_j , for all $t \in \mathcal{T}_i$.

To ensure that such a truncation adequately captures the degradation in C_{\max} across successive trials, or potentially across trials with a battery of any type, an exponentially decaying, temporally dependent factor, factor is defined across all time stamps $t_i, t_j \in \mathcal{T}_i$, and $t'_i, t'_j \in \mathcal{T}_j$. Free parameters β_1, β_2 , as demonstrated in plots for different decay rates of C_{\max} , which multiplicatively accompany the time intervals $[t_i, t_f]$ and $[t'_i, t'_f]$, over \mathcal{T}_i and \mathcal{T}_j , respectively, during which a current of varying magnitude \mathcal{I} is exerted. More generally, the power of the exponent is of the form $\sum_i \beta_i |\mathcal{T}_i|$, with the summation taken over all stages of the flight.

For distinct time periods of each stage, the rates of exponential decay in C_{\max} , in addition to the series representation, provide flight predictions by computing the rate of exponential decay in the C_{\max} across multiple flights with specified duration from the periods $\mathcal{T}_1^1, \dots, \mathcal{T}_n^1, \dots, \mathcal{T}_N^1, \dots, \mathcal{T}_N^n$. Incorporating the exponential decay mentioned in the previous step to determine the maximum duration's of time for which the flight can maintain the 30% threshold, can be obtained by making use of the formula

$$\text{SOC} = 1 - \frac{q_{\max} - q_b}{C_{\max}}, \quad (5)$$

provided for computing the threshold in [2]. With the previous exponential factor, it is also possible to determine the range of admissible Fourier modes in the series representation and to compute the MSE associated with the series approximation.

4.2. Computation Case Studies

With a substantial array of Fourier coefficients, ranging from 200, 2, 000 to 10, 000 modes, all of which together constitute a run time of approximately 3 days, numerical simulations were executed to determine properties relat-

Fourier modes	Max	Min
200	≈ 0.40793	$\approx 2.7658 \times 10^{-6}$
2,000	≈ 0.40793	$\approx 2.7049 \times 10^{-8}$
10,000	≈ 0.40793	$\approx 1.0955 \times 10^{-3}$

Table 3. Fourier cosine coefficients

Fourier modes	Max	Min
200	$\approx -8.6023 \times 10^{-4}$	≈ -21.1558
2,000	$\approx -8.6023 \times 10^{-5}$	≈ -21.1558
10,000	$\approx -1.7205 \times 10^{-5}$	≈ -21.1558

Table 4. Fourier sine coefficients

ing to the convergence of Fourier series, which is valuable for determining the critical number $\mathcal{F}_{\text{crit}}$. By introducing a series approximation to the end of the first stage of this flight up to $t_f = 450$, the numerical experiments demonstrate that we do not have to resort to a high number of Fourier modes in order to reach a sufficiently low MSE. This demonstrates that utility of the approach in being able to readily generate predictions that are computationally accessible.

Beyond observed numerical results, the plots below exhibit the distribution of higher frequency terms that could be used in the Fourier series expansion, where the computations of the Fourier coefficients are carried out for 10,000 Fourier sine and cosine coefficients. Due to the significantly higher MSE associated with the Fourier sine coefficients for this example flight, we have only made use of the cosine coefficients in the series expansion to approximate the flight data, from which the series expansion is plotted for all 4938 time stamps of the flight.

4.3. Adjusting the free parameters in the exponentially decaying factor

From the description and implementation of the auxiliary algorithm as a proxy for the change in C_{\max} across a flight, from a fixed ordering of the time stamps and current measurements, the image of time intervals under the

Fourier modes	Max.	Min.
200	≈ 0.3139	$\approx 7.928 \times 10^{-6}$
2,000	≈ 0.3139	$\approx 7.857 \times 10^{-8}$

Table 6. Fourier cosine coefficients

Fourier modes	Max.	Max.
200	≈ 21.124	$\approx 2.466 \times 10^{-3}$
2,000	≈ 21.236	$\approx 2.466 \times 10^{-4}$

Table 7. Fourier sine coefficients

assignment $\Phi : \mathbf{R}^+ \longrightarrow \mathbf{R}^+ : |t_j - t_k| \mapsto \beta_i$, for $j \neq k$, and $\beta_i > 0$, produces a monotonic pairing of the time intervals of each stage of the flight with the freely chosen β_i so that, throughout the variable duration of a given flight pattern, periods of shorter duration over which the magnitude of the current \mathcal{I} abruptly changes are multiplicatively weighed unfavorably in their negative impact on the ability of the circuit to transport charge in the engine, while periods of longer duration over which the current of magnitude \mathcal{I} changes more gradually over the course of a stage in the flight, are multiplicatively weighed favorably in terms of continuing to preserve the ability of the circuit to maintain the maximum capacitance which in turn less adversely impacts the circuit.

With such a convention of the free parameter assignment, a range of exponentially decaying factors, allows for predictions to be realized. Through the experiment with the arrays of Fourier coefficients that have been generated, the same approach can be applied to flight patterns for which the time intervals of each stage are collected, from which the temporally adjusted weighted exponential decrease of the circuit can be computed which is dependent on the magnitude of the current exerted during stages of the flight. Such data sets are publicly available from the NASA prognostics repository 15.

Fourier modes	MSE
200	≈ 560.79416
2,000	≈ 561.902567337
10,000	≈ 5.62001093

Table 8. MSE values

Fourier modes	MSE
200	$\approx 0.192276077317043$
10,000	$\approx 0.192276132208228$

Table 5. MSE values

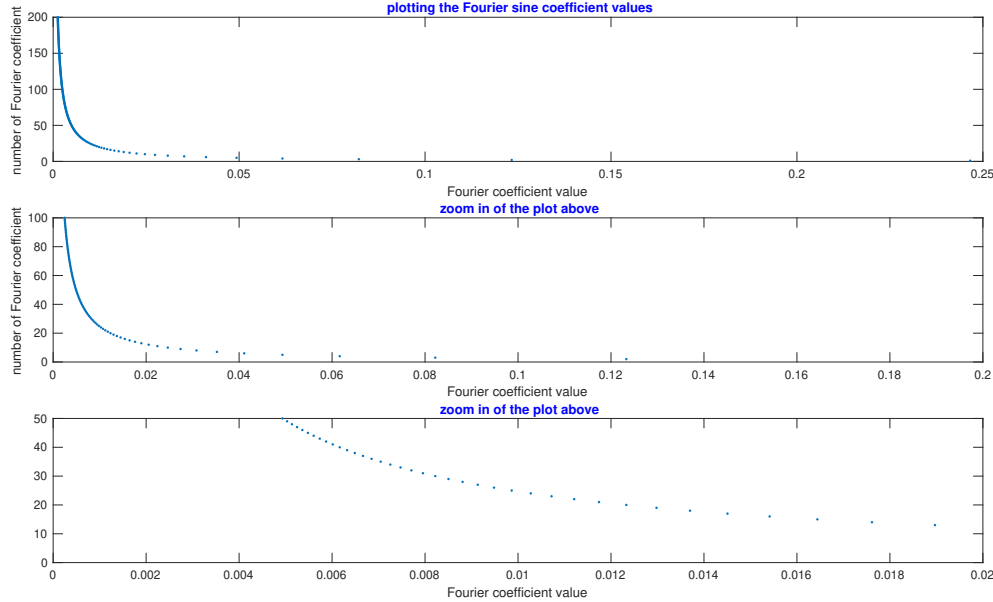


Figure 7. In contrast to similar plots of the Fourier cosine coefficients, the sine coefficients, for the truncated polynomial approximation up to the time stamp 450 before the current change occurs results in coefficients that are of opposite sine than those previously presented in the previous diagram.

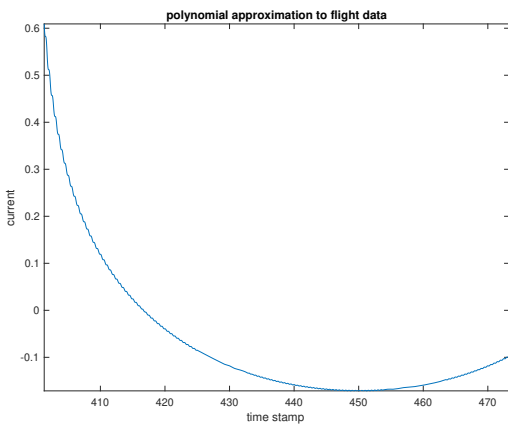


Figure 8. To more closely analyze the behavior of the series approximation from which predictions will be generated with a corresponding MSE, the behavior of the series approximation, as t varies, is depicted above.

5. PROCEDURE FOR GENERATING THE COMBINATORIAL SPACE OF FLIGHT PREDICTIONS

To produce effective and informative flight predictions given a numerically specified exponential rate of decay in C_{\max} , we proceed with the following.

Step 1 (identifying the stage of the flight during which the prediction is to be established): To systematically address all stages and times during which an anomaly

could occur, we introduce arbitrary time stamps $t_{\text{abort}}^{(i)}$ corresponding to each stamp $T^{(i)}$ of a given flight. From such time stamps in future flight plans that we attribute to anomalies, predictions for the flight in question will be generated by linearly varying the stamp $t_{\text{abort}}^{(i)}$ with respect to time for all admissible stamps in the stage $\mathcal{T}^{(i)}$ of the flight. From such a collection of times, we proceed to incorporate the minimum and maximum rates of exponential decay in C_{\max} of the circuit, by means of introducing a suitable free parameters β_i in the exponentially decaying factor, insofar as to not only simulate distinct rates of exponential decrease in C_{\max} , but also to account for flight plan anomalies in any possible stage. To determine whether a flight should be terminated, at arbitrary $t_{\text{SOC}}^{(i)} < t_{\text{abort}}^{(i)}$, we make use of the expression for the state of charge threshold given in [2].

Step 2 (computing informative ranges in the exponential decay of C_{\max}): In order to generate realistic predictions, we must also introduce upper and lower bounds for the decay of C_{\max} . Pursuant of this goal, we wish to measure the change in exponential decay that one can attribute to different choices of parameters β_j , denoted β'_j , satisfying $|\beta_j - \beta'_j| < \epsilon$ for arbitrarily small ϵ . Under these assumptions, the exponential factor for measuring the change in capacitance takes the form,

$$e^{\sum_{i \cap j} \beta_i \left(t_{\text{final}}^{(i)} - t_{\text{initial}}^{(i)} \right) + \beta_j \left(t_{\text{final}}^{(j)} - t_{\text{initial}}^{(j)} \right)} - e^{\sum_{i \cap j} \beta_i \left(t_{\text{final}}^{(i)} - t_{\text{initial}}^{(i)} \right) + \beta'_j \left(t_{\text{final}}^{(j)} - t_{\text{initial}}^{(j)} \right)},$$

where the arbitrary reals β_j, β'_j are chosen during the stage $T^{(j)}$ of the flight, which has time duration $t_{\text{final}}^{(j)} - t_{\text{initial}}^{(j)}$. Because all of the remaining β_i , for $i \neq j$ for all other stages of the flight are fixed, enforcing a different choice of the β_j parameter amounts to a multiplicative, exponentially decaying factor, of the form

$$e^{\sum_{i \cap j} \beta_i \left(t_{\text{final}}^{(i)} - t_{\text{initial}}^{(i)} \right)} \left(e^{\left(\beta_j - \beta'_j \right) \left(t_{\text{final}}^{(j)} - t_{\text{initial}}^{(j)} \right)} \right).$$

Additionally, to make even more explicit the dependence of the C_{\max} decay with respect to time, we designate the arbitrary time stamps $t_{\text{abort}}^{(i)}$ as the times during each stage $T^{(i)}$ during which the flight could be terminated. At each such time stamp in this stage, the choice of parameters will satisfy the SOC threshold that is provided in future arguments.

Step 3 (choosing flight data from the prognostics repository to compute exponential rates of decay in C_{\max} , from which bounds on the C_{\max} will be generated): From previous remarks concerning how the C_{\max} of the circuit would change across successive flights with choices of β_i for each flight stage, as a consequence it is important to designate the sets of experimental data from which exponential rates of decay in C_{\max} will be determined. In addition to enforcing a certain SOC threshold that the aircraft must satisfy while it is operational, predictions for future flights can be generated by determining appropriate choices of the β_i so that the model reliably captures the rate of C_{\max} as observed from experiments.

Step 4 (generalizing sets of predictions for flight plan abnormalities given a time stamp of flight termination): With upper and lower bounds for C_{\max} in hand from Step 3, generating flight predictions now amounts to implementing the variable time, to be specified between stages of a flight, during which an arbitrary flight plan could be aborted due to either flight plan abnormalities or mechanical failures. In particular, by choosing each possible stage of the future flight plans at which the

anomaly could occur, predictions are readily generated by searching for parameters that capture the rate of decay in the maximum capacitance.

In specific instances of different flight planes, the approach is capable of determining whether a small aircraft can land given unforeseen changes in the C_{\max} value of the circuit. With an additional exponentially decaying factor appended to the quantity has already been given and discussed, which takes the form

$$C_{\max_{i+1}}^{\text{PL}, T^{(i)}} = \left(e^{\sum_i -\beta_i |t_{\text{initial}}^{(i)} - t_{\text{final}}^{(i)}|} \times e^{\frac{\beta_{\text{PL}, T^{(i)}}}{\tau_{\text{PL}}} |t_{\text{final}}^{\text{PL}} - t_{\text{initial}}^{\text{PL}}|} \right) C_{\max_i}, \quad (6)$$

which denotes the local exponential decay of C_{\max} given a temporally dependent, exponentially increasing, parasitic load PL. Numerically, it is important to remark upon the nature of this exponential term, particularly in that the power of the exponential can be equal to, less than, or greater than in magnitude of the summation in the power of the first exponential which is dependent on both the β_i and duration of each stage $T^{(i)}$ of the flight. One may also define the decay of the local capacitance due to a polynomial factor, instead of an exponential one, taking the form

$$C_{\max_{i+1}}^{\text{PL}, T^{(i)}} = \left(e^{\sum_i -\beta_i |t_{\text{initial}}^{(i)} - t_{\text{final}}^{(i)}|} \times \left(1 + \left(\beta_{\text{PL}, T^{(i)}} |t_{\text{final}}^{\text{PL}} - t_{\text{initial}}^{\text{PL}}| \right) t_{\text{final}}^{\text{PL}} + \frac{\left(\beta_{\text{PL}, T^{(i)}} |t_{\text{final}}^{\text{PL}} - t_{\text{initial}}^{\text{PL}}| t_{\text{final}}^{\text{PL}} \right)^2}{2} + \dots \right) \right) C_{\max_i}, \quad (7)$$

for a parasitic load which polynomially increases with respect to time. The rate of decrease that this load poses on the C_{\max} value after consecutive flights is useful in being able to model different rates of decay in the circuit in stage $T^{(i)}$ of the flight.

Step 5 (SOC formulas based on maximum capacitance formalism for the regular and local cases): From expressions of C_{\max} and C^{PL} , we can make use of the formula for computing the SOC to propose 3 different formulas that can be used to compute the corresponding state of charge, each of which are of the form,

$$\text{SOC}_1 = 1 - \frac{q_{\max} - q_b}{e^{\sum_i -\beta_i \times t_{\text{initial}}^{(i)} - t_{\text{final}}^{(i)}} C_{\max}}, \quad (8)$$

$$\begin{aligned} \text{SOC}_2 &= 1 - (q_{\max} - q_b) / [e^{\sum_i -\beta_i |t_{\text{initial}}^{(i)} - t_{\text{final}}^{(i)}|} \\ &\quad \times e^{\frac{\beta_{\text{PL}, T^{(i)}}}{\tau_{\text{PL}}^{(i)}} |t_{\text{final}}^{PL} - t_{\text{initial}}^{PL}|} C_{\max}], \end{aligned} \quad (9)$$

$$\begin{aligned} \text{SOC}_3 &= 1 - (q_{\max} - q_b) / [1 + (\beta_{\text{PL}, T^{(i)}} \frac{|t_{\text{final}}^{PL} - t_{\text{initial}}^{PL}|}{\tau_{\text{PL}}^{(i)}}) t_{\text{final}}^{PL} \\ &\quad + \frac{1}{2} (\beta_{\text{PL}, T^{(i)}})^2 |t_{\text{final}}^{PL} - t_{\text{initial}}^{PL}| \\ &\quad t_{\text{final}}^{PL})^2 + \dots) C_{\max}], \end{aligned} \quad (10)$$

respectively, which together correspond to the SOC for the first formula for the capacitance introduced the earliest in the report, while the remaining 2 formulas below the first equation correspond to expressions for the SOC due to the local capacitance C of the parasitic load, with either exponential or polynomial rates of decay.

Step 6 (summarizing the procedure: backtracking from t_{abort} to determine time intervals for which the current satisfies 30% SOC): From either a flight or parasitically driven mechanical abnormality, we can make flight predictions by following previous steps, in which exponentially weighing the duration of each flight, which poses mechanical or thermal stress on the engine, provides convenient interpretations for the total duration of a flight before the circuit fails to satisfy a specified SOC threshold.

5.1. Rate of decay of the local capacitance due to a parasitic load

As suggested through computations in previous tables, we are able to readily generate predictions for upcoming flights by specifying the stage of the flight at which the load is imposed, from which computations of the local capacitance, due to either polynomial or exponential decay, can be computed. Thus, from such a rate of decay, it is possible to establish suggestions for the maximum flight time given the duration of each stage of the flight. Conversely, past flight data from previous mechanical malfunctions can also be interpreted, as follows. If the duration of either a mechanical malfunction or a flight anomaly is known, the magnitude of the parasitic load, whether polynomial or exponential, can be determined by working backwards from the expressions given in the previous section. Namely, if the distance over which the mechanical or flight plan anomaly is known through

experimentally gathered current measurements, then the distance over which the anomaly has occurred can be used to approximate the magnitude of the parasitic load responsible for the anomaly.

Furthermore, because an exponentially varying parasitic load that increases with respect to time can be Taylor expanded into a polynomial of fixed degree, computing the distance over which a flight anomaly have occurred may also be implemented to obtain a polynomial expression for the parasitic load that is responsible for the anomaly. In either circumstance, the approach fits within experimental data that is to be gathered in upcoming chamber experiments, or to data that has already been gathered, to inform maintenance of future flights. Clearly, if the magnitude due to the parasitic load is sufficiently dominant, in the sense that the degradation due to the parasitic load prevents the flight from completing individual stages of a flight that are of the same duration from flights that it has already completed previously in a given sequence, then the flight should be terminated.

6. CONCLUDING REMARKS

By introducing an exponentially decaying factor that is temporally weighed in specific sets of loading current versus time measurements that are experimentally recorded for flight patterns, we are able to generate widely accommodating flight predictions that take into account the specific nature of the data, which in this case consists of current drawn from the batteries supplied to the electric power-train throughout the flight, which is variable and can variably degrade with repeated use. In future work, we are continuing to pursue our interest of being able to continue generating sufficiently large combinatorial spaces from the Φ assignment. Although such a mapping is defined so that we do not assign multiple β free parameters to the C_{\max} decay for time periods of a flight that are not equal, there are countably many mappings that can be constructed to further experiment with the steepness of the C_{\max} decay. Varying the rate of the C_{\max} decay could be of additional interest for aircraft that are either built according to different specifications than the one in which HIRF chamber experiments were held. The developed methodology and the approach presented here is capable of addressing such changes in machinery by being able to explore families of Φ mappings, within the space of mappings Φ_S , where S is the sample space of times during individual stages of the flight. With a more general notion of the rate of change of the maximum capacitance with respect to not only the flight number of a cycle but also with respect to the hardware specific requirements of the battery and equipment that are being used, our approach can be of use in future experiments as well.

Another area of interest for future work includes being able to develop a broader formalism so that the approach can describe other data structures that could arise in the experimentally gathered current readings. With more complicated experiments and specifications imposed upon either the amount of current that will be delivered throughout the circuit during a flight, or upon the duration of the flight itself, it would be helpful to continue expanding on the approach so that flights with an arbitrary number of stages can be analyzed, which could improve battery maintenance, as well as overall construction of the aircraft for optimal aerodynamic performance in a wide variety of flight profile patterns. Although the estimates for the decay in the maximum capacitance will not be subject to electromagnetic radiation effects that are present in the background of the environment which can significantly impact the temperature at which the equipment optimally functions, another exponential factor with its own free parameter accounting for the difference between the ambient temperature of the environment, and the maximum temperature at which the battery will continue to carry sufficient enough current above the SOC threshold, can be introduced.

REFERENCES

- Goebel, K., & Eklund, N. (2007). Prognostic fusion for uncertainty reduction. In *Aiaa infotech@aerospace 2007 conference and exhibit*.
- Hogge, E., & et. al. (2014). Verification of a remaining flying time predictions system for small electric aircraft. In *Annual conference of the phm society*.
- Kulkarni, C., Biswas, G., Celaya, J. R., & Goebel, K. (2011). Prognostics techniques for capacitor degradation and health monitoring. In *The maintenance and reliability conference, marcon*.
- Kulkarni, C., Biswas, G., Koutsoukos, X., Goebel, K., & Celaya, J. (2010). Physics of failure models for capacitor degradation in dc-dc converters. In *The maintenance reliability conference, marcon 2010 the maintenance & reliability conference, marcon 2010*.
- Kulkarni, C., Hogge, E., Quach, C., & Goebel, K. (2015). "hirf battery data set". In *Nasa ames prognostics data repository*. NASA.
- Saha, B., Saha, S., & Goebel, K. (2009). A distributed prognostic health management architecture. In *Ieee aerospace conference*.
- Sankararaman, S., & Goebel, K. (2013a). Remaining useful life estimation in prognosis: An uncertainty propagation problem. In *Aiaa infotech conference*.
- Sankararaman, S., & Goebel, K. (2013b). Uncertainty quantification in remaining useful life of aerospace components using state space models and inverse form. In *54th aiaa structures, structural dynamics & materials conference*.